



**DEVELOPMENT OF A MIXED-RADIATION  
DIRECTIONAL ROTATING SCATTER MASK  
DETECTION SYSTEM**

THESIS

Bryan V. Egner, Second Lieutenant, USAF  
AFIT-ENP-MS-19-M-075

**DEPARTMENT OF THE AIR FORCE  
AIR UNIVERSITY**

**AIR FORCE INSTITUTE OF TECHNOLOGY**

**Wright-Patterson Air Force Base, Ohio**

DISTRIBUTION STATEMENT A  
APPROVED FOR PUBLIC RELEASE; DISTRIBUTION UNLIMITED.

The views expressed in this thesis are those of the author and do not reflect the official policy or position of the United States Air Force, Department of Defense, or the United States Government. This material is declared a work of the U.S. Government and is not subject to copyright protection in the United States.

AFIT-ENP-MS-19-M-075

DEVELOPMENT OF A MIXED-RADIATION DIRECTIONAL ROTATING  
SCATTER MASK DETECTION SYSTEM

THESIS

Presented to the Faculty  
Department of Engineering Physics  
Graduate School of Engineering and Management  
Air Force Institute of Technology  
Air University  
Air Education and Training Command  
in Partial Fulfillment of the Requirements for the  
Degree of Master of Science in Nuclear Engineering

Bryan V. Egner, BS  
Second Lieutenant, USAF

March 2019

DISTRIBUTION STATEMENT A  
APPROVED FOR PUBLIC RELEASE; DISTRIBUTION UNLIMITED.



Designator Number

Title

Student's Name and Rank

Approved:

Committee Chair Signature   
Digitally signed by BURGGRAF.LARRY.W.1078567909  
Date: 2019.02.12 11:18:09 -05'00' Date

Committee Member Signature   
Digitally signed by BEVINS.JAMES.EDWARD.1113201890  
Date: 2019.02.15 05:51:28 -05'00' Date

Committee Member Signature   
Digitally signed by HOLLAND.DARREN.E.1282993755  
Date: 2019.02.15 09:23:11 -05'00' Date

Committee Member Signature  Date

For Dissertations Only

Dean's Acceptance  Date

ADEDEJI B. BADIRU, Ph.D.  
Dean, Graduate School of Engineering and Management

## **Abstract**

Previous work demonstrated gamma-ray directional detection through the integration of a radiation detection system and an additively manufactured rotating scatter mask (RSM). This work advances the RSM directional detection system through improvements in the system's design, validation of a new scatter mask, and the novel ability to directionally detect both neutrons and gamma rays, a desirable feature for many nuclear safeguard and counterproliferation applications. The mixed-radiation RSM system developed for this research utilized the Spartan I mask design coupled with a 1" EJ-309 liquid scintillator. A GEometry ANd Tracking (Geant4) model is developed and quantitatively compared to experimental measurements for both pulse-height energy spectra and detector response curves, validating the system's directional detection capabilities. Two sets of directional measurements are performed with an americium-beryllium source, varying the source's distance and direction for each set. The RSM correctly identified the direction of the source within  $5^\circ$  in both the azimuthal and polar directions for neutron induced events and within  $10^\circ$  for gamma rays. The results demonstrated the RSM is a compact, lightweight, and modular directional detection system useful for safeguard and counterproliferation missions that require rapid identification of the type and location of radioactive sources.

## Acknowledgements

I am very thankful for the assistance and support from my advisor Dr. Burggraf, and my committee, Capt Bevins and Dr. Holland. Others who warrant recognition are Mr. Taylor, Lt Olesen, Capt Condon, Maj Recker, Dr. Bickley, and Mr. Gautam for assisting in helping me perform both the computational and experimental work of this thesis. Additionally, gratitude is owed to Ms. Martin, the AFIT 3D Print Shop, and the entire AFIT Model Shop for assisting in building the new RSM system.

Bryan V. Egner

# Table of Contents

	Page
Abstract .....	ii
Acknowledgements .....	iii
List of Figures .....	vi
List of Tables .....	ix
1. Introduction .....	1
1.1 Motivation .....	1
1.2 Background .....	3
1.3 Problem .....	4
1.4 Hypothesis .....	5
1.5 Approach .....	5
1.6 Research Assumptions and Limitations .....	6
1.7 Research Contributions .....	7
2. Theory .....	9
2.1 Rotating Scatter Mask Directional Detection System .....	9
2.1.1 Rotating Scatter Mask System Overview .....	9
2.1.2 Direction Identification Method .....	12
2.2 Alternate Directionally Sensitive Neutron Detection Systems .....	13
2.2.1 Rotating Modulating Collimator .....	13
2.2.2 Single-Volume Neutron Scatter Camera .....	15
2.3 Neutral-Particle Interactions with Matter .....	15
2.3.1 Neutron Energy Loss Mechanisms .....	17
2.3.2 Gamma-Ray Energy Loss Mechanisms .....	19
2.4 Neutron Sources .....	21
2.5 Nuclear Cross Sections .....	23
2.5.1 Active Detector Volume Material .....	24
2.5.2 Scatter Mask Material .....	26
2.6 Radiation Detection .....	29
2.6.1 Fast Neutron Detection .....	30
2.6.2 Slow Neutron Detection .....	30
2.6.3 Gamma-Ray Detection .....	31
2.6.4 Scintillation Process .....	32
2.6.5 Pulse Shape Discrimination .....	34
2.7 Quantitative Metrics for Distribution Comparisons .....	42
2.7.1 Modal Assurance Criterion .....	42

	Page
2.7.2 Chi-Squared Test .....	43
3. Methodology .....	45
3.1 Scatter Mask Design .....	46
3.2 Experimental Measurements .....	48
3.2.1 System Design .....	48
3.2.2 Experimental Setup .....	49
3.3 Radiation Transport Model .....	52
3.3.1 Geant4 Toolkit .....	52
3.3.2 Rotating Scatter Mask Simulation .....	52
4. Results .....	58
4.1 Pulse Shape Discrimination Performance .....	58
4.2 Energy Spectrum Analysis .....	61
4.2.1 Energy Calibration .....	61
4.2.2 Spectral Broadening .....	64
4.2.3 AmBe Spectrum Results .....	69
4.3 Directional Measurements .....	75
4.3.1 Direction Identification Performance .....	75
4.3.2 Modal Assurance Criterion Direction Identification Method .....	81
4.3.3 Rotating Scatter Mask Field-of-View .....	85
4.3.4 Relative Efficiency Characterization .....	85
5. Conclusion .....	88
5.1 Future Research .....	89
Appendix A. Equipment and Settings .....	92
Appendix B. Radiation Source Information .....	94
Appendix C. Rotating Scatter Mask Research Repository .....	95
Bibliography .....	97

## List of Figures

Figure		Page
1	Comparison of the Original RSM System and the New System. ....	11
2	RSM Spherical Coordinate System .....	12
3	Example MCNP6.1.4 Simulated DRC Performed in Previous Work .....	13
4	An Image and Schematic Diagram of a Modified RMC Used for Directional Thermal Neutron Detection .....	14
5	Types of Neutron Reactions .....	16
6	Laboratory and Center-of-Mass Coordinate System for Elastic Scattering .....	18
7	Graphical Representation of Gamma-ray Compton Scattering .....	20
8	Example Continuous-Energy Watt Neutron Fission Spectra.....	22
9	AmBe Discrete Energy Neutron Spectrum .....	23
10	Macroscopic Cross Sections of an EJ-309 Scintillator for Fast Neutron Energies (0.1 MeV to 11.7 MeV) .....	25
11	Gamma-ray Macroscopic Cross Sections for an EJ-309 Scintillator .....	26
12	Total Fast Neutron Macroscopic Cross Section of the PMMA Scatter Mask .....	28
13	Gamma-ray Macroscopic Cross Sections for the PMMA Scatter Mask.....	29
14	Energy levels for a $\pi$ -Electron Structure for Light Photon Production in Scintillation Materials .....	33
15	Scintillation Light Yield for an Organic Plastic Scintillator .....	35

Figure	Page
16	Total Stopping Power of Protons and Electrons for an EJ-309 Scintillator . . . . . 36
17	Induced Particle Dependent Light Intensity Plots for Stilbene, an Organic Plastic Scintillator . . . . . 37
18	Example Signal Waveform for an EJ-309 Scintillator . . . . . 39
19	Example of 2D PSD Histogram . . . . . 40
20	Double Gaussian fitted PSD ratio Histogram from an AmBe Neutron Source with an EJ-309 Scintillator. . . . . 41
21	Directional Detection Validation and Verification Flowchart . . . . . 45
22	Spartan I 3D SolidWorks Model and 2D Design Matrix . . . . . 47
23	The Spartan I mask Being 3D Printed at AFIT . . . . . 48
24	A Labeled Image of the RSM System . . . . . 49
25	Example Directional Measurement of an AmBe Source with the RSM System . . . . . 51
26	Geant4 Geometry for the RSM . . . . . 55
27	Example Geant4 Simulation Run for the RSM . . . . . 57
28	2D PSD Histogram an AmBe Source with an EJ-309 Scintillator . . . . . 59
29	Detector Calibration Using Gamma-Ray Compton Edges . . . . . 62
30	Detector Energy Calibration Curve . . . . . 63
31	Detector Resolution $\chi^2$ -Minimization Algorithm . . . . . 66
32	Detector Resolution Curve . . . . . 67
33	Experimental and Broadened Gamma-Ray Spectra . . . . . 68
34	Birks' Formula Parameter $\chi^2$ -Minimization Algorithm . . . . . 70
35	Estimation of Proton Light Yield Using Birks' Formula . . . . . 71

Figure	Page
36	Experimental and Broadened $^{12}\text{C}^*$ de-excitation Energy Spectra..... 72
37	Experimental and Broadened AmBe Neutron Energy Spectra..... 74
38	Geant4 Simulated Neutron DRM for an AmBe source Using an EJ-309 Scintillator..... 76
39	Geant4 Simulated Valley Separation Curve..... 77
40	Directional Measurement Set 1: Neutron DRCs..... 79
41	Directional Measurement Set 1: Gamma-Ray DRCs..... 80
42	Directional Measurement Set 2: Neutron DRCs..... 82
43	Directional Measurement Set 2: Gamma-Ray DRCs..... 83
44	MAC Comparison Matrices for Neutron DRCs..... 84
45	DRC Valley Ratios..... 86
46	Geant4 Simulated Normalized Neutron Event Rate..... 87

## List of Tables

Table		Page
1	Scatter Mask Material Properties .....	28
2	Geant4 Model Parameters and Settings .....	54
3	Geant4 Model Material Properties .....	54
4	Radiation Detection System Settings .....	58
5	Gamma-Ray Calibration Sources.....	61
6	Experimental and Geant4 Simulated Gamma-Ray Spectra Comparison.....	66
7	Experimental and Geant4 Simulated AmBe Spectra Comparison .....	73
8	Direction Identification Results for Neutrons .....	78
9	Direction Identification Results for Gamma Rays.....	78
10	Directional Measurement Set 1: AmBe DRC Comparison .....	81
11	Directional Measurement Set 2: AmBe DRC Comparison .....	81
12	RSM Relative Efficiency Loss.....	87
13	Rotating Scatter Mask System Equipment List .....	92
14	Full List of Radiation Detection System Settings .....	93
15	Radiation Source List .....	94

# DEVELOPMENT OF A MIXED-RADIATION DIRECTIONAL ROTATING SCATTER MASK DETECTION SYSTEM

## 1. Introduction

### 1.1 Motivation

The development of a novel compact directional detection system for both neutrons and gamma rays directly supports the United States' sustainment of specialized capabilities to combat nuclear terrorism, as stated in the 2018 Nuclear Posture Review (NPR), "to sustain specialized capabilities to search, interdict, characterize, and disable nuclear devices" [1]. A wide range of nuclear security applications exist for portable and directional radiation detectors under the umbrella highlighted by the NPR including radioactive source surveying in shipyards, radiation monitoring at border crossings, event security and monitoring, and aerial drone radiation surveying. Specifically, mixed-radiation directional detection would assist day-to-day operations of the Civil Support Team (CST), a specialized United States National Guard unit tasked with protecting and defending the nation against chemical, biological, radiological, nuclear, and explosive (CBRNE) threats [2]. The CST takes part in a wide range of training exercises to be ready for any scenario involving CBRNE threats, many of these exercises would be more efficiently completed by using a portable directional detection system. In 2016, a press release by the United States Army, titled *National Guard team searches for radioactive material on Lake Champlain*, describes an exercise where various personnel including members of the 2nd CST had to locate various radiation sources hidden on boats and in parked cars at Lake Champlain on

the border of the United States and Canada [3]. The report stated various detectors and equipment were needed because of the difficulty in locating sources over such a large area. In the future, a portable and inexpensive system like the rotating scatter mask (RSM) directional detection system capable of measuring both neutrons and gamma rays could be hand carried by personnel surveying for sources. Such a system could also be mounted to a drone to cover more ground.

The development of a simple, yet versatile, directional neutron and gamma-ray detection system significantly enhances the current field capabilities used to solve two key problems, the interdiction of illicitly trafficked special nuclear material (SNM) and the orphan source problem. The Department of Energy (DOE) classifies SNM as accountable nuclear materials used to develop a nuclear weapon or improvised nuclear device (IND) [4]. Characteristic of SNM is the emission of both neutron and gamma-ray signatures where a mixed radiation directional detector would not only be able to identify the direction of such material, but also potentially identify the type and origin of the source. This is a useful feature as the environmental neutron background is low and only a few heavy actinides, most of which are classified as SNM, are likely emitters. The orphan source problem, defined by the Nuclear Regulatory Commission (NRC) as the issue of locating uncontrolled and unwanted radioactive materials, this includes both lost and stolen materials emitting neutrons or gamma rays, or both [5]. A proof-of-concept, both computationally and experimentally, is provided to demonstrate how and why the RSM system is capable of solving these problems. This chapter serves to provide a brief background and summary of the approach, limitations, and accomplishments for this research.

## 1.2 Background

Directional gamma-ray detection is not novel technology, as many systems have been developed to locate radioisotopes. Many of these gamma-ray systems utilize arrays of detectors and coded-apertures involving some form of collimator to determine the direction of a gamma-ray source. For example, the SuperMISTI system, developed by the Office of Naval Research (ONR) has been proven to detect and image sources up to 400 feet away, with the goal of achieving up to a mile via active interrogation methods using bremsstrahlung pulses. However, this system costs over \$1,000,000 (USD) and weighs over 17,000 pounds [6], lacking mobility and simplicity. Smaller systems have also been developed and deployed, such as the Germanium Gamma-Ray Imager (GeGI) produced by PHDS Co. The GeGI weighs only 28 pounds, and costs approximately \$150,000 (USD) [7]; however, germanium detectors are susceptible to vibrational and microphonic resolution degradation making these detectors less suitable for use on airborne platforms. Additionally, performance degradation occurs for germanium detectors in the presence of fast neutrons limiting this system to strictly gamma-ray directional detection [8]. H3D Inc. has developed a line of proprietary portable detection systems primarily for gamma-ray identification and directional detection where some are lighter than 8 pounds [9], but do not detect neutrons.

Another option for directional gamma-ray detection is the RSM system developed at The Air Force Institute of Technology (AFIT). For the gamma-ray RSM, the detector signal as a function of the rotational angle of the uniquely designed mask allows for simple signal processing to obtain directional information about a radiation source. The gamma-ray RSM system has been computationally and experimentally proven to find the direction of multiple gamma-ray sources, and various mask designs have been computationally explored [10–14]. The newly developed RSM system assembled for this proof-of-concept study weighs only 15 pounds and costs under \$11,000, making

the RSM system competitive with other directional detection systems already on the market.

The field of directional neutron detection, especially for cost-effective and portable systems, is much less developed. Current directional neutron detection systems rely on pinhole techniques, coded apertures, or neutron cameras utilizing large arrays of detectors and or complex system geometries [15]. Research published at Sandia National Laboratory shows the feasibility of creating a single-volume neutron scatter camera (SVNSC) [15, 16], but this technique relies heavily on precise timing and positioning of induced photons from two neutron elastic scattering events. Thus, there is an increase in the complexity and overall reduction in efficiency for this system.

In contrast, the neutron RSM, based on the gamma-ray RSM system, strives to be a compact and modular single detector directional detection system. The modularity and simplistic concept allows for the system to have both interchangeable detectors and masks depending on the application and operational environment. The system's components enable the exploration of applying the RSM for neutron detection and introduces the capability of mixed-radiation imaging by utilizing a detector with high  $n/\gamma$  discrimination.

### **1.3 Problem**

The task of interdicting illicitly trafficked SNM is aided by directional neutron detection systems. However, there are not efficient, portable, and simple systems available on the market to solve this challenge. This research seeks to address this gap and demonstrate the RSM system's directional detection capabilities for neutrons, while simultaneously demonstrating mixed-radiation directional detection capabilities by detecting gamma rays. By data fusing both neutron and gamma-ray signatures,

more information about the origin and type of source could be extracted.

## 1.4 Hypothesis

This research is based on the hypothesis that the angle identification technique, applied to the gamma-ray RSM system and explained in Section 2.1.2, can also be applied to a neutron RSM system. Instead of using full energy peak (FEP) information, originally used in the gamma-ray RSM system, the neutron RSM will utilize the full recoil proton response curves produced from neutrons elastically scattering off hydrogen nuclei inside of an EJ-309 scintillator. The neutron source's direction can then be found by integrating the response histograms for each mask rotation angle to develop an overall detector response curve (DRC) similar to the gamma-ray RSM FEP DRC. Additionally, through pulse shape discrimination (PSD), Compton integral gamma-ray DRCs are generated introducing the novel capability of mixed-radiation directional detection.

## 1.5 Approach

A Monte Carlo radiation transport model of the gamma-ray RSM, developed by Logan and Holland [11] in previous studies, using GEometry ANd Tracking Version 10.3 Patch 2 (Geant4) [17] is modified to include neutron transport and to track the secondary particles, primarily electrons and protons, induced by neutron and gamma-ray interactions. This model guided RSM design development and experimental validations of the system. Simulated detector response matrices (DRMs) over a field-of-view (FOV) from  $5^\circ$  to  $165^\circ$  in the polar direction, and a full  $360^\circ$  in the azimuthal direction are generated for an americium-beryllium (AmBe) neutron source and 4.438 MeV gamma-ray source. The model is experimentally validated through measurements of an AmBe source with an EJ-309 scintillator encased in an additively

manufactured Spartan I scatter mask developed by Olesen and Holland [12]. These steps accomplished the primary research objective of establishing a proof-of-concept verification for determining an AmBe source’s direction both computationally and experimentally using the neutron and gamma-ray responses with the RSM system.

## 1.6 Research Assumptions and Limitations

Serving as a proof of concept for directional neutron detection, this study is limited to the resources available in a laboratory setting, and the limitations of Geant4 radiation transport modeling. The Geant4 model assumes the source is a point source with no self-shielding, models an ideal detector response, has perfect angular binning of detected events, and utilizes a simplified system, material composition, and environment geometry. To convert the simulated recoil proton energy deposition to the measured electron equivalent energy deposition, Birks’ formula, discussed in Section 2.6.5, is used [18]. While Birks’ formula has been shown to capture the photon light yield response well, some studies have observed a breakdown in the relation at low proton energies below 500 keV [19]. To account for the simulation’s ideal response, the simulated pulse-height energy spectra for both neutrons and gamma rays are broadened with energy-dependent Gaussian distributions, before comparing the simulated results with experimentally measured spectra [8]. Experimentally, the response curves could have error from signal collection losses, signal noise, charge collection efficiency, and gamma-ray pile-up. Additionally, there is always the possibility of error in the source and detector placement, and mask rotation angle. Lastly, to mitigate discrepancies between the model and experimental results, the measurements are taken at fixed mask rotational angles in  $10^\circ$  increments instead of rotating at a set rotational speed to prevent angular event binning biases.

## 1.7 Research Contributions

This research advanced the state-of-the-art for directional detection systems. Some of the more notable contributions are:

- **Validation of a neutron direction identification capability:** This research demonstrated the ability to identify a neutron source's direction using the RSM methodology previously implemented for gamma rays.
- **Demonstrated mixed-radiation directional identification:** The use of an EJ-309 scintillator with high  $n/\gamma$  discrimination allowed for source direction identification from either the neutron or gamma-ray emissions. Additionally, the ability to use Compton scattering events to generate gamma-ray DRCs increases the overall detection efficiency compared to FEP DRCs in previous work [11]. This result demonstrates the potential for identifying the direction and also characterizing unknown sources.
- **Assembled new RSM system:** A more compact and modular RSM system was assembled with the ability to easily change detectors and masks for rapid experimental testing and development.
- **Validation of Spartan Class mask designs:** Previous research with the RSM had only simulated the performance of using a scatter mask design from the Spartan Class to determine a gamma-ray source's direction [12]. This work serves as an experimental validation of the ability to identify the direction of a neutron and gamma-ray source with the Spartan I mask.
- **Enhanced RSM radiation transport model:** This research led to enhancing the RSM Geant4 simulation package by extending the RSM system model to

obtaining a neutron detector response, and by implementing secondary particle tracking capabilities.

## 2. Theory

Development of a neutron RSM detection system requires an understanding of how neutrons interact with the mask and detector to convert the deposited energy into a usable signal for determining the source direction. First, an overview of how the RSM works and prior developments are provided. This topic is followed by a comparison of alternative directional neutron detection systems to the RSM. Then, a summary of basic neutron reactions, common neutron sources, and a breakdown of the relevant mask and detector nuclear cross sections are presented. A brief discussion on gamma-ray interactions with matter is provided to understand the mixed-radiation capabilities of this system. After understanding the nuclear cross sections for each material, the methods of both fast and thermal neutron and gamma-ray detection are summarized for organic liquid scintillators. Finally, the quantitative and statistical metrics used for comparing experimental measurements and Geant4 simulated data are discussed. Together, the information provided in the following sections allow for an understanding and interpretation of the results and conclusions made in Chapters 4 and 5.

### 2.1 Rotating Scatter Mask Directional Detection System

#### 2.1.1 Rotating Scatter Mask System Overview

In 2015, FitzGerald introduced the concept of using a rotating mask to scatter, not collimate, radiation traveling towards a detector [10]. Ideally, this phenomenon results in a unique DRC to determine the source's direction. Since then, further contributions have been made by Charles, Holland, Logan, Condon, Olesen, and Martin, leading to the following RSM system milestones:

- FitzGerald: Conception and preliminary Monte Carlo N-Particle eXtended

(MCNPX) simulations for a gamma-ray RSM system to establish the feasibility of the novel imaging system [10].

- Charles: Built and performed the initial experimental validation of a gamma-ray RSM system [11].
- Logan: Developed a Geant4 model of the gamma-ray RSM system. Also, performed an experimental validation by correctly determining the direction of a  $^{137}\text{Cs}$  source 86.36 cm from the detector using the 662 keV FEP to generate DRCs, and then the Modal Assurance Criterion to compare the experimental DRCs to the Geant4 DRCs [11].
- Holland: Initiated efforts to optimize mask designs by removing degeneracies in the DRCs for different source directions and developed an automated Monte Carlo N-Particle (MCNP) version 6.1.4 RSM model generator to quickly build and analyze new mask designs [13].
- Condon: Experimentally demonstrated the ability to determine the direction of three different gamma-ray sources at once with the gamma-ray RSM using the FitzGerald mask design [14].
- Olesen: Performed a mask design parameter study for the Spartan Class of mask designs. The Spartan designs allow for a simplified method of determining the source's direction by decoupling the azimuthal ( $\theta$ ) and the polar ( $\phi$ ), angles and eliminate the need to compare the experimental DRC with a library of pre-obtained DRCs [12].
- Martin: Designed a more compact RSM system using SolidWorks and performed a finite element analysis of the stresses using Abaqus [20].

Both the original gamma-ray RSM system, used by Charles, Logan, and Condon, and the new neutron RSM system, designed by Martin and used in this work, are shown in Figure 1. The original system utilized a 3" by 3" Saint-Gobain sodium iodide thallium-doped (NaI(Tl)) scintillator [21] with a 28-pound Poly(methyl methacrylate) (PMMA) scatter mask designed by FitzGerald and constructed by Charles. The new system weighs only 15 pounds including the mask, detection electronics, and mechanical rotation equipment. Also, it's volume is significantly less than half the old system's volume. A more detailed description of how the current system functions and operates is provided in Chapter 3.

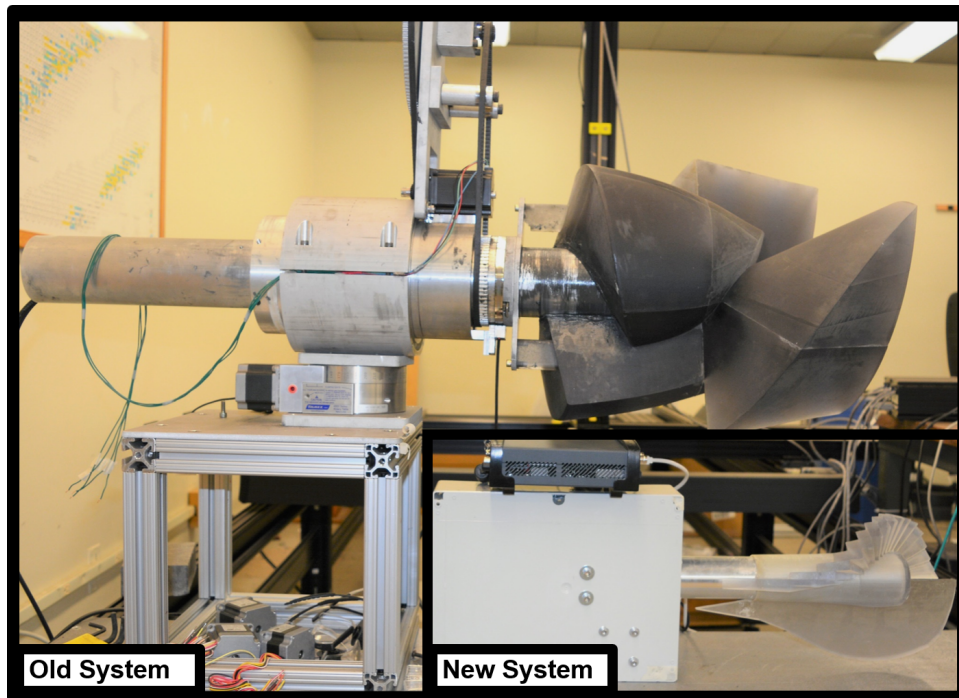


**Figure 1.** A comparison of the original gamma-ray RSM detection system and the new, more compact system. The radiation detection modules for the original system are not displayed; all of the components for the new system are encased in the white Polycase box.

### 2.1.2 Direction Identification Method

A spherical coordinate system, shown in Figure 2, is used for determining the source's direction. The final DRC produced by the system, depicted in Figure 3, is the total number of detected events as a function of the rotational angle,  $\theta$  for a given polar angle. The fin and wall features of the Spartan I mask result in two distinct valleys in the MCNP simulated DRCs for gamma rays generated by Olesen in previous work [12]. Olesen showed the  $\theta$  direction of a source is determined by the wall-induced valley, which is the deeper valley for  $\phi$  angles between  $35^\circ$  to  $165^\circ$ . Then, the  $\phi$  direction of the source is calculated from a linear expression based on the angular separation between the wall and fin valleys. This expression is obtained from the mask's physical geometry or from simulations. The mask geometry and linear expression are further discussed in Section 3.1.

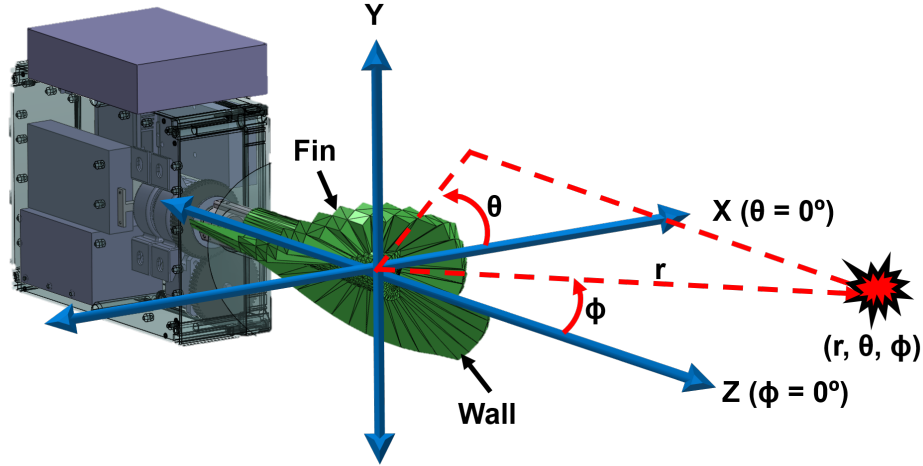


**Figure 2.** The RSM uses a spherical coordinate system where  $r$  is the source-to-detector distance,  $\phi$  is the polar angle, and  $\theta$  is the azimuthal angle. The mask rotates  $360^\circ$  in  $\theta$  around the detector. [20].

This method, referred to as the Spartan method, for determining the direction of a radiation source has only been demonstrated computationally for gamma rays. While the primary objective of this work is to demonstrate both computationally

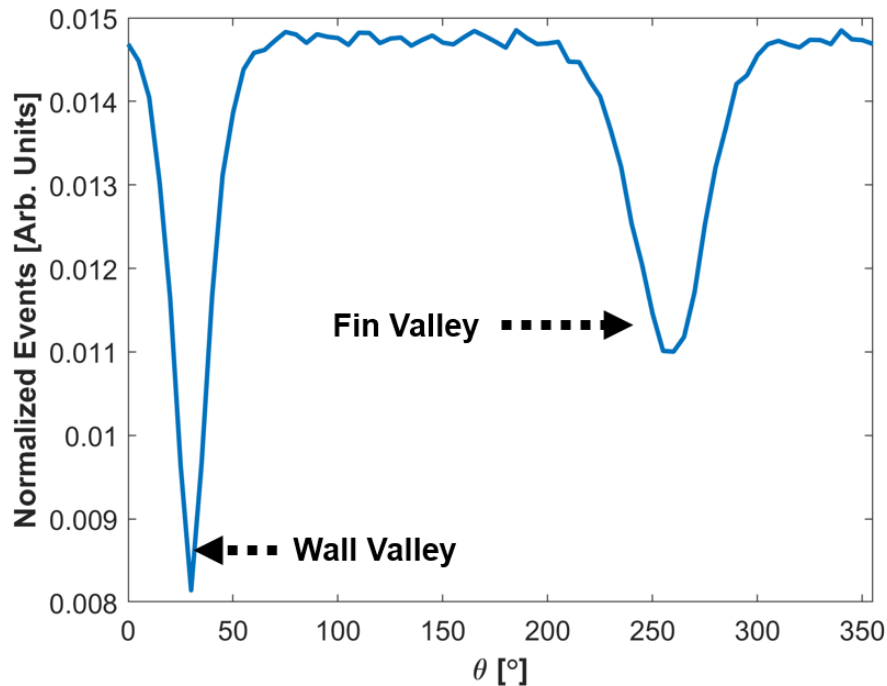


Figure 3. Example MCNP6.1.4 simulated DRC of a Spartan mask performed by Olesen [12]. The response curve shows two distinct valleys, one generated by the wall of the mask and the other from the fin of the mask. The  $\theta$  direction of a source is predicted by the location of the wall valley on the DRC, and the  $\phi$  direction can then be determined based on the distance between the centroids of the two valleys.

and experimentally that the Spartan I design also works for neutrons, a secondary objective is to experimentally validate the system for gamma rays.

## 2.2 Alternate Directionally Sensitive Neutron Detection Systems

### 2.2.1 Rotating Modulating Collimator

The Rotating Modulation Collimator (RMC), a predecessor to the RSM, was originally developed by Kowash for gamma-ray directional detection to assist in the orphan source search problem [22, 23]. Later, the RMC concept branched out into neutron and mixed-radiation directional-detection systems [24–26]. An example of a modified RMC constructed at AFIT for thermal neutron detection, along with a simplified diagram of the directional-detection process, are shown in Figure 4.

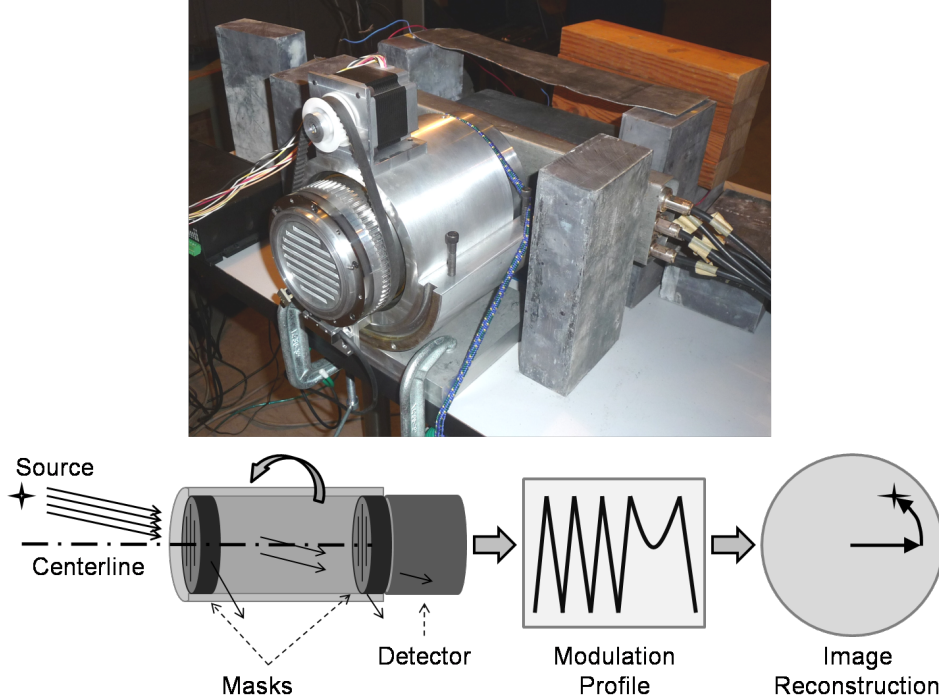


**Figure 4.** An image and simplified schematic diagram of a modified RMC used for directional thermal neutron detection at AFIT. The system consists of collimating masks inside of an aluminum cylinder, placed in front of  $^3\text{He}$  and  $\text{BF}_3$  detectors. To reduce backscattering effects, the detectors are wrapped in cadmium except for the area directly behind the outer mask [25].

The basic RMC concept incorporated a rotating collimating mask composed of a high atomic number material such as tungsten or lead placed in front of a detector. As the mask rotates, a unique modulation profile or DRC is generated to determine the direction of a source. This system relies solely on a single non-position sensitive detector, similar to the RSM system, to generate a multi-dimensional image by applying an image reconstruction algorithm to the total number of detected events binned by rotational angle.

The main difference between the DRCs produced by the RMC and RSM is that the current RSM Spartan I mask simplifies the complex image reconstruction algorithm to a linear expression dependent on the mask geometry. Other differences between the two systems include the portability and compactness of the RSM, a smaller efficiency loss from the mask because lower atomic number mask materials are used, and a larger

field-of-view (FOV) for the RSM. While the RMC explored the directional detection of thermal neutrons, this work focuses on fast neutrons as a more promising avenue due to more difficulties with thermal neutron scattering off environmental objects.

### **2.2.2 Single-Volume Neutron Scatter Camera**

Another directional neutron detection system currently being researched is the SVNSC at Sandia National Laboratories [15, 16]. The primary goal of this work is to develop a system that utilizes a single active detector volume rather than multiple segmented detectors used in existing Neutron Scatter Cameras (NSC) to reduce the size and improve geometrical detection efficiency. These systems obtain directional information by detecting two separate neutron elastic scattering events and performing a kinematic reconstruction to back out the original incident neutron direction.

The complexity and precision requirements of the SVNSC electronics system are much greater than the RSM system coupled with a Spartan I mask. This complexity is required for accurate determination of the origin of optical photons induced by the double elastic scattering events and will drive up the system's cost. The projected size and weight of the SVNSC is 40 cm by 40 cm by 20 cm with an estimated weight of 20 to 40 pounds, roughly 2-3 times that of the current RSM system. However, the SVNSC could have a true  $4\pi$  FOV, slightly larger than that of the RSM system.

## **2.3 Neutral-Particle Interactions with Matter**

A summary of the fundamental neutron and gamma-ray interactions with matter are provided to allow for an understanding of how neutrons and gamma rays can be detected and discriminated from each other in a single detector. Neutrons and gamma rays are neutral particles unaffected by the Coulomb force, which results in longer path lengths through matter compared to charged particles such as protons

and  $\alpha$  particles. Neutron interactions with nuclei are generalized into two distinct mechanisms, scattering and absorption reactions. Depicted in Figure 5, scattering reactions are further divided into elastic and inelastic reactions, where elastic scattering events result in the target nucleus remaining in a ground state while inelastic scattering leads to an excited nucleus. Inelastic scattering events are classified as endothermic interactions because energy is retained by the target nuclei leading to the emission of inelastic gamma rays to de-excite back to a ground state.

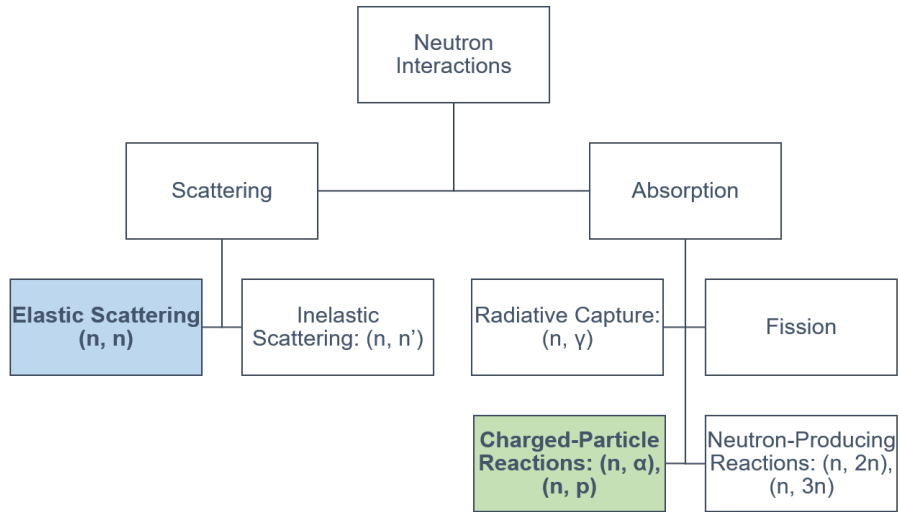


**Figure 5.** Typical neutron reactions categorized as scattering or absorption events. Green blocks depict reactions of interest for detecting thermal neutrons, and blue blocks represent reactions of interest for detecting fast neutrons for this study [8, 27].

Analogous to scattering reactions, absorption reactions are commonly sub-divided into fission, radiative capture, charged particle producing, and neutron-producing reactions. Both fission and neutron-producing reactions result in the production of additional neutrons. Fission events occur when an absorbed neutron causes an excited nucleus to stabilize by splitting into fragments and free neutrons. In contrast, a neutron-producing reaction causes a nucleus to eject loosely bound neutrons. Often these neutron-producing reactions are denoted as  $(n, Xn)$  reactions, where  $X$  depends on the number of neutrons released. Lastly, when a neutron is absorbed, other types of radiation could be emitted to de-excite the target nucleus. Examples of this include

gamma rays for radiative capture and charged particles for neutron-induced charged particle reactions [27].

To understand how radiation is detected using an EJ-309 scintillator a summary of the energy loss mechanisms of free neutrons and gamma rays are provided along with various sources of free neutrons in the following two sections. Then, a discussion on relevant cross sections for this work is presented. Finally, the primary interaction mechanisms of importance for gamma-ray detection are discussed in Section 2.3.2.

### 2.3.1 Neutron Energy Loss Mechanisms

Radiation detection is fundamentally possible by converting the energy of incident radiation particles inside of an active detector volume to some form of processable electric pulse or current. The primary energy loss mechanisms for neutrons are partial or full-energy transfer by a scattering or absorption event, respectively. For this work, the partial energy transfer via elastic scattering is the primary means of detecting fast neutrons. When a neutron with energy  $E_0$  elastically scatters with a target nucleus of mass  $A$  at rest, the conservation of energy and momentum laws allow for the derivation of the recoil nucleus energy,  $E_R$ , expressed as [8]

$$E_R = \frac{2A}{(A+1)^2}(1 - \cos(\Theta))E_0, \quad (1)$$

where both the  $E_R$  and  $E_0$  are measured in the laboratory system, while  $\Theta$  is the neutron scattering angle measured in the center-of-mass coordinate system. Figure 6, displays both the center-of-mass and laboratory reference frames for neutron elastic scattering, where  $\theta$  is the recoil nucleus scattering angle in the laboratory coordinate system. Equation 2 is used to convert the center-of-mass system scattering angle to the laboratory system [8].

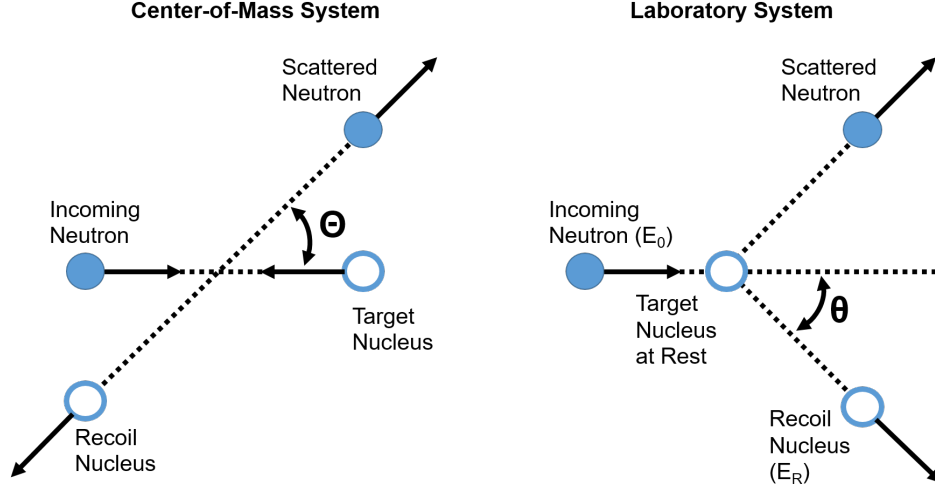


Figure 6. Laboratory and center-of-mass coordinate system for elastic scattering [8].

$$\cos(\theta) = \sqrt{\frac{1 - \cos(\Theta)}{2}} \quad (2)$$

Combining Equations 1 and 2, the recoil energy is defined using the recoil nucleus scattering angle as

$$E_R = \frac{4A}{(A + 1)^2} \cos^2(\theta) E_0. \quad (3)$$

This expression shows the energy transfer during a scattering event is dependent on the scattering angle, where the maximum energy transfer occurs for head-on collisions ( $\theta \cong 0^\circ$ ) and the minimum energy transfer is nearly zero for grazing collisions ( $\theta \cong 90^\circ$ ).

For hydrogen and recoil scattering angles of  $\theta \cong 0^\circ$ , Equation 3 results in  $E_R \cong E_0$ , indicating all of the energy is transferred in a single collision. This makes hydrogen an appealing material for recoil detectors since the recoil hydrogen will become ionized leading to a free recoil proton and electron. The proton carries away almost all of the transferred kinetic energy and is measured through scintillation mechanisms discussed in Section 2.6.4. Heavier nuclei, on the other hand, transfer on average a

smaller fraction of energy from the neutron due to their higher atomic mass. This reduces the probability of generating high enough energy charged particles inside of the scintillation crystal required for detection purposes.

For thermal or slow neutrons, the energy transfer from scattering is too small to generate a usable detector signal, so absorption reactions are the preferred interaction mechanism. For example, a common reaction used for slow neutron detection is the  $^{10}\text{B}(n,\alpha)^7\text{Li}$  reaction, which has a very high probability, or cross section, at low neutron energies. In this reaction, a thermal neutron incident on a  $^{10}\text{B}$  nucleus is absorbed and 94% of the time produces a charged  $^7\text{Li}^*$  ion and an  $^4\alpha$  particle with energies of 0.84 MeV and 1.47 MeV, respectively [8]. There is a 6% chance the  $^7\text{Li}$  ion will be emitted directly into the ground state resulting in energies about 21% larger. Using dopants such as boron in scintillators allows for the detection of both fast and slow neutrons.

### 2.3.2 Gamma-Ray Energy Loss Mechanisms

In addition to detecting neutrons, some detectors also have the ability to convert incident gamma rays into a detectable signal as well. The three primary gamma-ray interactions for detection are photoelectric absorption, Compton scattering, and pair production. In photoelectric absorption, an incident gamma ray interacts with the atom as a whole, is absorbed, and emits a photoelectron from one of the bounded electron shells. The resulting photoelectron energy,  $E_{e^-}$ , is equivalent to the incident gamma ray energy,  $E_\gamma$ , minus the shell binding energy,  $E_b$ , of the photoelectron as shown in Equation 4.

$$E_{e^-} = E_\gamma - E_b \quad (4)$$

For gamma-ray energies greater than a few hundred keV the binding energy becomes

very small compared to the incident gamma-ray energy resulting in the photoelectron carrying away most of the initial energy [8].

Another possible gamma-ray interaction is Compton scattering, where an incident gamma ray scatters off an electron transferring an amount of energy dependent on the kinematic scattering angle. Following the conservation of energy and momentum, the energy transfer to an electron in a Compton scattering event is represented graphically in Figure 7, or mathematically, with Equation 5. In Equation 5,  $E_{e'}$  is the recoil electron energy and  $m_0c^2$  is the electron rest mass energy, 0.511 MeV.

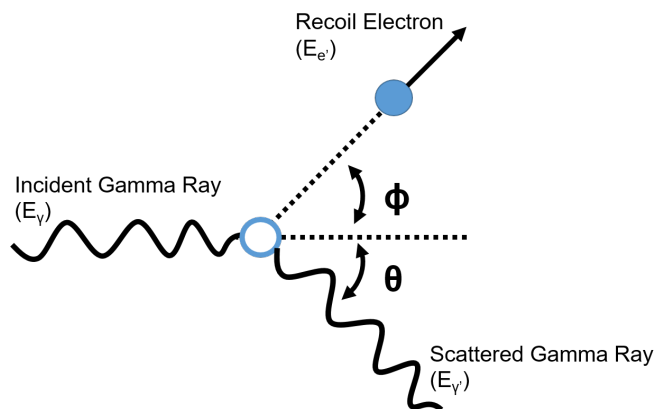


**Figure 7. Graphical representation of gamma-ray Compton Scattering with an electron. The kinetic energy transferred to the electron is dependent on the gamma-ray scattering angle [8].**

$$E_{e'} = \frac{E_\gamma}{1 + \frac{E_\gamma}{m_0c^2}(1 - \cos\theta)} \quad (5)$$

The last gamma-ray interaction of interest is pair production. This mechanism is only available for gamma rays with energies exceeding twice the rest-mass energy of an electron, which is required to create an electron-positron pair. The positron will ultimately annihilate with another free electron resulting in the emission of two 0.511 MeV photons emitted in nearly opposite directions.

## 2.4 Neutron Sources

Neutron sources of interest for nuclear safeguard applications consist of spontaneous fission reactions and neutron-emission nuclear reactions. Spontaneous fission, occurring in transuranic-heavy nuclides, releases neutrons with energies peaking between 0.5 and 1 MeV, but can reach energies exceeding 10 MeV [8]. The most common spontaneous fission source is  $^{252}\text{Cf}$ , yielding approximately 0.116 neutrons per second per becquerel and emitting neutrons isotropically with energies following a Watt spectrum as shown in Figure 8. The continuous-energy Watt fission spectrum is represented as a normalized intensity in arbitrary units, Arb. Units, and is approximated as

$$\chi(E) = Ce^{-E/A}\cosh(\sqrt{BE}), \quad (6)$$

where  $C$  is a normalization constant and  $A$  and  $B$ , in units of MeV and  $\text{MeV}^{-1}$ , respectively, are empirically determined isotope dependent parameters [28].

Examples of spontaneous fission sources pertaining to nuclear security applications are  $^{235}\text{U}$ ,  $^{238}\text{U}$ ,  $^{239}\text{Pu}$ , and  $^{240}\text{Pu}$ . Depending on the enrichment and weight, these isotopes are all classified as SNM and pose a proliferation threat [4]. These sources also emit neutrons following a Watt fission spectrum qualitatively similar to  $^{252}\text{Cf}$ , shown in Figure 8, making  $^{252}\text{Cf}$  a useful neutron source for developing a detection system to characterize SNM.

Neutron-emission nuclear reactions rely on the absorption of incident particles by a target nucleus, such as  $(\alpha, n)$  and  $(\gamma, n)$  reactions, resulting in the emission of neutrons when the product nucleus de-excites. AmBe is a common  $(\alpha, n)$  source frequently used for experimental measurements with neutron emission energies ranging from thermal energies to 11.19 MeV [29]. An example AmBe neutron energy spectrum is shown

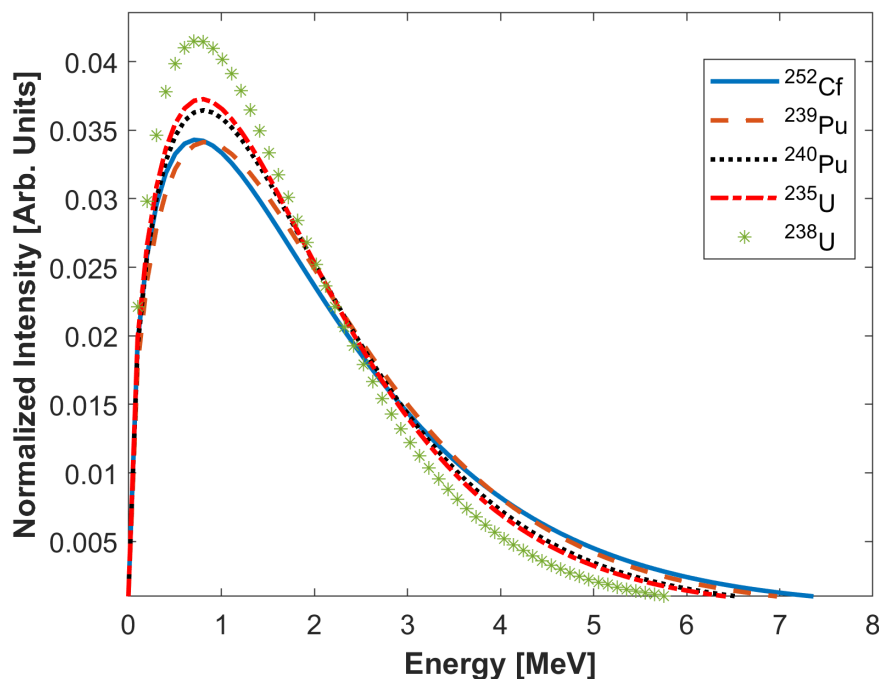


**Figure 8.** Normalized continuous-energy neutron spontaneous fission spectra for  $^{252}\text{Cf}$ ,  $^{239}\text{Pu}$ ,  $^{240}\text{Pu}$ ,  $^{235}\text{U}$ , and  $^{238}\text{U}$  generated using Equation 6 [28].

in Figure 9.  $^{241}\text{Am}$   $\alpha$ -decays with a half-life of 432.2 years, providing a relatively constant source of 5.486 MeV  $\alpha$  particles for the  $^9\text{Be}(\alpha, n)^{12}\text{C}^*$  reaction, which emits 30 neutrons per million alpha particles on average [29, 30]. The wide energy range of neutrons emitted makes AmBe neutron sources useful for characterizing fast neutron detection capabilities. Another appealing feature of an AmBe neutron source is a mono-energetic 4.438 MeV gamma-ray emission caused by the de-excitation of  $^{12}\text{C}^*$  following  $^{13}\text{C}^*$  de-excitation by neutron emission. For this work, an AmBe source is used due to being the most easily accessible neutron source at AFIT and because of the complimentary mono-energetic gamma ray allowing for both neutron and gamma-ray directional detection in a single set of measurements. A current limitation is this source does not emit a Watt fission spectrum characteristic of SNM, but in future work directional measurements with  $^{252}\text{Cf}$  will be made.

Another type of neutron-producing nuclear reaction involves colliding charged

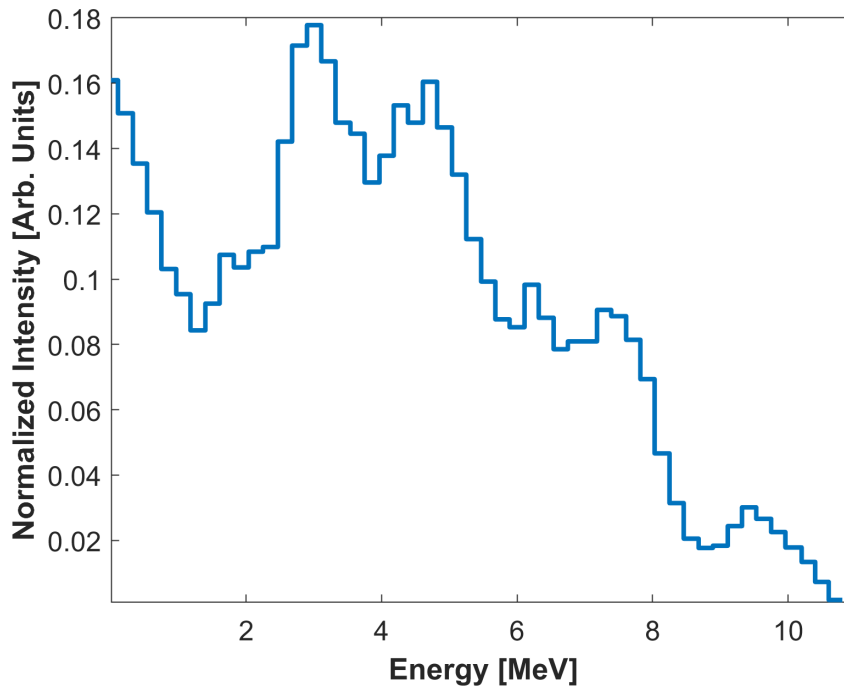


**Figure 9.** Normalized discrete-energy neutron spectrum for an AmBe source generated using spectral data from ISO 8529-1:2001 [31].

particles together with enough energy to overcome the Coulomb barrier. Neutron generators capitalize on these reactions by fusing two deuterium ions (D+D) or a deuterium and tritium (D+T) ion together producing approximately 2.45 and 14.1 MeV neutrons, respectively [8]. For thin targets, this method of generating neutrons creates a mono-energetic neutron source. This makes D+D and D+T fusion neutron sources useful for characterizing the fast neutron detection performance at specific energies. However, they are more suited to serve as sources for characterizing the neutron emission from a detonated nuclear weapon rather than assisting in developing a system for finding and characterizing SNM.

## 2.5 Nuclear Cross Sections

One of the most important nuclear properties to consider when choosing an active detector volume and scatter mask material is the nuclear cross section of the mate-

rial. The probability a neutron will interact with a nucleus, or the effective area of interaction, is called the microscopic cross section,  $\sigma$ , expressed in units of barns; one barn is equivalent to  $10^{-24}$  cm<sup>2</sup>. Neutron cross-sections are highly dependent on both the energy of the incident particle and the specific isotopes of the target material. To account for the effect of a material's atom density,  $N$ , on the probability of neutron interaction, a quantity called the macroscopic cross section,  $\Sigma$ , is calculated as

$$\Sigma = N\sigma \left[ \frac{1}{cm} \right] \quad (7)$$

and is interpreted as the probability per unit path length for a reaction process to occur [8]. The total probability of interaction,  $\Sigma_{total}$ , is the sum of all the different possible nuclear reactions that can occur when a neutron collides with a nucleus.

The diverse types of neutron interactions with matter require a thorough analysis of the isotopic composition of the active detector volume and scatter mask to fully understand the final DRC produced by the neutron RSM system. These characteristics are discussed in the subsequent sections. The probability of gamma-ray interactions are analogous to neutrons and are discussed as well.

### 2.5.1 Active Detector Volume Material

An EJ-309 liquid scintillator is composed of organic material: hydrogen and carbon. For this experiment, the neutron macroscopic cross sections of interest are the hydrogen elastic scattering cross section, and total carbon cross section, displayed in Figure 10 [32]. A discrete neutron energy spectrum for an AmBe source is overlaid to better visualize the neutron energies for this experiment and to demonstrate the use of an EJ-309 scintillator as a suitable detector [31]. Figure 10 shows at lower neutron energies, the probability of interaction is highest. However, if the incident neutron energy is not high enough, then an elastic scattering event will not result in

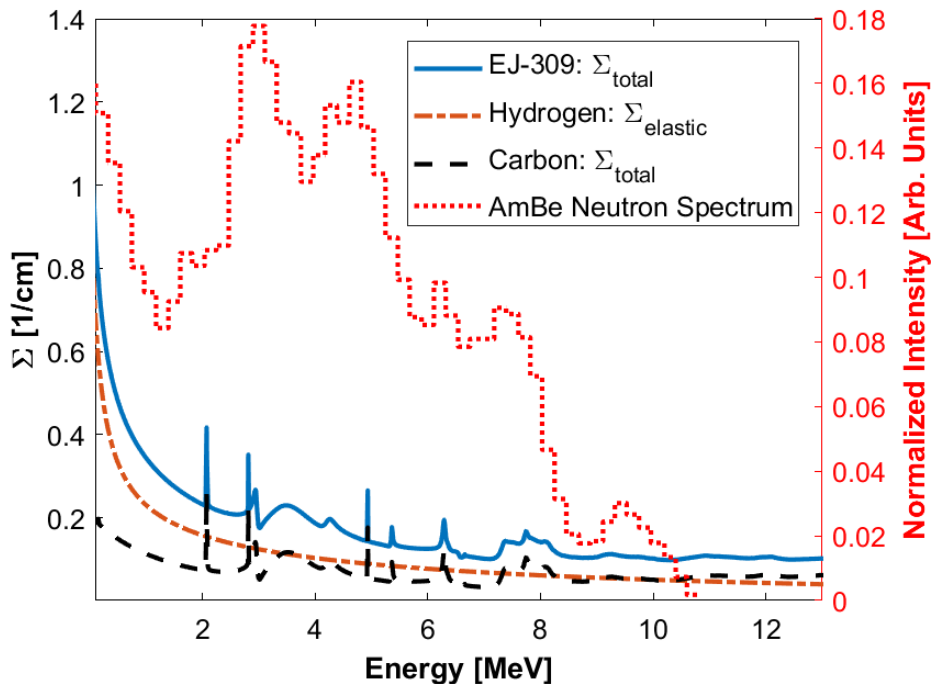
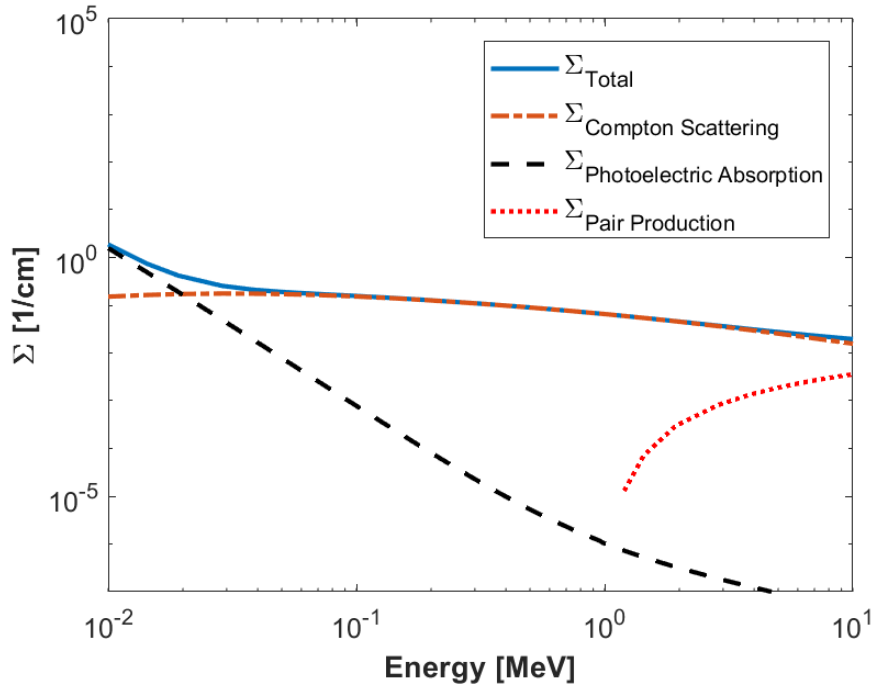


Figure 10. Macroscopic cross sections of an EJ-309 scintillator (blue) composed of carbon (black) and hydrogen (dashed orange) with a density of  $0.959 \text{ g/cm}^3$  from interpolated ENDF/B-VIII [32] nuclear data. The AmBe neutron spectrum (dotted red) from Figure 9 is overlaid to better visualize the neutron energies measured in this experiment [31].

a recoil proton with enough energy to generate a usable detector signal.

Another important feature is the cross section difference between hydrogen and carbon. Since scatter off hydrogen nuclei is more likely to generate a usable detection signal, an ideal fast neutron detector will have the highest possible hydrogen fraction to maximize the efficiency. Unfortunately, the difference between the hydrogen and carbon cross sections shrinks at higher neutron energies; therefore, the detection efficiency degrades at higher energies starting around 2.5 MeV [33].

The gamma-ray macroscopic cross section, shown in Figure 11, is just as important as the neutron cross section as it provides insight to the complex interaction types that occur in the detector active volume. At low energies, below 0.02 MeV, photoelectric absorption is dominant, and for energies between 0.02 to 38 MeV, Compton



**Figure 11. Gamma-ray macroscopic cross sections: photoelectric absorption, compton scatterings, and pair production for an EJ-309 Scintillator from the NIST Photon Cross Sections Database [34].**

Scattering is the primary interaction. The threshold for pair production is 1.02 MeV, but does not become the dominant interaction mechanism until gamma-ray energies greater than 38 MeV are reached. For this study, the energy range of interest is approximately 0.1 to 4.438 MeV, resulting in Compton scattering events being the dominant interaction mechanism inside of the EJ-309 scintillator.

### 2.5.2 Scatter Mask Material

The purpose of the scattering mask is to absorb or alter the trajectory and energy of streaming neutrons in such a way that the final DRC is direction dependent. For the Spartan Class of mask designs, the total macroscopic cross section is used as a first-order approximation for the overall effect the mask will have on streaming neutrons. Under this approximation, it is assumed any reaction inside of the mask will prevent

the neutron from reaching the active detector volume. This assumption neglects the varying neutron backscatter due to the rotating mask and surrounding environment and is only useful as a qualitative analysis of the mask material. An extremely high absorption cross section, which includes all types of absorption reactions, could be undesirable because the parasitic decrease in neutron flux incident on the detector will lead to a lower absolute detection efficiency. On the other hand, absorption reactions are the most effective, on a per neutron basis, at generating distinct wall and fin valleys of a DRC. This result is beneficial for direction identification as long as the absorption cross-section is not too high such that no events are detected because all neutrons are being absorbed at all rotational angles. Another factor considered when analyzing the scatter mask material cross section is based on Equation 3. The average energy transfer per elastic scattering event decreases as the atomic mass increases. This relationship means for higher atomic weight materials, such as lead, neutrons will lose less energy per collision while transporting through the mask compared to lighter materials like hydrogen, where potentially all of the neutron energy is transferred in a single collision. Also under the previous assumptions, the probability a neutron will scatter inside of the mask and then into the detector with enough energy to generate a detectable signal is less using hydrogen than if the mask is made of a heavier material.

For this study, the mask is three dimensional (3D) printed in VeroClear<sup>TM</sup>, produced by Stratasys and is a similar material to PMMA [35]. The actual elemental composition is proprietary; PMMA or plexiglass from the Geant4 Material Database is used for the radiation transport model for simplicity and is a potential source of model error. [17]. Table 1 lists the nominal density and the primary elemental components along with the average total macroscopic cross sections for both slow, 0.025 eV - 0.5 eV, and fast, 0.1 MeV - 11 MeV, energy neutrons. The total cross-sections are integral values calculated from the PMMA data in Figure 12 [32]. The cross

section resonances shown in Figure 12 are from the carbon and oxygen components of PMMA.

Table 1. The density and average slow (0.025 eV - 0.5 eV) and fast (0.1 MeV - 11 MeV) total neutron cross sections for the PMMA scatter mask.

Material	Density [ $\frac{\text{g}}{\text{cm}^3}$ ]	Chemical Compound	Slow Energy $\Sigma_{\text{total}}[\frac{1}{\text{cm}}]$	Fast Energy $\Sigma_{\text{total}}[\frac{1}{\text{cm}}]$
PMMA <sup>a</sup>	1.19	C <sub>5</sub> H <sub>8</sub> O <sub>2</sub>	2.349	0.313

<sup>a</sup>Nominal properties because the mask is made of proprietary material.

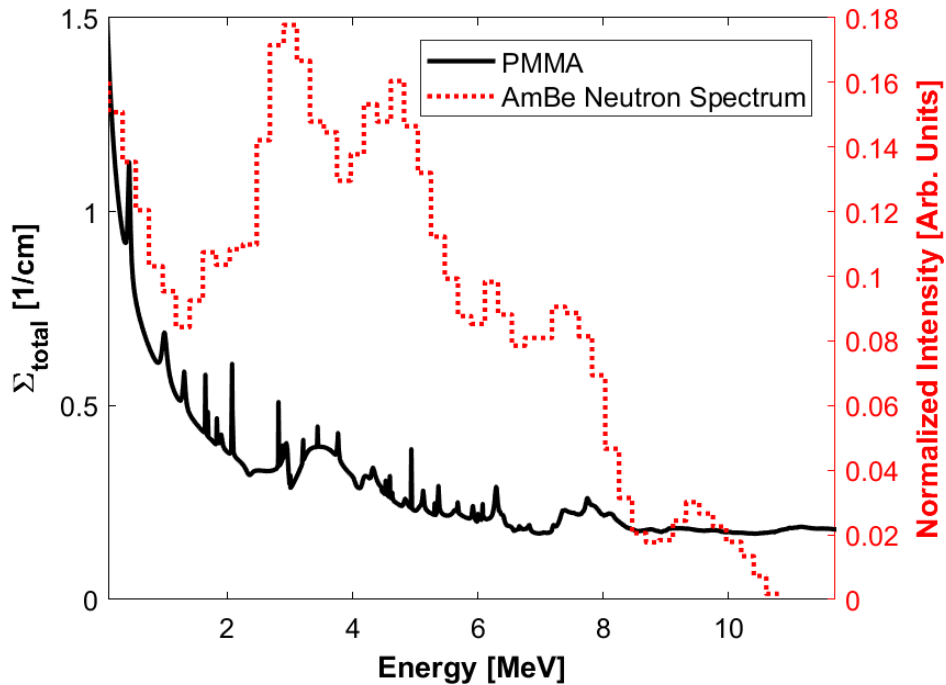
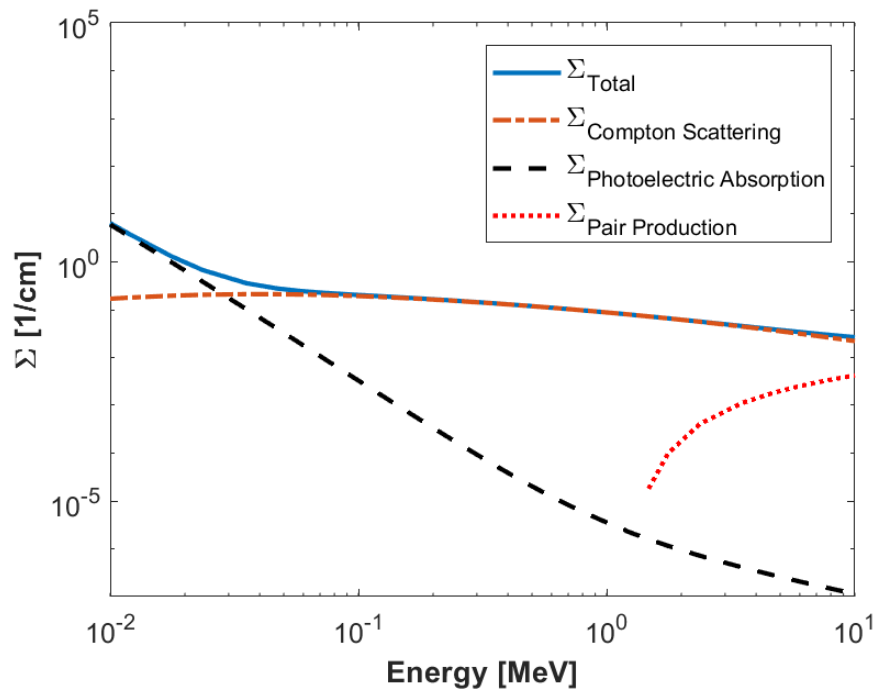


Figure 12. Total fast neutron macroscopic cross section of the PMMA scatter mask (black) composed of carbon, hydrogen, and oxygen with a density of 1.18 g/cm<sup>3</sup> from interpolated ENDF/B-VIII [32] nuclear data. The AmBe neutron spectrum (red) from Figure 9 is overlaid to better visualize the neutron energies measured in this experiment [31].

The macroscopic cross sections for gamma rays are displayed in Figure 13 for the PMMA scatter mask. These are slightly higher than the gamma-ray cross sections of EJ-309 due to the higher density and additional oxygen atoms. Again, Compton scattering is the dominant reaction mechanism over the energy range of interest, 0.1

to 4.438 MeV. This trait results in a reduction of the total number of incident gamma rays on the detector due to large angle scattering inside of the mask and also softens or lowers the energy of the gamma-ray energy spectrum reaching the detector for low-angled scatters.



**Figure 13. Gamma-ray macroscopic cross sections: photoelectric absorption, compton scatterings, and pair production for the PMMA scatter mask from the NIST Photon Cross Sections Database [34].**

## 2.6 Radiation Detection

Neutrons are detected indirectly by the collection of neutron induced charged particles. Discussed in Section 2.3, the primary reactions for detecting neutrons are scattering and secondary charged particle producing nuclear reactions. Neutron detection is divided into fast neutron detection, used for neutrons with energies above 100 keV, and slow neutron detection, used for neutrons below the cadmium cutoff energy of 0.5 eV [8]. The bounds are somewhat arbitrary and can vary based on the

detector material used, but they provide a general guide for the ensuing discussion.

Fast neutron detection, relevant to the EJ-309 scintillator used in this research, is described in Section 2.6.1, and slow neutron detection, relevant to an EJ-309 boron doped (EJ-309B) scintillator, is described in Section 2.6.2. Fast neutron detection is the focus of this study, but gamma-ray and slow neutron detection are discussed for completeness and to provide insight for future developments into both gamma-ray and fast and thermal neutron directional detection with the RSM. The scintillation process where induced charged particles and electrons are converted to collectible light photons is discussed in Section 2.6.4. In both thermal and fast neutron cases, the application of pulse shape discrimination (PSD), discussed further in Section 2.6.5, is required to separate the neutron and gamma-ray events.

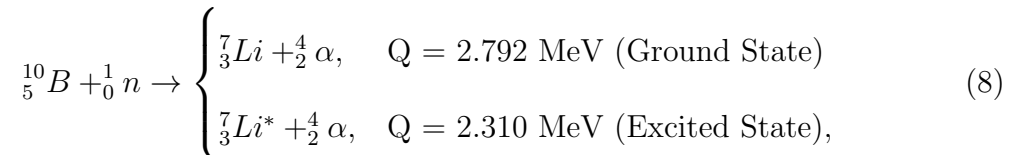
### **2.6.1 Fast Neutron Detection**

In this study, the detector conversion process for fast neutrons is light nuclei elastic scattering events in the active detector volume. To detect neutrons via elastic scattering, the incident neutron must transfer enough kinetic energy to the target nuclei. Possible target light nuclei for the production of recoil charged particles are hydrogen, deuterium, and helium. Hydrogen is the most popular because it has the highest energy transfer per collision ratio and is the main component inside of the EJ-309 scintillator. In EJ-309 scintillators, a fast neutron elastically scattering off hydrogen leads to a recoil proton detectable through scintillation of the active detector volume. Details are described further in Section 2.6.4.

### **2.6.2 Slow Neutron Detection**

The EJ-309 scintillator is a fast neutron detector but when doped with  $^{10}\text{B}$  has slow neutron detection capabilities. At low neutron energies, the  $^{10}\text{B}$  capture macroscopic

cross section becomes dominant and leads to the charged particle producing reaction [8]



used to detect slow neutrons. For thermal neutron energies, the  ${}^7\text{Li}$  ion is released in an excited state 94% of the time and quickly decays to the ground state in approximately  $10^{-13}$  seconds with the emission of a 0.48 MeV gamma ray that is assumed to escape [8]. At such low energies, the kinetic energy of the incident neutron is negligible, and the detector light energy spectrum for slow neutrons would consist of  ${}^7\text{Li}$  and  $\alpha$  peaks and would be used for generating slow neutron DRCs. From a nuclear safeguards application standpoint, SNM is often stored in some sort of shielding capsule that softens or thermalizes the emitted fast neutrons. Having the ability to detect slow neutrons increases the signal available for directional detection of neutron sources of interest.

### 2.6.3 Gamma-Ray Detection

Gamma rays are detected with an EJ-309 scintillator through Compton scattering events. Compton scattering generates electrons with energies dependent on the scattering angle, calculated using Equation 5. Similar to protons, the electrons will cause the EJ-309 to scintillate, and the photons generated are collected in the photomultiplier tube (PMT). The application of PSD techniques, described in Section 2.6.5, can allow for the separation of neutron and gamma-ray events to produce independent neutron and gamma-ray event DRCs as a function of rotational angle to determine the source direction.

#### 2.6.4 Scintillation Process

The previous three sections discussed the production of charged particles induced by neutrons and gamma rays for an EJ-309 and EJ-309B scintillator, which are then converted into a usable detector signal through charge scintillation mechanisms. There are three processes for absorbing ionizing radiation and emitting light photons inside of a scintillator: fluorescence, phosphorescence, and delayed fluorescence. Fluorescence is the prompt emission of light photons, and delayed fluorescence is the same process as fluorescence except with a longer emission time [8]. Phosphorescence leads to the emission of photons with longer wavelengths than fluorescence. All three processes lead to the emission of light photons, collectible by a PMT. Light photons generated from the three processes traverse through the scintillator and interact via the photoelectric effect at the photocathode of the PMT producing photoelectrons. These photoelectrons are then accelerated into an adjustable configuration of dynodes resulting in a cascade amplification of the free electron population that is finally collected by an anode. This process produces the detector output signal for digital signal processing and PSD [8].

A simplified demonstration of the material excitation process for organic scintillators with a  $\pi$ -electron structure is illustrated in Figure 14. Induced charged particles in the scintillation material transfer kinetic energy to the surrounding molecules through Coulombic interactions thereby exciting valence band electrons to various excited states. In Figure 14, singlet states,  $S$ , are described by their spin state, denoted by an  $S_0$ ,  $S_1$ ,  $S_2$ , and  $S_3$ , and their vibrational states, denoted as the second subscript as  $S_{00}$ ,  $S_{01}$ ,  $S_{02}$ , etc. The absorption of kinetic energy results in excitation to higher states (blue arrows). The energy difference between  $S_0$  and  $S_1$  is between 3 to 4 eV, and the energy spacing for higher states is slightly smaller. Energy states higher than  $S_1$  de-excite quickly,  $\sim 10^{-12}$  s, to the  $S_1$  state through radiationless inter-

nal conversion, and any excess vibrational energy is also quickly lost through phonon emission.

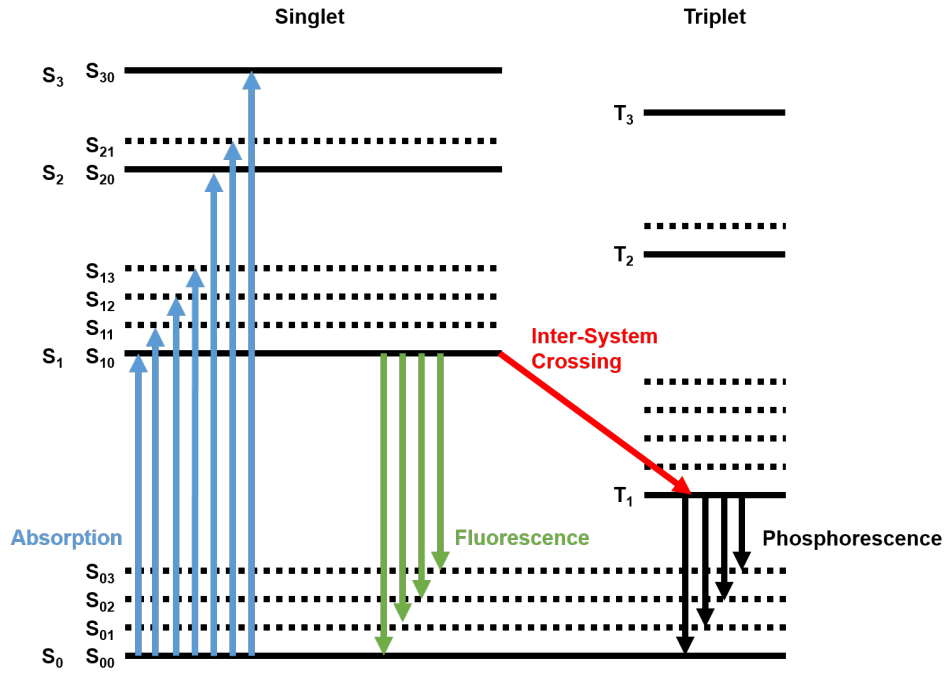


Figure 14. Energy levels of an organic molecule with a  $\pi$ -electron structure to illustrate the electron excitation process that produces collectible light photons for scintillation detection [8].

After a negligible period of time, the bulk of the excited molecules are in the S<sub>10</sub> state. From here, prompt fluorescence can occur (green arrows) to the ground state with an intensity,  $I$ , as a function of time,  $t$ , as described by

$$I = I_0 e^{-\frac{t}{\tau}}, \quad (9)$$

where  $\tau$  is the decay constant and a common documented performance parameter for different scintillation materials. Through a process called inter-system crossing (red arrow), some excited states are converted to triplet states, T<sub>1</sub> with lifetimes as long as  $10^{-3}$  s. T<sub>1</sub> states de-excite through the emission of phosphorescence photons (black arrows), which are delayed and have longer wavelength compared to photons

generated from fluorescence. There is also a non-zero probability of molecules in the  $T_1$  state thermally exciting back up to the  $S_1$  state. The resulting decay of the  $S_1$  state is called delayed fluorescence and has a lifetime longer than fluorescence, a few nanoseconds, but shorter than phosphorescence.

All but the  $S_{10}$  to  $S_{00}$  fluorescence transitions produce photons with lower energies than the required excitation energies, resulting in very little self-absorption of the fluorescence light photons. Any process leading to the loss of light photons through self-absorption or radiationless de-excitation are classified as quenching. The overall light yield from this scintillation process is dependent on the initial charged particle induced by neutron or gamma-ray interactions allowing for PSD, discussed next.

### 2.6.5 Pulse Shape Discrimination

The light and pulsed signal output of scintillators vary for different types of charged particles. This characteristic allows for incident radiation particle discrimination through PSD. For an EJ-309 and EJ-309B scintillator, the primary-secondary charged particles are electrons for incident gamma rays, protons for fast neutrons, and both  ${}^7\text{Li}$  ions and  $\alpha$  particles for slow neutrons. The fraction of kinetic energy converted into light, known as the scintillation efficiency, is dependent on both the particle type and energy. Figure 15 shows the scintillator response as a function of particle energy of an NE-102 organic scintillator, similar in composition to an EJ-309 scintillator. For organic scintillators, like NE-102 and EJ-309, the response of electrons is linear for particle energies greater than 125 keV [8]. In addition, the scintillation efficiency decreases as a function of the particles mass, another factor driving the use of low-Z materials for recoil detectors.

The implication of Figure 15 is that the same energy neutron and gamma ray will result in different amounts of collected light at the PMT's photocathode. To

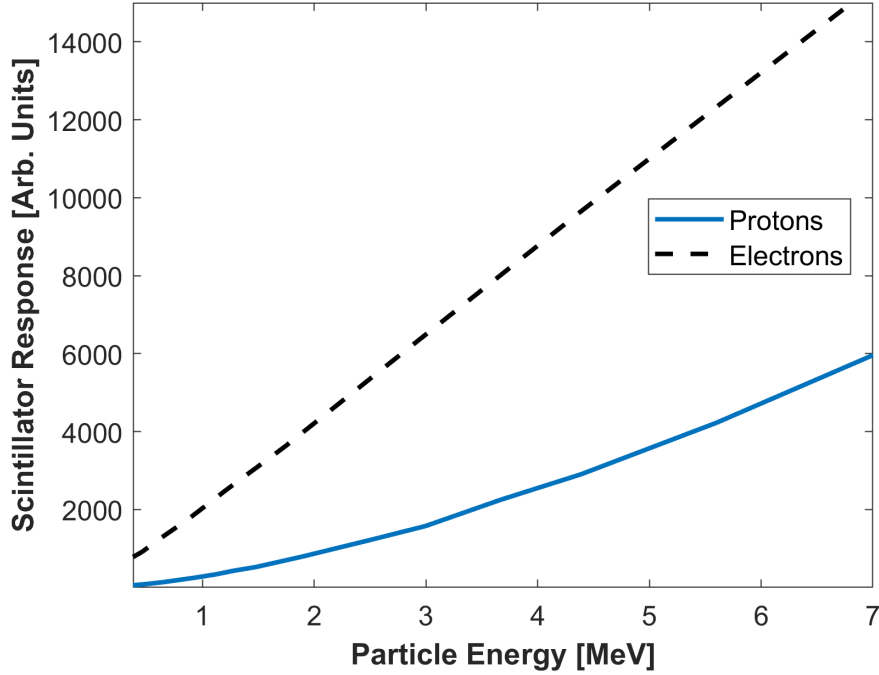


Figure 15. An example of the energy and particle dependence light yield of a plastic organic (carbon and hydrogen based) scintillator, NE-102, where it is seen that the energy to light conversion is significantly less efficient and non-linear for protons compared to electrons [8].

describe the absolute light yield using a common unit, the energy-dependent response is typically mapped to MeV or keV electron equivalent (MeVee or keVee) units. This is accomplished using a light conversion function to convert between MeV and MeVee for all secondaries other than electrons. This study utilized a relationship known as Birks' formula, Equation 10, to convert the energy deposition of recoil protons,  $E_p$  in MeV, to an electron equivalent light yield,  $L(E_p)$  in MeVee [8, 36].

$$L(E_p) = \int \frac{a}{1 + b \frac{dE}{dx}} dE \quad (10)$$

Birks' formula relies on the assumption that there is a high ionization density along the protons trajectory leading to quenching from damaged molecules resulting in a lower scintillation efficiency. The parameters  $a$  and  $b$  are system dependent and

used as adjustable fit parameters to better match simulated data to experimental. The proton stopping power,  $\frac{dE}{dx}$  in units of  $MeV/(mg/cm^2)$ , is incorporated when using Birks' formula to capture the varying changes as a function of particle energy. Figure 16 displays both the proton and electron stopping power used throughout this work obtained from the NIST ESTAR database and The Stopping and Range of Ions in Matter (SRIM) software package [36–39].

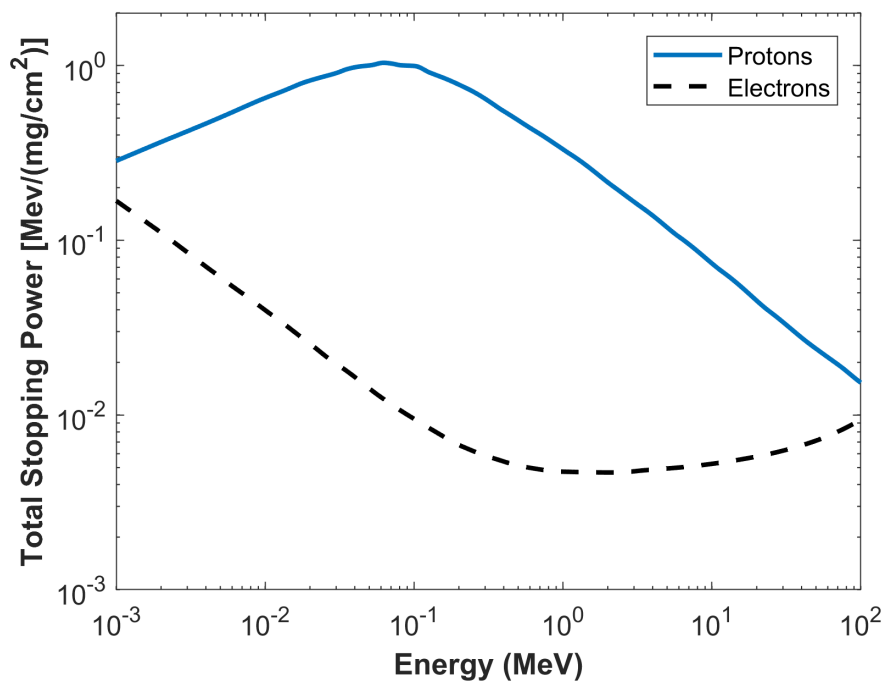


**Figure 16.** Energy dependence of the total stopping power for both protons and electrons, obtained from the NIST ESTAR database and SRIM software package [36–39].

Additionally, there is a particle dependent timing response of the scintillation material allowing for particle type determination. An additional timing component is added to Equation 9, to account for the intensity rise and decay of an induced pulse,

$$I = I_0(e^{-\frac{t}{\tau}} - e^{-\frac{t}{\tau_1}}) \quad (11)$$

where the new  $\tau_1$  parameter represents the signal rise time of the scintillation mate-

rials. The prompt fluorescence process component generates most of the scintillation light and is on the order of a few nanoseconds, but a slower component is observed from delayed fluorescence on the order of several hundred nanoseconds creating a long-lived tail in the response signal. The long-lived tail is dependent on the excitation particle. This phenomenon is illustrated in Figure 17 for an organic stilbene scintillator, where the induced gamma-ray pulses decay much faster than neutron and alpha particle induced pulses. The phenomena of particle dependent decay times arises due to the slow component depending on the linear energy loss rate  $\frac{dE}{dx}$  of the induced charge particles: electrons, recoil protons, and heavy charged particles (HCPs). Higher energy loss rates, found with increasing  $Z$  of the charged particle, result in an increase in delayed fluorescence probability.

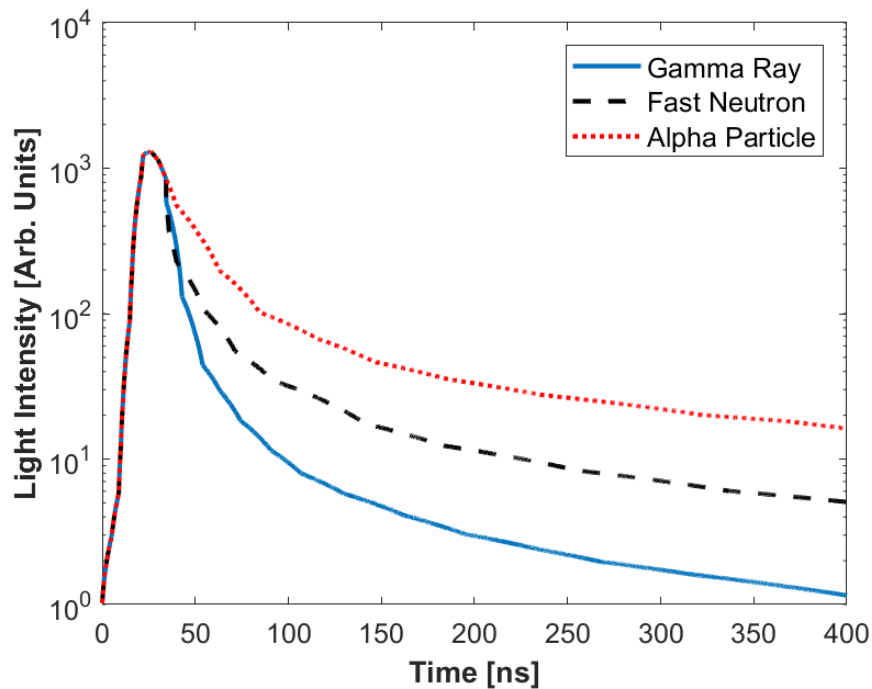


**Figure 17.** Induced particle dependent light intensity timing Plots for stilbene, an organic plastic scintillator [8]. A clear distinction between gamma rays, fast neutrons, and alpha particles are seen allowing for PSD techniques to be applied for separating events.

Calculated PSD ratios are used to generate histograms for discriminating between

neutron and gamma-ray induced events. PSD ratio calculations using the shape of the induced pulse waveforms are made by implementing the Tail-to-Total method defined as

$$PSD = \frac{Q_{Long} - Q_{Short}}{Q_{Long}}, \quad (12)$$

where  $Q_{Long}$  and  $Q_{Short}$  are the total integrated charge from detector waveforms using fixed long and short timing gates, respectively. An example waveform induced by a gamma ray used for calculating the PSD ratio is shown in Figure 18 where the short gate (blue) is an integration window over the prompt portion of the waveform to obtain  $Q_{Short}$ , and the long gate (red) is an integration window over the whole detected waveform to calculate  $Q_{Long}$ .  $Q_{Long}$  represents the total integrated charge, and the subtraction of  $Q_{Short}$  to  $Q_{Long}$  represents the decaying tail of the waveform, hence called the Tail-to-Total method.

For each waveform collected, a PSD ratio is calculated using Equation 12 and then plotted as a function of the total integrated area or charge of the waveform as shown in Figure 19 known as a two-dimensional (2D) PSD histogram or PSD ratio density plot. In Figure 19 the total integrated charge can later be converted to total light yield through a detector calibration. The PSD ratio density plot shows a clear differentiation of neutron and gamma-ray induced events.

Collapsing the PSD ratio density plot along the y-axis, generates a one-dimensional (1D) histogram of the PSD ratio frequency, Figure 20, to quantify the number of gamma-ray and neutron events. A double Gaussian fit to Figure 20 is used to calculate the total number of neutron and gamma-ray events. Particle-type dependent RSM DRCs are then generated by pairing the total number of particle events with the corresponding mask rotational angle bin,  $\theta$ .

The 1D histogram in Figure 20 can also be used to quantify the PSD performance.

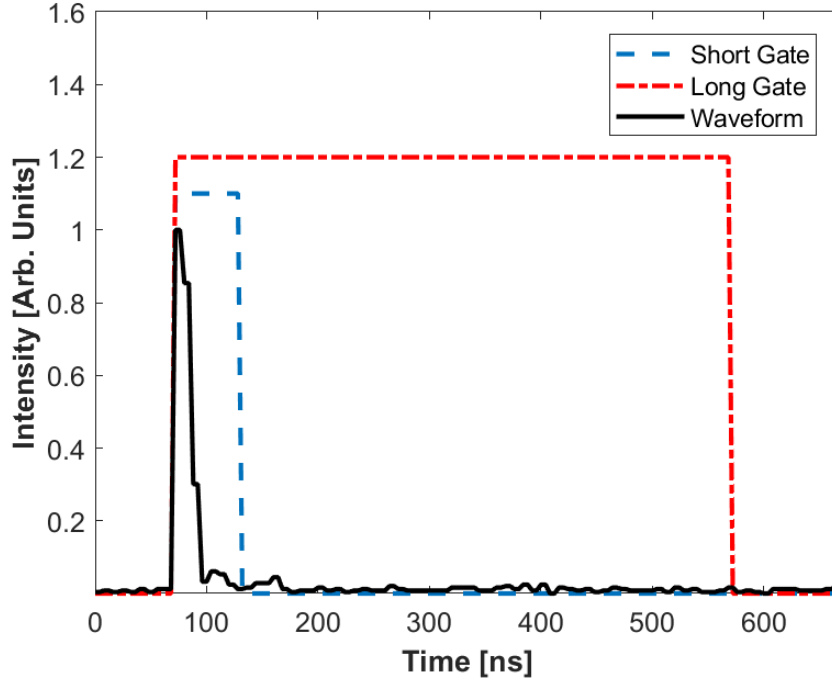


Figure 18. An example of a collected waveform induced by a gamma ray using an EJ-309 scintillator. The short gate (blue) and long gate (red) are integration windows to obtain  $Q_{Short}$  and  $Q_{Long}$ , respectively, for calculating PSD ratios.

A figure of merit (FOM) to quantitatively represent the PSD performance of the system is defined as the ratio of the difference in peak centroids,  $C_{neutrons}$  and  $C_{gamma}$ , to the sum of the full-width-half-maxima (FWHM) of the two peaks,  $FWHM_{neutron}$  and  $FWHM_{gamma}$ , shown in Equation 13.

$$FOM = \frac{C_{neutron} - C_{gamma}}{FWHM_{neutron} + FWHM_{gamma}} \quad (13)$$

Due to the curvature in the density plot particle clusters of Figure 19, a curved energy-dependent discrimination cut is applied to separate gamma-ray and neutron events.

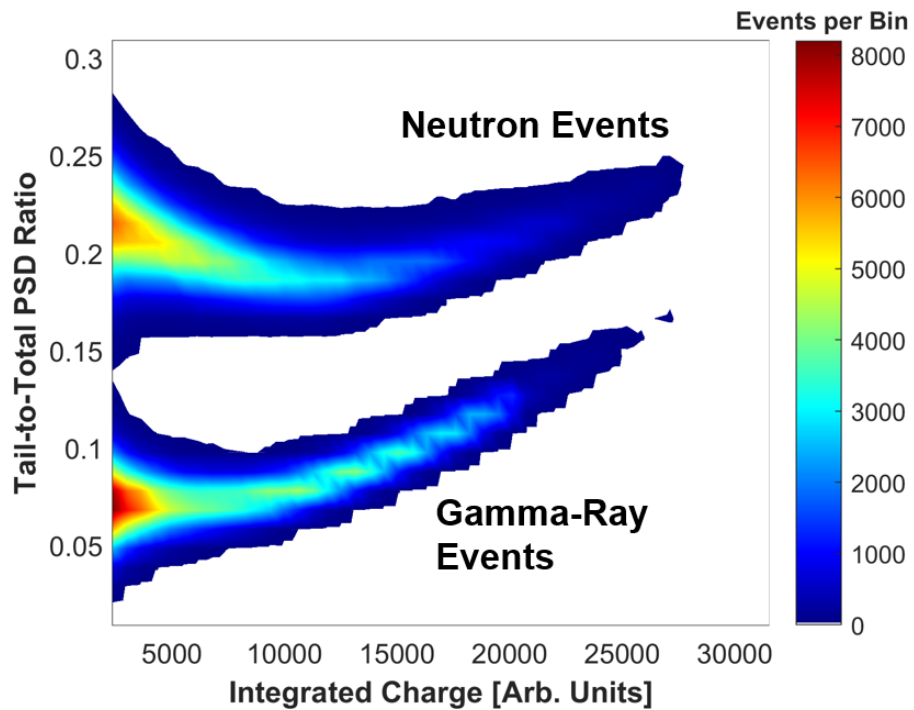


Figure 19. An example PSD ratio density plot, also called a 2D PSD histogram, generated by measuring an AmBe neutron source with an EJ-309 scintillator. A clear distinction between neutron and gamma-ray induced events are observed, and the curvature of each cluster is due to non-linear over amplification of the induced detector signal output from the PMT.

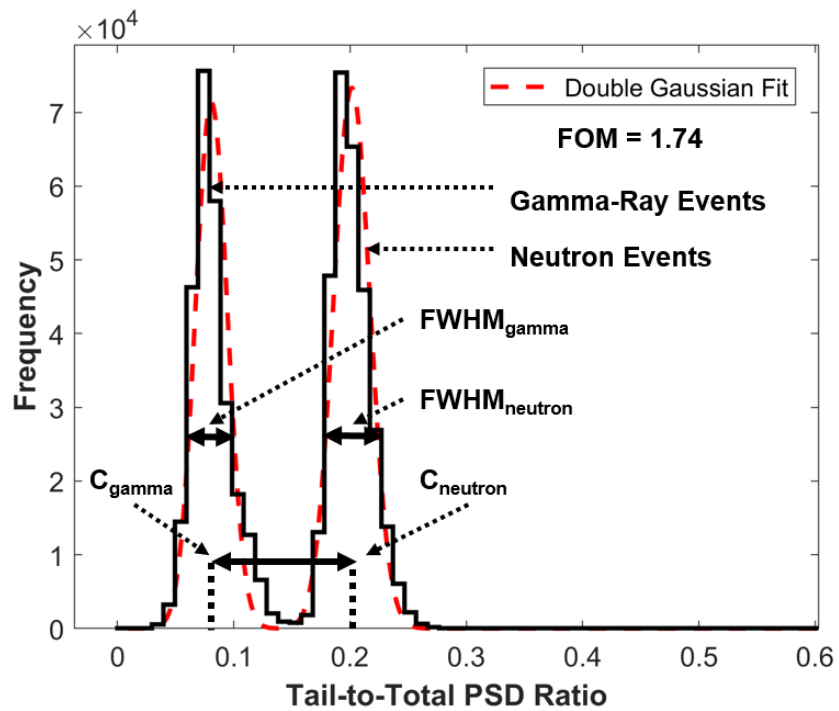


Figure 20. Double Gaussian fitted PSD ratio histogram generated by measuring an AmBe neutron source with an EJ-309 scintillator. The integration of each Gaussian fit is used to determine the number of neutron and gamma-ray events, and a PSD performance FOM is calculated using Equation 13.

## 2.7 Quantitative Metrics for Distribution Comparisons

This study involves comparing both Geant4 simulated and experimentally measured DRCs for determining the direction of an AmBe source with the neutron RSM system. Thus, statistical tests are required to validate and quantify the quality of the simulated results with reality. The analysis utilizes two statistical tests to compare the simulated and experimental data, the Modal Assurance Criterion (MAC) and  $\chi^2$  Goodness of Fit Test. Also, the relative percent difference is calculated for all comparisons. These tests are implemented to validate the Geant4 model and quantify discrepancies in the pulse-height energy spectra and DRCs. Two additional imaging algorithms, other than the Spartan method discussed in Section 2.1.2, utilize the MAC or  $\chi^2$  comparisons to determine the direction of a radiation source by comparing simulated DRMs for all source directions to a measured DRC, as done in previous RSM research [11, 12, 14].

### 2.7.1 Modal Assurance Criterion

The MAC is used as a quantifiable statistical indicator for the similarities in the modal shape of two distributions such as Geant4 and experimentally generated DRCs. This test is most sensitive to large discrepancies in modal shape, while relatively insensitive to small differences [40]. The MAC value, Equation 14 [11, 13], is bounded between 0 and 1, where a MAC value of 1 means the modal shapes are 100% similar, and 0 indicates that the shapes are orthogonal or inconsistent with each other.

$$MAC_{\theta,\varphi} = \frac{(\mathbf{u}_{\theta,\varphi}^T \mathbf{v})^2}{(\mathbf{u}_{\theta,\varphi}^T \mathbf{u}_{\theta,\varphi})(\mathbf{v}^T \mathbf{v})} \quad (14)$$

$MAC_{\theta,\varphi}$  represents the normalized scalar product of two vectors [40]: the simulated normalized DRC,  $\mathbf{u}_{\theta,\varphi}$ , for a specific source direction, and the experimentally mea-

sured normalized DRC,  $\mathbf{v}$ . The same calculation is performed analogously for pulse-height energy spectra as well. The DRCs are mean-reduced, which entails subtracting each element of a DRC by the mean value, centering the curve about zero vertically and increasing the variance of the calculated MAC values to improve imaging capabilities. A MAC matrix is then generated by calculating the MAC values for all directions in the simulated DRM, where the highest MAC value represents the simulated DRC that is most similar to the experimental measurement and the predicted source direction.

### 2.7.2 Chi-Squared Test

In addition to the MAC comparison, a frequency comparison is required to further validate the Geant4 model with experimental results, and thus the  $\chi^2$  Goodness of Fit Test is applied for a more thorough statistical comparison [41, 42]. The  $\chi^2$  Goodness of Fit Test is used to compare experimental and simulated data sets quantifying the level of agreement by accounting for the square of the residuals and the uncertainty in the experimental data.  $u$  and  $v$  represent Geant4 simulated and experimental distributions, respectively, and is used to calculate a test statistic.

$$\chi_1^2 = \sum_{i=1}^n \frac{(u_i - v_i)^2}{\sigma_i^2} \quad (15)$$

This calculation assumes that the pulse-height energy spectra and each integrated particle event count extracted from a 2D PSD histogram follow a Poisson or Gaussian distribution such that the uncertainty in each measurement,  $\sigma_i$ , is equivalent to the square root of the counts in a given bin [8]. The  $\chi^2$  statistic is modified by dividing by the total number of degrees of freedom minus 1,  $\nu$ , to obtain the reduced  $\chi^2$ , which is the quoted metric in Chapter 4. This value allows for comparing the statistical level of agreement for multiple  $\chi^2$  Goodness of Fit Tests by removing the degree of

freedom dependence on the  $\chi^2$  statistic. An ideal reduced  $\chi^2$  value is equivalent to one. Values greater than one represent a poorer fit, and values less than one are considered to be an over-fit [41]. For the comparisons made throughout this study, the goal is to obtain a reduced  $\chi^2$  value close to 1.

### 3. Methodology

The Spartan I scatter mask performance for the detection system discussed in Section 3.1 is tested both computationally and experimentally to confirm the system’s directional detection capabilities. Developing a robust radiation transport model in Geant4 and then providing an experimental validation allows for future optimization and parameter studies to be computationally performed saving both time and financial resources. Two DRCs are obtained for the experimental validation for both neutrons and gamma rays. To enhance the reproducibility of this work, the systematic approach used to demonstrate this proof-of-concept neutron RSM directional detection system is outlined in Figure 21 .

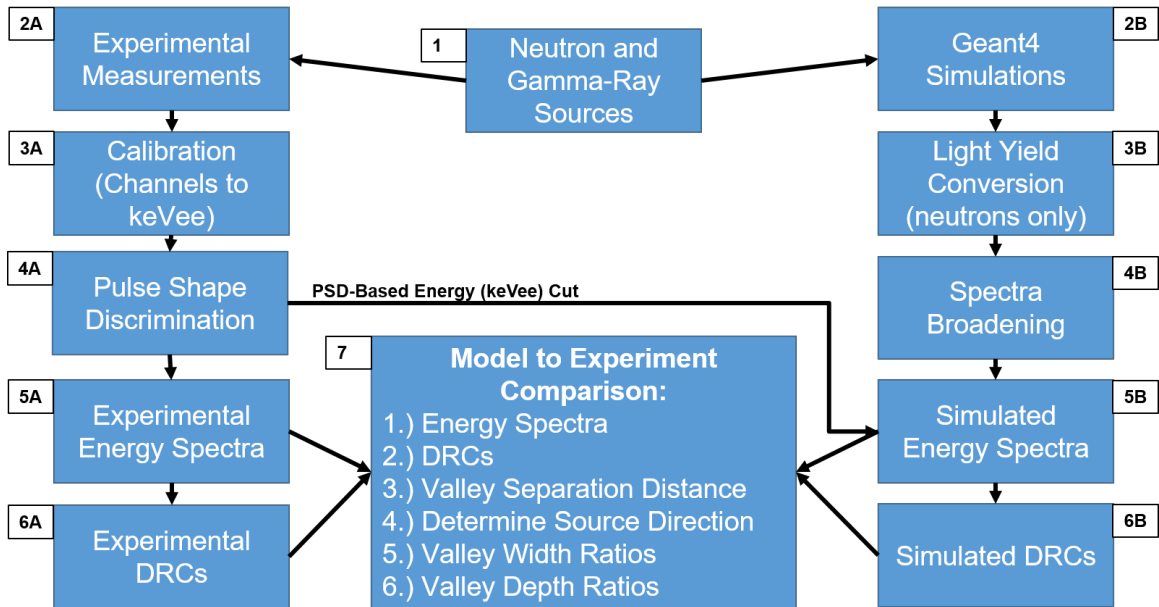


Figure 21. Neutron RSM directional detection validation and verification flowchart.

Starting with Step 1, various neutron and gamma-ray sources are selected for the study. Both are experimentally measured in Step 2A and simulated using Geant4 in Step 2B. For Step 3A, select gamma-ray sources are used to calibrate the EJ-309 detector. Only for neutron simulations, the proton energy deposition must be

converted to an electron equivalent light yield using Equation 10, Step 3*B*, before broadening the simulated spectra for both neutrons and gamma rays, Step 4*B*. The simulation assumes perfect energy deposition thereby missing the imperfect resolution of real detection systems, thus the resolution function is used to broaden the simulated energy deposition histograms, Step 4*B*, to better model the experimental outcomes. PSD techniques can then be applied, Step 4*A*, to separate neutron and gamma-ray events. These events can then be used to obtain particle dependent energy spectra, Step 5*A*, and experimental DRCs, Step 6*A*. Next, the simulated neutron and gamma-ray energy spectra are generated, Step 5*B*. Using the experimental PSD electron equivalent energy cutoff, simulated DRCs are generated in Step 6*B*. Finally, Step 7 is accomplished by applying the statistical comparison metrics discussed in Section 2.7 to quantify how well the simulated results match the experimental data along with identifying the source’s direction using the Spartan Method.

### 3.1 Scatter Mask Design

The Spartan I scatter mask geometry, originally created and characterized by Holland, Martin, and Olesen in previous work, uses a voxel method where a 2D design matrix, shown in Figure 22, is converted into a 3D mesh [12, 13, 20]. Each block of the design matrix represents a  $10^\circ$  voxel in  $\theta$  and  $\phi$ , and the color signifies the thickness of the mask material between the center of the cylindrical detector and the center of each voxel. The black voxels represent the lateral wall thickness of 7.5 cm, the blue voxels create the rotational fin thickness of 5 cm, and the white voxels represent the base mask thickness of 0.81 cm.

The dashed red double-headed arrow represents the geometrical angular separation between the center of the wall to the center of the fin,  $\Delta\theta$ . This distance is the fundamental characteristic of the Spartan I mask used to identify a source’s  $\phi$

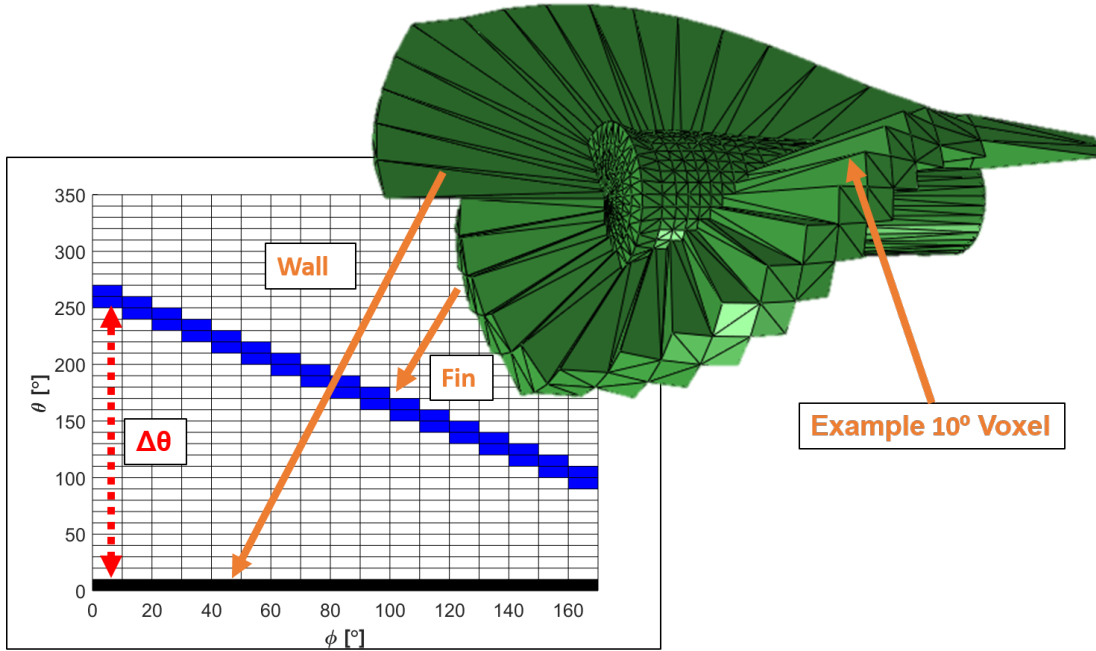


**Figure 22.** Spartan I 3D SolidWorks model overlaying the 2D design matrix used to generate the mask. The dashed red double-headed arrow represents the linear decrease in separation of the wall and fin as a function of  $\phi$  [13].

direction as previously mentioned in Section 2.1.2. Assuming sufficient statistics are obtained such that the DRC has a converged solution, the DRC is primarily dependent on the thickness of mask material between the source and detector. The ideal Spartan I linear equation is given as

$$\phi = -(\Delta\theta) + 260^\circ. \quad (16)$$

Figure 22 also contains an overlay of the SolidWorks mask model, which represents the 3D mesh generated by creating a stereolithography (.stl) file using Abaqus to pair each element of the design matrix to a 3D node. The .stl model is used to 3D print the mask. Figure 23 is a photograph of the mask being printed at AFIT. The total time between placing the 3D print order and delivery of the final product is 6 days, exemplifying the ability to quickly test various complex mask designs and additive manufacturing materials.

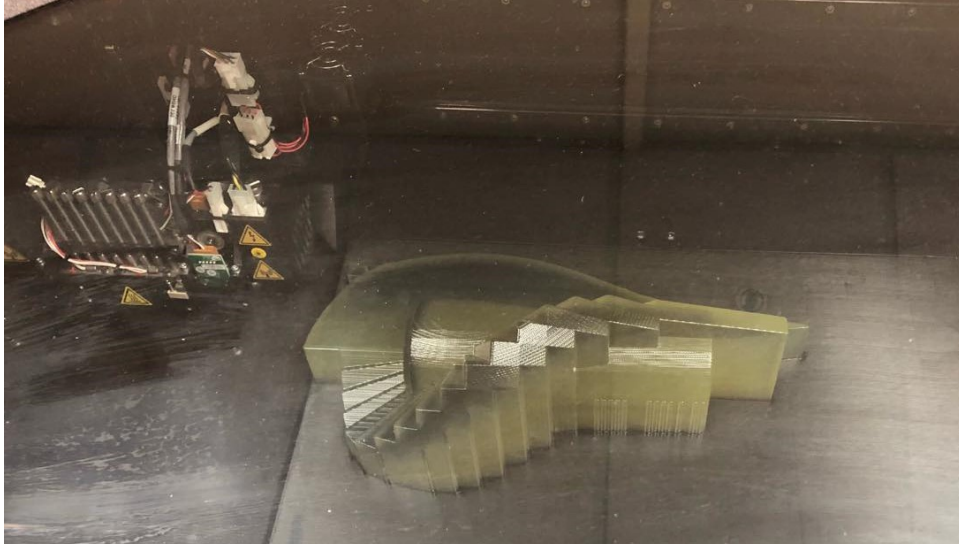


**Figure 23.** The Spartan I mask for the neutron RSM directional detection system being 3D printed at AFIT in VeroClear™, a material similar to PMMA.

## 3.2 Experimental Measurements

### 3.2.1 System Design

The RSM system is composed of three main parts: the radiation detection equipment, the rotational motor system, and the mask. A labeled image of the RSM system is shown in Figure 24. The radiation detection system consists of an Eljen Technology 1" EJ-309 scintillator coupled with a Hamamatsu R6094 PMT connected to a CAEN DT5790 digital pulse analyzer (DAQ). The PMT is encased in a custom assembly mounted to the scintillator and placed inside of the detector holder where the two are held firmly together using a spring system and secured inside of the Polycase assembly box. Surrounding the detector holder, but not touching, is the mask holder clamped internally to a plastic rotating gear. Inside of the assembly box is the rotational motor system consisting of a stepper motor and gear system connected to the mask and powered by a 40 Volt battery [20]. In the future, the system will be programmed by an installed Raspberry Pi for portability, but for this work a personal computer is used [43]. Characteristics such as the battery lifetime, maximum

and minimum rotational velocity, and use of the encoder ring for the motor rotational angle have yet to be determined and will be a priority in future work to make the system deployable in the field.

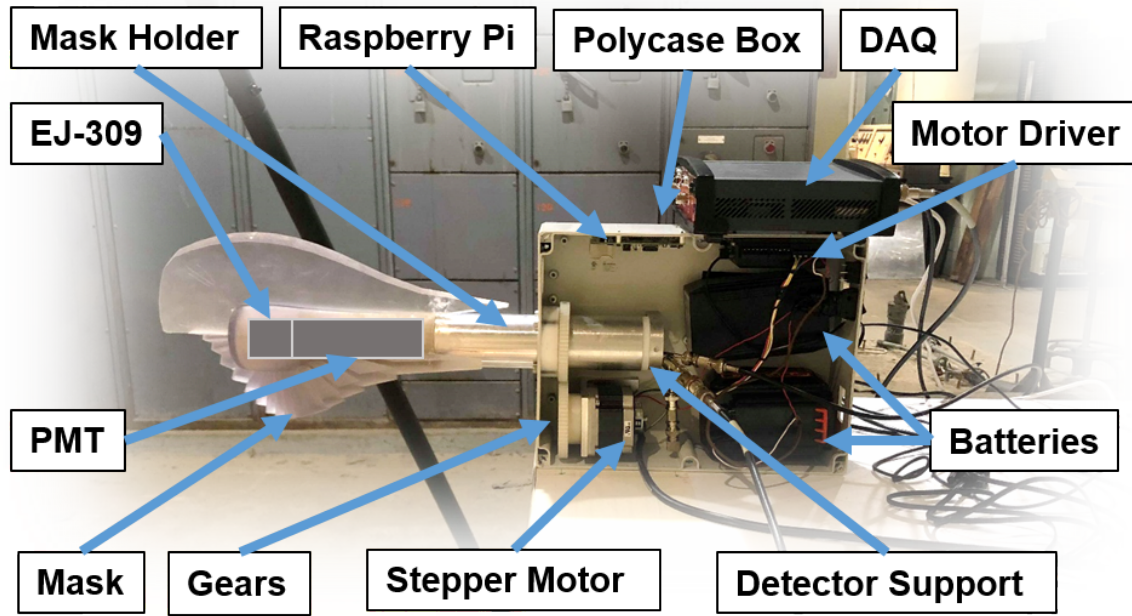


Figure 24. A labeled image of the RSM system. The EJ-309 scintillator and PMT are represented as gray rectangles, and the wiring has been removed from the Polycase box for a better viewing of the internal components.

### 3.2.2 Experimental Setup

The neutron RSM validation experiment consisted of performing a detector calibration using the Compton edges of multiple gamma-ray sources ( $^{137}\text{Cs}$ ,  $^{60}\text{Co}$ , and  $^{22}\text{Na}$ ), and two directional measurement sets using an AmBe neutron source. First, the calibration measurements are taken for 12 hours, where the mask is removed to prevent gamma-ray attenuation. Then, two sets of directional measurements are performed. Each set of measurements consisted of 36 individual 30-minute measurements with the mask attached but stationary. After each 30-minute measurement, the mask position is incremented  $10^\circ$  in  $\theta$ . Stationary measurements allowed for a more direct

comparison of the model and simulation, while a rotating measurement would require a constant angular binning of each detected event. This can lead to deviations from the model if not done correctly, which would affect the primary objective of this research to verify the ability to determine the direction of a source and validate the Geant4 model. Future work will need to incorporate real-time angular rotation and binning. Additionally, for each directional measurement set, one measurement is taken with the mask rotating at 0.0139 revolutions per second and one measurement with the mask removed. This allowed for a relative percent efficiency loss calculation to be made, due to the addition of a scatter mask over the detector.

An example directional measurement setup is shown in Figure 25, where the RSM rested 87 cm above the concrete floor on a wooden table, the source is hung by a tripod, and sheets of cadmium are placed around the Polycase box and table to reduce neutron backscattering effects. The tripod stood approximately 2.6 cm high, allowing for the source to be hung in the open air, and additional sheets of cadmium were taped to each leg. The entire setup is created using a tape measure, laser distance measurer, and a laser leveler where the human error is assumed to be less than 1.27 cm in all directions.

The Digital Pulse Processing for Pulse Shape Discrimination (DPP-PSD) software provided by CAEN is used for all measurements. The acquisition settings for the experiment along with a full description of each radiation source are found in Appendix A and B, respectively [44]. These measurement sets result in particle dependent DRCs to compare with Geant4 simulated DRCs.

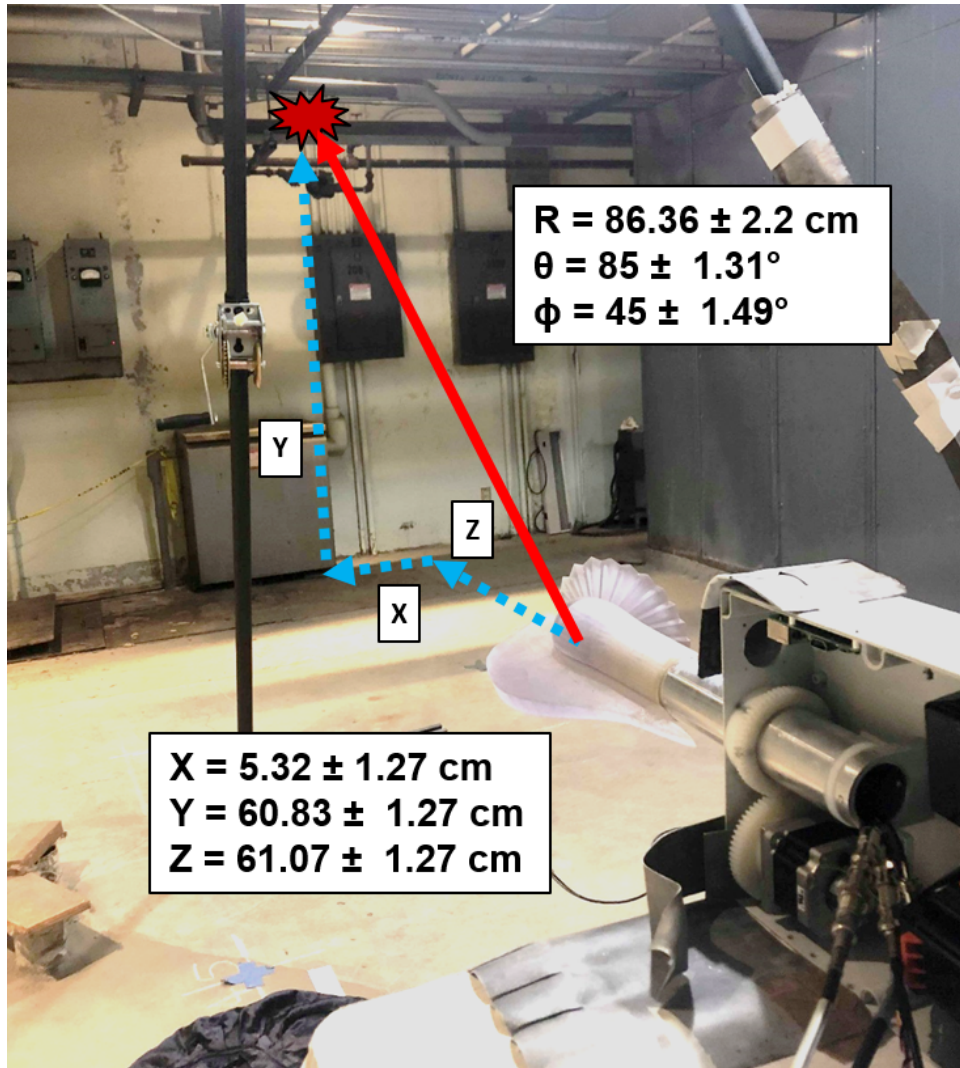


Figure 25. Example directional measurement of an AmBe source placed 86.36 cm away from the neutron RSM system at a direction of  $\theta = 85^\circ$  and  $\phi = 45^\circ$ . Thirty-six stationary 30-minute measurements are taken, rotating the mask  $10^\circ$  between each measurement to generate an experimental DRC.

### 3.3 Radiation Transport Model

#### 3.3.1 Geant4 Toolkit

Two primary methods exist to model radiation transport. The deterministic approach numerically solves the Boltzmann transport equation, while the stochastic or Monte Carlo approach utilizes the probabilistic nature of radiation particle transport. For this study, the RSM system is modeled using a Monte Carlo transport toolkit, Geant4, to emit the neutrons and gamma rays from a point source, transport them through the RSM system, and track the reaction history, including the production of secondary particles. Geant4 is an object-oriented C++ transport code developed by the European Organization for Nuclear Research (CERN) [17].

Monte Carlo particle transport relies on generating probability distribution functions to sample parameters such as the particle emission energy, initial direction, transport distance, reaction type, energy transfer, and recoil direction after a collision. Geant4 allows the user to extract a wide array of static and time-dependent information: energy deposition into any user-defined object, reaction types, position, momentum, and speed. For this study, the extracted information is the energy deposition of secondary protons and gamma rays inside of the active detector volume to generate both energy deposition histograms and DRCs.

#### 3.3.2 Rotating Scatter Mask Simulation

The directional neutron RSM detection system is modeled using a modified simulation package developed by Holland and Logan, consisting of multiple Python modules, shell scripts, and a Geant4 RSM model originally designed for gamma-ray transport. The package allows the user to adjust the Geant4 RSM model and automate the transport simulation runs. Additionally, the package generates the DRM by varying the source position, defined by  $\theta$  and  $\phi$ , to cover a FOV of  $360^\circ$  in  $\theta$  and  $5^\circ$  to  $165^\circ$

in  $\phi$ . Note that for the simulation, the source is rotated while the mask remained stationary; experimentally the mask rotates and the source is assumed to be stationary. This reduces the overall simulation run-time because adjusting the source position does not require the program to adjust the mask geometry and re-compile each model. A full  $4\pi$  FOV is not used to reduce the full simulation time because the Spartan I FOV has been shown to be limited to  $25^\circ$  to  $165^\circ$  in  $\phi$ , currently one of the drawbacks of this mask design. The primary parameters and settings used for the Geant4 model are summarized in Table 2.

A simplified geometry is used for the RSM system. Only components holding the detector and mask are included, and the motor, gears, and electronics are neglected. Figure 26 displays all of the model components except for the active detector volume, scintillator window, and PMT which are all enclosed inside of the PMT and scintillator cell casing. The dotted arrows signify how the PMT and scintillator cell casing go inside of the detector holder which slides through the mask holder attached to the mask itself. Unseen in Figure 26, there is a small air gap, less than a millimeter thick, between the detector holder and mask holder which allows the physical mask to rotate while the detector remains stationary.

The materials and densities used in the model are listed in Table 3. For all but the mask and PMT material, the default densities from the Geant4 Material Database are used [17]. Two simplifications are made for the material composition of the mask and PMT, which could potentially be sources of error in the simulation results. The material used for the PMT is classified as a pseudo-PMT material made of iron with a significantly lower density. For the 3D printed mask mentioned previously, PMMA is the assumed material. The density is obtained by measuring the volume and weight for a 3D printed cube of VeroClear<sup>TM</sup>, but the dimensions of the cube are slightly uneven resulting in a range of densities between 1.15 and 1.19 g/cm<sup>3</sup> and so a nom-

**Table 2. Summary of Geant4 parameters and settings used in the RSM radiation transport model.**

Parameter	Description
Model Geometry	Scintillator, multiple aluminum tubes, Spartan I Mask
Physics Package	- QGSP_BIC_HP (Neutrons) - FTFP_BERT_LIV (Gamma Rays)
Neutron Source	ISO 8529-1:2001 AmBe spectrum
Gamma-Ray Source	$^{137}\text{Cs}$ (0.661657 MeV) $^{60}\text{Co}$ (1.173228 MeV and 1.332492 MeV) $^{12}\text{C}^*$ (4.438 MeV) $^{22}\text{Na}$ (0.511 MeV and 1.274537 MeV)
Source Direction	Cone directed at the center of the detector
Source Distance	86.36 cm (first directional measurement) 106.46 cm (second directional measurement)
Number of Particles	4e7 to 1e9
Model Output	- Primary particle energy deposition in active detector volume - Secondary particle energy deposition in active detector volume

inal density of  $1.19 \text{ g/cm}^3$  is used [37]. Two different default physics packages are employed. For neutrons, the QGSP\_BIC\_HP physics list, which includes the Quark Gluon String model, Binary Cascade model, and the High Precision Neutron Model is used. For gamma rays, the physics list used is FTFP\_BERT\_LIV, which includes the Fritiof String model, Bertini-Style Cascade model, and the low energy electromag-

**Table 3. The materials and densities used for the Geant4 model.**

Material	Density [ $\frac{\text{g}}{\text{cm}^3}$ ]	Components
EJ-309	0.959	Detector active volume
Pseudo-PMT	0.39	PMT
Aluminum-6061	2.7	Detector casing, PMT casing, detector tube, rotating tube
PMMA	1.19	Mask
Borosilicate Glass	2.23	Scintillator Window
Air	0.00120479	Environment

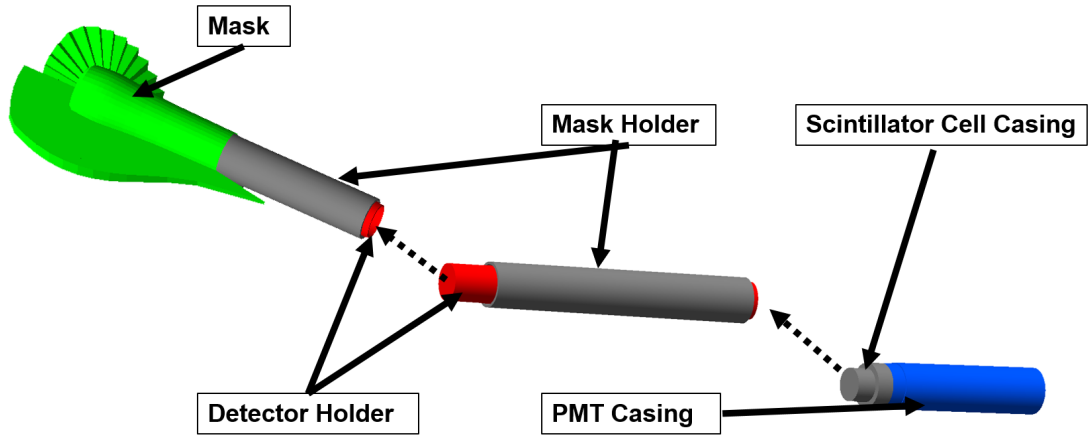


Figure 26. Geant4 geometry for the RSM showing all components except for the active detector volume, scintillator window, and PMT, which are all enclosed inside of the PMT and scintillator cell casing. The dashed arrows represent where each component is inserted.

netic Livermore Physics list. Both of these physics packages are recommended for radiation transport below 20 MeV for radiation protection and shielding studies [45]. Both the Binary and Bertini-Style Cascade models allow for tracking the secondary protons and electrons necessary to generate the detector response of an EJ-309 scintillator. The High Precision Neutron Model uses the Geant4 Neutron Data Library (G4NDL4.5), which consists primarily of nuclear data from Evaluated Nuclear Data Files (ENDF/B-VII.r1) with NJOY (NJOY-99u364) processing for resonance reconstruction [46].

Multiple simulations are performed using the radiation sources listed in Table 3 at source positions matching the experimental positions. To help calibrate and determine the detector resolution, a simulation is executed for each source without the mask and mask holder. This modification allowed for an energy spectra comparison with experimentally measured spectra to determine the appropriate light yield parameters,  $a$  and  $b$ , in Equation 10.

Full DRMs are generated at two different source distances using both an AmBe

neutron spectrum and the 4.438 MeV mono-energetic gamma ray from the de-excitation of  $^{12}\text{C}^*$ . These DRMs are used to generate the linear expression for determining the  $\phi$  direction of a source and for a direct comparison to experimentally measured DRCs. To reduce the number of particles required to obtain a converged solution, the particles are emitted as a biased cone source as shown in Figure 27. The cone half-angle,  $\theta_H$  in degrees, is determined based on the source-to-detector distance so the entire RSM is encapsulated by the cone. This is calculated using Equation 17, where  $W$  is the absolute maximum mask dimension and  $r$  is the source-to-detector distance.

$$\theta_H = \tan^{-1} \left( \frac{W + 2}{r} \right) \quad (17)$$

An additional two centimeters are added to  $W$  as a “safety factor”. Mathematically to account for this variance reduction technique in the simulation results a scaling factor is required, Equation 18.

$$VR = \frac{1 - \cos\left(\frac{\theta_H \tan 2(0,-1)}{180}\right)}{2} \quad (18)$$

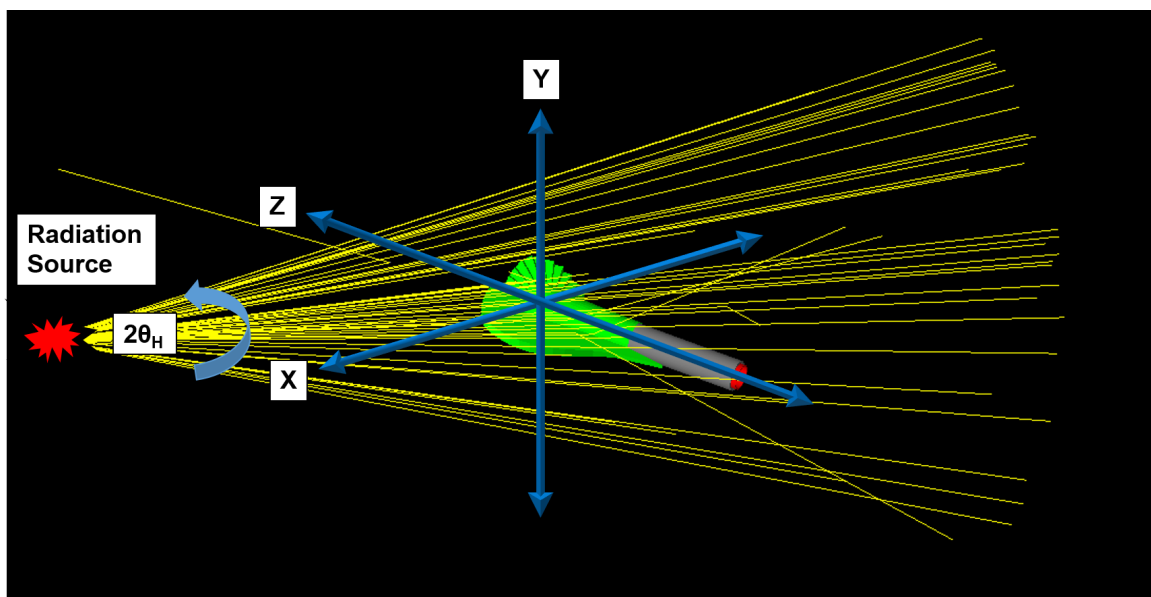


Figure 27. Example Geant4 simulation run for the RSM where the primary neutrons or gamma-ray particles represented by the yellow rays are emitted as a biased cone towards the RSM system to reduce computational time.

## 4. Results

The previous three chapters provided motivation, background information, and the methodology for the neutron RSM directional detection system proof-of-concept study. This chapter presents the results and is organized as follows. First, the applied detector acquisition settings and overall PSD performance are provided. Next, spectral analysis of the experimental and simulated neutron and gamma-ray events, including the detector calibration, determination of the detector resolution function, and the application of Birks' formula, are discussed. Finally, the directional identification performance of two measurement sets is analyzed, along with a characterization of the system's FOV and efficiency.

### 4.1 Pulse Shape Discrimination Performance

The primary detector acquisition settings used for all measurements are listed in Table 4. A full list of settings is found in Appendix A. The settings are determined through a simple iterative approach based on settings from previous work with the same DAQ as a starting point [44, 47–50].

**Table 4. Final radiation detection data acquisition settings used throughout the experiment. All settings are adjustable using the DPP-PSD software provided by CAEN [44].**

Settings	Input
High Voltage	-800 V
Record Length	672 ns
Threshold	250 LSB
Gate Offset	8 ns
Short Gate	60 ns
Long Gate	500 ns
Trigger Hold Off	544 ns
Charge Sensitivity	40 fc/LSB

For each detected waveform, the integrated charge of the short and long gates are

recorded and a PSD ratio is calculated using Equation 12. The results are grouped into 100 bins for viewing purposes to generate a 2D PSD histogram as shown in Figure 28. Two clear bands are seen representing the neutron and gamma-ray events. A curved discrimination cut, the red dashed line, is used to separate the clusters and calculate the total number of neutron and gamma-ray events for each measurement. The upward curvature, at higher integrated charge values, of each band arises from a non-linear amplification of the induced signal for higher energy photoelectrons generated by the PMT's photocathode. A bias of -800 V enabled strong particle discrimination performance, a manageable curvature of the bands, and ensured all events fell within the DAQ's 2 V peak-to-peak dynamic range.

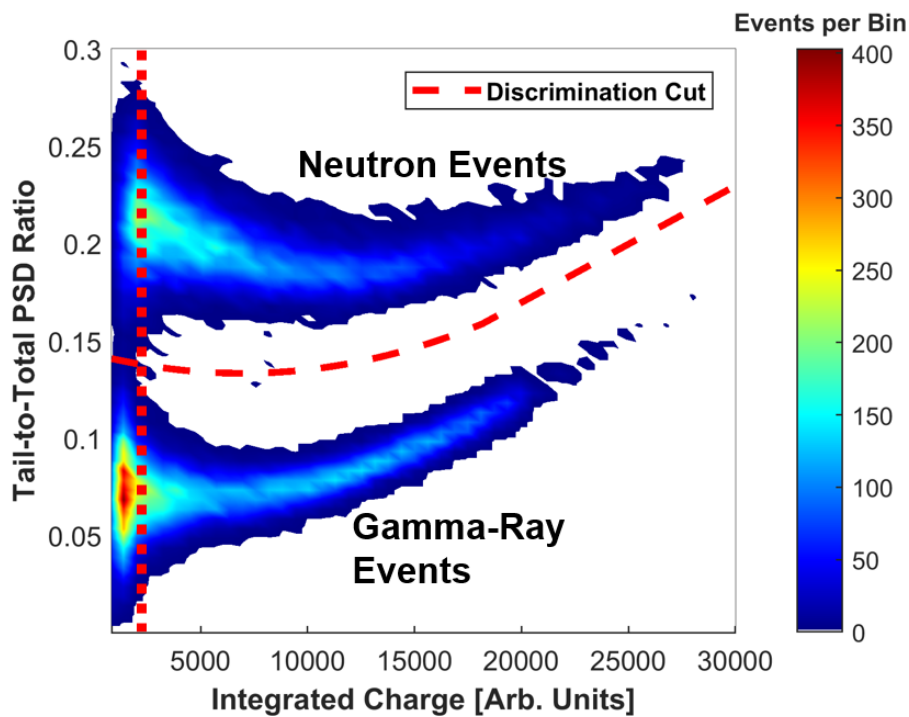


Figure 28. 2D PSD histogram generated using Equation 12 for measured waveforms of an AmBe source with a 1" EJ-309 liquid scintillator. The red lines represent discrimination cuts made to the particle clusters to separate between neutron and gamma-ray events resulting in an average FOM of 1.74.

The curved PSD discrimination cut is generated by taking 100 vertical slices of

the PSD plot. The  $y$ -projection of each slice creates a 1D PSD histogram, similar to Figure 20 in Section 2.6.5. The midpoints between each of the centroids from the double Gaussian fits are taken to be the PSD ratio cut for that slice. This method would not be ideal if one of the bands is significantly wider than the other but suffices for the current detection system. Finally, a linear interpolation between each of the 100 slices is used to generate a PSD ratio cut for every integrated charge bin. At lower bins there is an overlap between the two bands, resulting in the use of a conservative integrated charge cut at channel 2040, the vertical red dotted line in Figure 28.

The conservative cut avoids the issue of incorrectly classifying neutron and gamma-ray events at low integrated charge values. Additionally, this cut made the experimental validation of the primary aspects of the model more robust as the low energy depositions are likely to be populated by the surrounding environment, which is not modeled. However, this cut reduces the overall efficiency of the system and more robust PSD algorithms and cuts will be employed in future work.

Using the above methodology, a PSD FOM between 1.70 and 1.83 is obtained for all measurements performed throughout the experiment. This is as good, if not better, than the typical values reported in the literature for EJ-309 detectors [49, 51] and allows for excellent discrimination between neutron and gamma-ray events fundamental for generating separate particle dependent DRCs. Next, the detection system must be calibrated to obtain a common unit, keVee, relating the integrated charge, currently in channels, to the incident particle energy for comparison with the Geant4 simulations.

## 4.2 Energy Spectrum Analysis

### 4.2.1 Energy Calibration

The calibration technique employed uses the Compton edges of known gamma-ray energies and fits them to a partial Gaussian where the standard deviation,  $\sigma$  in units of channels, of the fit can then be used to determine the corresponding channel for the Compton edge energy with Equation 19 [49, 51].

$$N_c = N_e + 1.177\sigma \quad (19)$$

$N_e$  and  $N_c$  are the channel numbers of the centroid of the partial Gaussian fit and the Compton edge, respectively. Four different gamma-ray sources are used to perform the calibration, and the emitted gamma-ray and corresponding Compton edge energies are shown in Table 5. The Compton edge energies are calculated with Equation 5, where the Compton edge represents the maximum possible energy transfer a gamma ray can give to an electron, occurring at a scattering angle of  $180^\circ$ .

**Table 5. Gamma-ray sources used to calibrate a 1" EJ-309 liquid scintillator.**

Source	Gamma-Ray Energy [keV]	Compton Edge Energy [keV]
$^{137}\text{Cs}$	661.66	477.33
$^{60}\text{Co}$	1173.2	963.42
	1332.5	1118.1
$^{22}\text{Na}$	511	340.67
	1274.5	1061.7
$^{12}\text{C}^*$ (AmBe)	4438	4196.4

The partial Gaussian fits of this liquid scintillator calibration technique are shown in Figure 29, where the measured spectra are background-reduced before applying the edge fit. In each manually selected spectral region of interest, the partial Gaussian fit is represented by the dotted black or green lines, and the vertical lines represent the

location of the Compton Edges,  $N_c$ , used to generate the calibration curve. Noted previously, there is a non-linear behavior in the measured 2D PSD histograms at higher bins or gamma-ray energies. A third-order polynomial, Equation 20, is used to fit five calibration points shown in Figure 30.

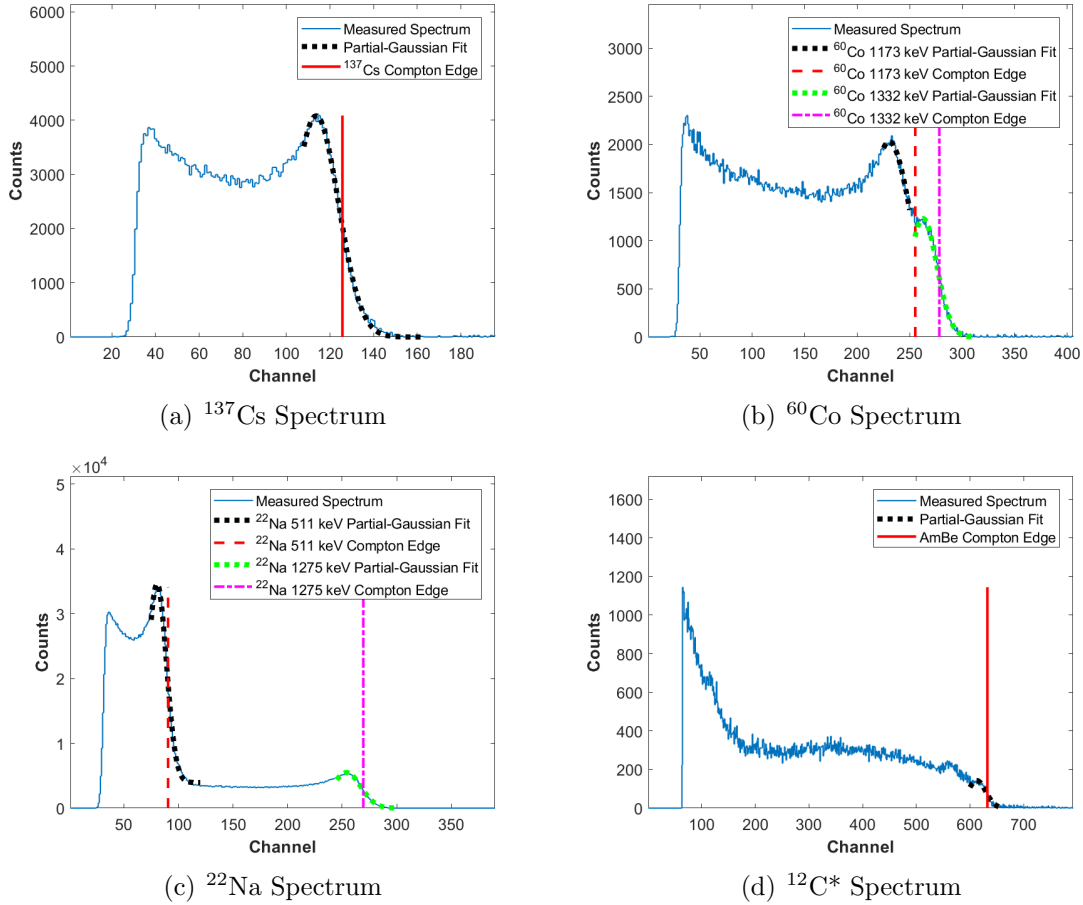


**Figure 29.** The results of a Compton edge calibration technique for a 1" EJ-309 liquid scintillator using  $^{137}\text{Cs}$ ,  $^{60}\text{Co}$ ,  $^{22}\text{Na}$ , and  $^{12}\text{C}^*$  gamma-ray sources [49, 51]. The experimentally measured pulse height spectra for each source are provided in (a), (b), (c), and (d) where the dotted black or green lines represent the partial Gaussian fits, and the vertical red or pink lines represent the location of the Compton Edge.

$$E [keVee] = (1.30 * 10^{-5})x^3 - 0.00434x^2 + 4.28x - 0.939 \quad (20)$$

For  $^{60}\text{Co}$  there is a slight overlap between the 1173.2 and 1332.5 keV gamma-ray

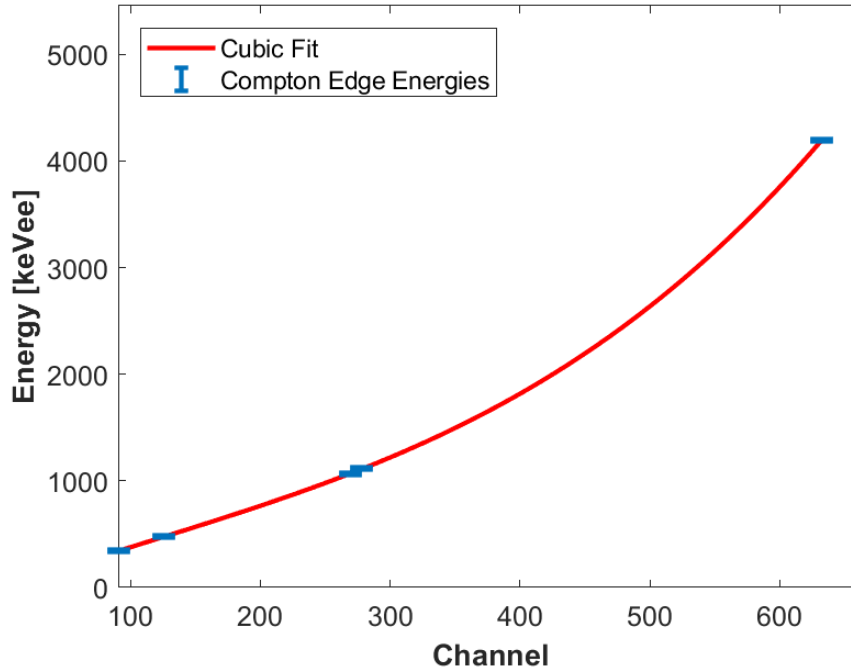


**Figure 30.** Measured energy calibration curve for an EJ-309 liquid scintillator using a Compton edge calibration technique with various gamma-ray sources. The data set is fit with a third-order polynomial to generate Equation 20.

Compton edges, causing both edges to be dependent on each other. The 1332.5 keV gamma-ray edge is at a higher energy and is affected to a lesser extent, because of this, only the 1332.5 keV edge is used and the 1173.5 keV edge is omitted from the calibration. Fortunately, the energy separation and difference in emission intensity of the  $^{22}\text{Na}$  gamma rays allows for both edges to be used in the calibration without any distortion. The statistical uncertainty used in the calibration curve data set is based on the one-sigma confidence interval of the partial Gaussian fit parameters  $\sigma$ , and  $N_e$ , extracted using the MATLAB Curve Fitting Toolbox [52].

The next step after calibrating the radiation detection system is a spectral comparison of simulated and experimental pulse-height energy spectra to determine the validity of using the simulated results for source direction identification, discussed in the next two sections.

### 4.2.2 Spectral Broadening

When a radiation-induced signal is processed through a real detection system, the signal becomes convoluted with physical limitations of the detection equipment, ultimately producing a perturbed output that is not accounted for in the Geant4 simulations. To account for this perturbation a broadening technique is employed assuming the response is represented by a Gaussian distribution. The broadened signal,  $g(x)$ , is calculated with Equation 21 [53], where each discrete channel,  $x$ , out of  $m$  total channels of a simulated spectrum is broadened. The resulting spectrum allows for a direct comparison with an experimental pulse-height energy spectrum.

$$g(x) = \sum_{x=1}^m g_i(x) \quad (21)$$

Summing each  $g_i(x)$  component generates the broadened signal,  $g(x)$ . The total number of counts,  $A_i$ , in the  $i^{th}$  discrete channel are distributed over all channels forming  $g_i(x)$  and represented by Equation 22. The channel being broadened is  $x_i$ , and the channel dependent detector resolution is represented by  $\sigma_i$ , the curve broadening term or channel standard deviation.

$$g_i(x) = A'_i e^{-\frac{(x-x_i)^2}{2\sigma_i^2}} \quad (22)$$

Some of the counts will be broadened outside of the channel range, 1 to 1024 channels. To account for these missing counts,  $A'_i$  is represented as  $A_i$  divided by a channel dependent normalization factor shown in Equation 23. The normalization component is the discrete area of the symmetric Gaussian distribution for  $m$  channels.

$$A'_i = \frac{A_i}{\sum_{x=1}^m e^{-\frac{(x-\frac{m}{2})^2}{2\sigma_i^2}}} \quad (23)$$

Note, as the number of channels goes to infinity, the normalization component approaches  $\sigma_i\sqrt{2\pi}$ . Currently, detection efficiency is being neglected for this study and is a potential source of error, but in future work will be incorporated by multiplying Equation 22 with a channel dependent efficiency factor.

The channel dependent detector resolution is obtained through a  $\chi^2$ -minimization algorithm of Equation 24 [8] summarized in Figure 31.  $\alpha$  and  $\beta$  are free parameters for fitting.

$$\sigma(x) = \frac{\sqrt{\alpha + \beta(x)}}{2\sqrt{2\ln 2}} \quad (24)$$

First, a Geant4 simulated histogram of the gamma-ray energy deposition is obtained for gamma rays emitted by a  $^{22}\text{Na}$  source incident inside of the EJ-309 active detector volume.  $^{22}\text{Na}$  is chosen for the optimization algorithm because of the wider gamma-ray emission energy range compared to  $^{137}\text{Cs}$  and  $^{60}\text{Co}$ . Then a pre-set range of 0 to 40 for  $\alpha$  and 0 to 10 for  $\beta$ , fit parameters of Equation 24, are selected to test a wide range of possible resolution functions. Using Equation 24, all possible permutations of  $\alpha$  and  $\beta$  are evaluated. Each broadened spectrum is normalized by dividing by the total number of counts and then compared to the normalized experimental spectrum through the  $\chi^2$  Goodness of Fit Test. Then a matrix of reduced  $\chi^2$  values for each  $\alpha$  and  $\beta$  pair is generated and the minimum value represents the best fit. The final parameters used in this study are  $\alpha = 0$  and  $\beta = 1.34$  leading to the resolution function shown in Figure 32.

The resulting normalized and broadened gamma-ray spectra for  $^{137}\text{Cs}$ ,  $^{60}\text{Co}$ , and  $^{22}\text{Na}$  compared against the experimental pulse-height spectra are shown in Figure 33. The experimental pulse-height spectra are obtained by generating a histogram of the total integrated charge,  $Q_{long}$ , of each event. Figures 33(b), 33(d), and 33(f) are the counting statistic one-sigma uncertainty bounds to visually show the level of

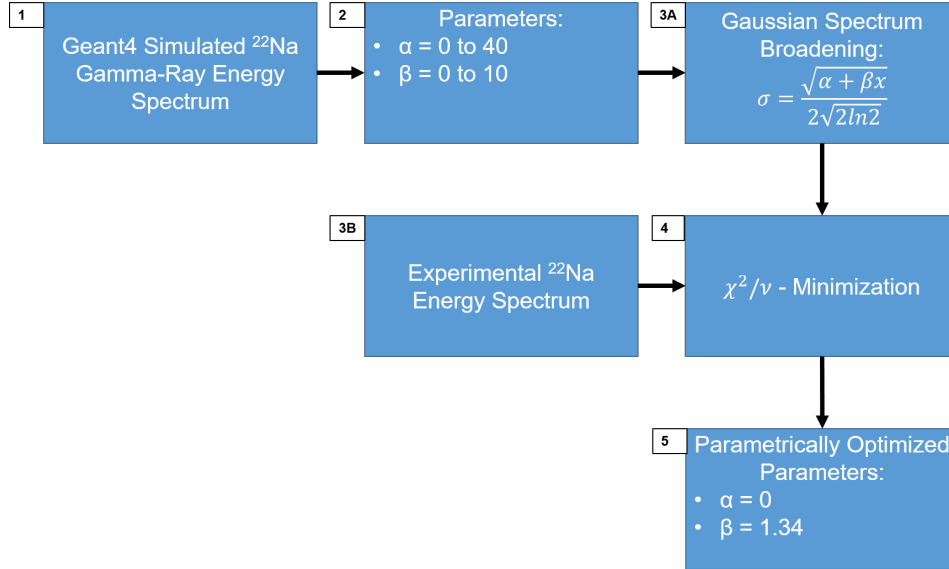


**Figure 31.** Schematic of the  $\chi^2$ -minimization algorithm used to obtain appropriate resolution parameters,  $\alpha$  and  $\beta$ , for Equation 24 to allow for energy dependent channel broadening of the Geant4 simulated spectra.

overlap between the measured and simulated spectra, and a summary of the spectral quantitative comparisons are provided in Table 6. The spectra are compared between energies of 130 keVee, set by the calibrated signal threshold of the DAQ listed in Table 4, up to the highest experimental energy bin with more than 100 events ( $< 10\%$  counting uncertainty).

**Table 6.** Summary of the level of agreement between background-subtracted measured and Geant4 simulated  $^{137}\text{Cs}$ ,  $^{60}\text{Co}$ , and  $^{22}\text{Na}$  pulse-height spectra for a 1" EJ-309 liquid scintillator. The experimental measurement count time is 12 hours and the simulation used 1,000,000,000 source particles.

Source	$\chi^2/\nu$	MAC	Average Relative Difference [%]	Maximum Relative Difference [%]
$^{137}\text{Cs}$	2.05	0.999	3.57	60.6
$^{60}\text{Co}$	2.92	0.997	4.68	43.6
$^{22}\text{Na}$	105	0.996	13.8	26.5

The Geant4 spectral broadening methodology obtained mixed results with an average channel-by-channel relative percent difference of 8.14%, and an overall maximum percent difference reaching 60.6%. The spectral shape showed excellent agreement

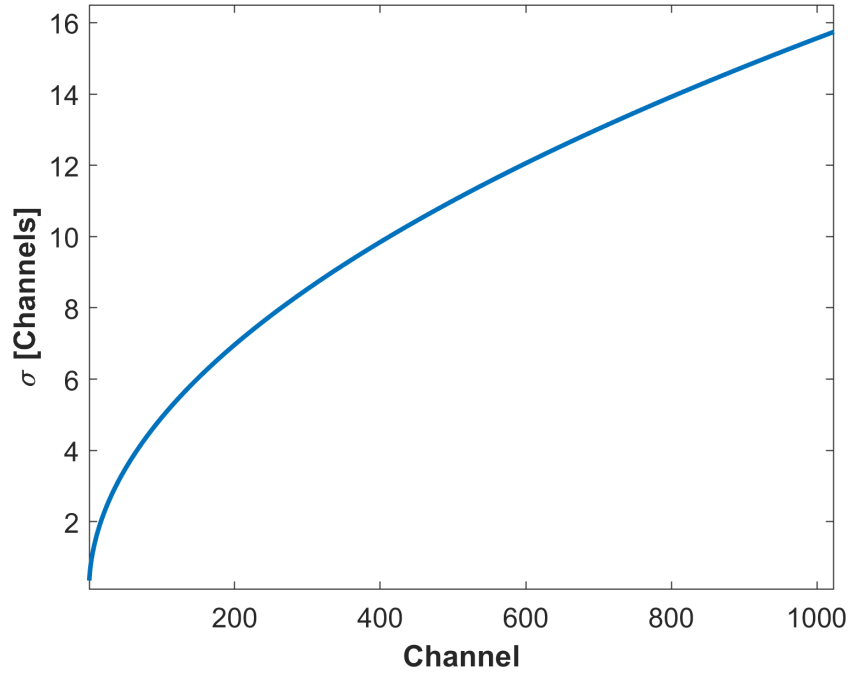
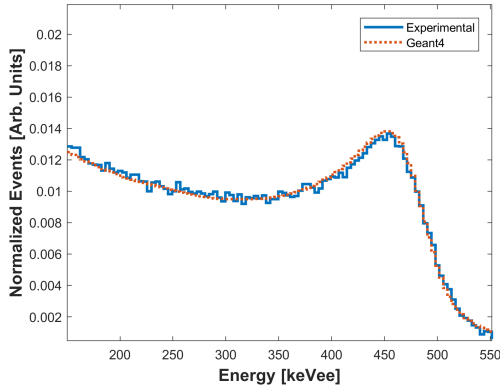
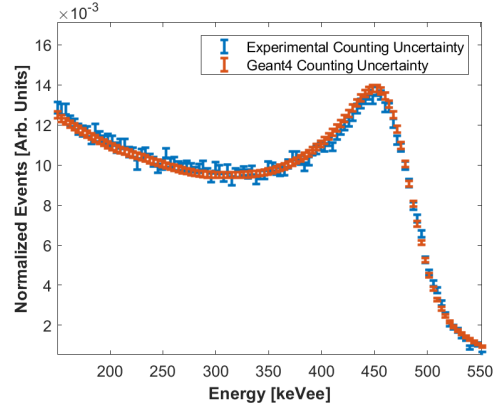


**Figure 32.** The detector resolution represented by the standard deviation of the channel dependent spread,  $\sigma$ , determined through a  $\chi^2$ -minimization algorithm of Equation 24 [8].

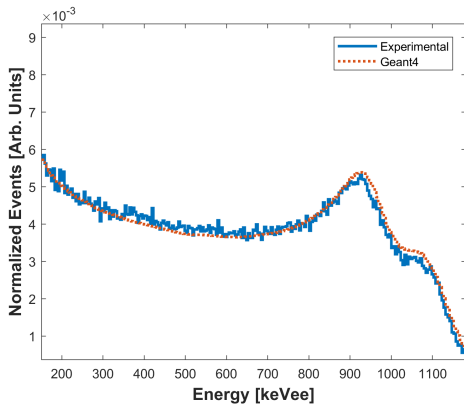
where all three spectral comparisons obtained MAC values greater than 0.99. The largest deviations for the  $^{137}\text{Cs}$  and  $^{60}\text{Co}$  spectra, on a relative difference basis, occurred at higher energy bins where the measured counts are very low with respect to the rest of the spectra and had poorer counting statistics. As for the  $^{22}\text{Na}$  spectra, visually the level of agreement looks worse and the average relative difference is much higher; however, the maximum relative difference is lower compared to the results for  $^{137}\text{Cs}$  and  $^{60}\text{Co}$ . These spectral deviations could potentially be caused by a combination of factors such as imperfections in the simulation physics and geometry simplifications made, the neglecting of experimental efficiency losses, imperfect experimental measurements, incorrect representation of the non-linearity in the calibration curve at higher gamma-ray energies, or due to error in the Compton edge calibration technique employed. The simulated gamma-ray spectra are generated by



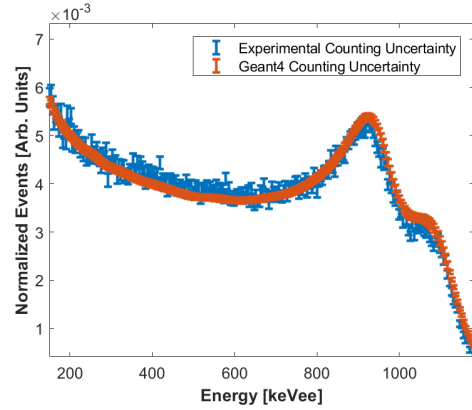
(a)  $^{137}\text{Cs}$  Spectra



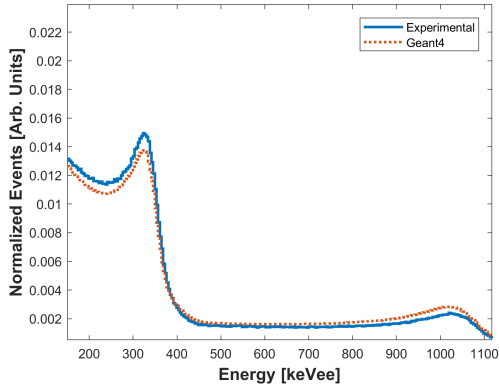
(b)  $^{137}\text{Cs}$  Spectra Counting Uncertainty



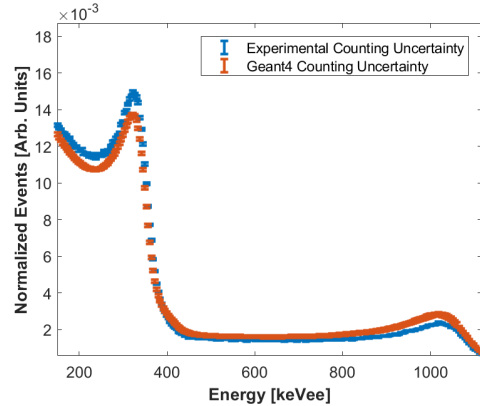
(c)  $^{60}\text{Co}$  Spectra



(d)  $^{60}\text{Co}$  Spectra Counting Uncertainty



(e)  $^{22}\text{Na}$  Spectra



(f)  $^{22}\text{Na}$  Spectra Counting Uncertainty

Figure 33. Visual comparison of normalized experimentally measured and broadened Geant4 simulated pulse-height energy spectra for  $^{137}\text{Cs}$ ,  $^{60}\text{Co}$ , and  $^{22}\text{Na}$  gamma-ray sources using a  $1''$  EJ-309 scintillator. The energy spectra are displayed in (a), (c), and (e), and the counting uncertainty for each energy bin is provided in (b), (d), and (f).

extracting the gamma-ray energy deposition histogram from the Geant4 results, an alternative approach to test in the future is to use electron energy deposition induced from gamma-ray interactions to potentially capture edge effects where induced electrons might not fully deposit all of the energy into the scintillator.

Even though the results did not obtain reduced  $\chi^2$  values of 1, the high MAC values for each comparison exemplify the ability to produce simulated spectra with similar spectral shapes to measured data. The next section discusses the same spectral broadening technique for the neutron and gamma-ray emissions of an AmBe source. For neutrons, Birks' formula is incorporated to account for non-linear proton light yield and allow quantification of how well the model can simulate the neutron detector response of an EJ-309 scintillator.

### 4.2.3 AmBe Spectrum Results

Section 4.1 demonstrated the RSM detection system coupled with an EJ-309 scintillator obtains excellent  $n/\gamma$  discrimination. This characteristic allows for the neutron and gamma-ray emissions of an AmBe source to be separated into two different pulse-height energy spectra for comparison with simulated results. Using the energy calibration curve, Equation 20, the lower-energy experimental pulse-height cut of 2040 channels, determined in Section 4.1, is converted to an electron equivalent energy of 258 keVee. This same energy cut is applied to the simulated results. Next, following the same procedure in the previous section, the simulated 4.438 MeV gamma-ray energy deposition spectrum is normalized and broadened to compare with measured results. However, for the neutron simulation, the simulated recoil proton energy deposition spectrum first needs to be converted to an equivalent electron light yield using Birks' formula before broadening.

Parameters  $a$  and  $b$  for Birks' formula, Equation 10, are obtained through a  $\chi^2$ -

minimization algorithm summarized in Figure 34 and very similar to the algorithm used in the previous section. A Geant4 simulated histogram of the recoil proton energy deposition is generated for neutrons emitted by an AmBe source. Then to avoid obtaining unrealistic results, a range for the fit parameters are selected based on values found in literature [36],  $a$  and  $b$  varied from 1 to 10 and 10 to 45, respectively. For each  $a$  and  $b$  combination using a step size of 100, the resulting light yield converted energy histogram is broadened and compared to the experimental neutron pulse-height spectrum using Equation 15 divided by the total number of degrees of freedom,  $\nu = 790$ . The smallest reduced  $\chi^2$  value corresponds to the best fit parameters and are found to be  $a = 5.22$  and  $b = 44.29$ . As expected based on the discussion from Section 2.6.5, these parameters result in a non-linear electron equivalent proton light yield,  $L(E_p)$ , as a function of recoil proton energy, shown in Figure 35.

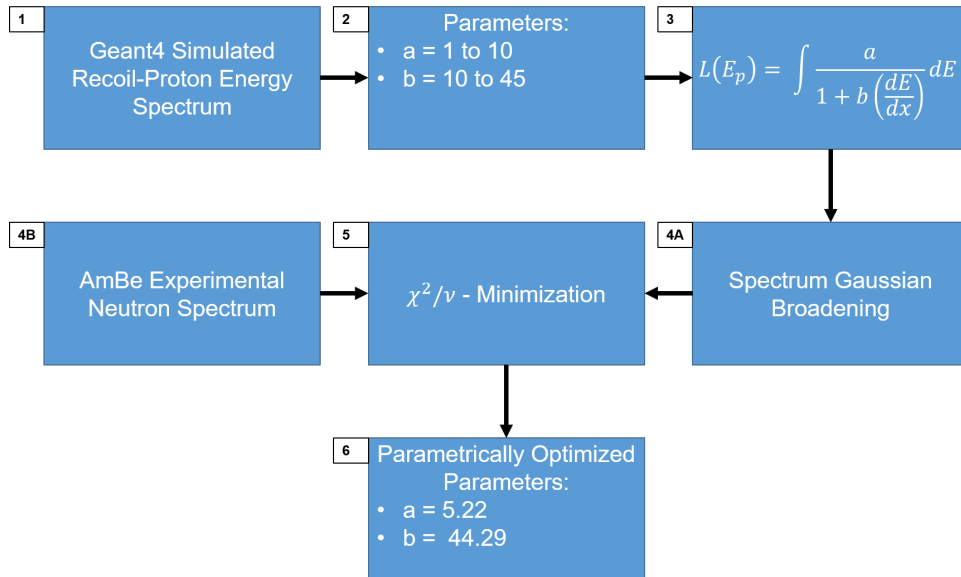


**Figure 34. Schematic of the  $\chi^2$ -minimization algorithm used to obtain appropriate parameters,  $a$  and  $b$ , for Birks' formula to convert recoil-proton energy to an equivalent electron light yield energy.**

The measured and Geant4 simulated AmBe pulse-height energy spectra, using a 1" EJ-309 scintillator, for gamma-rays and neutrons are shown in Figures 36 and 37, respectively. A summary of the comparison metrics is provided in Table 7 to quan-

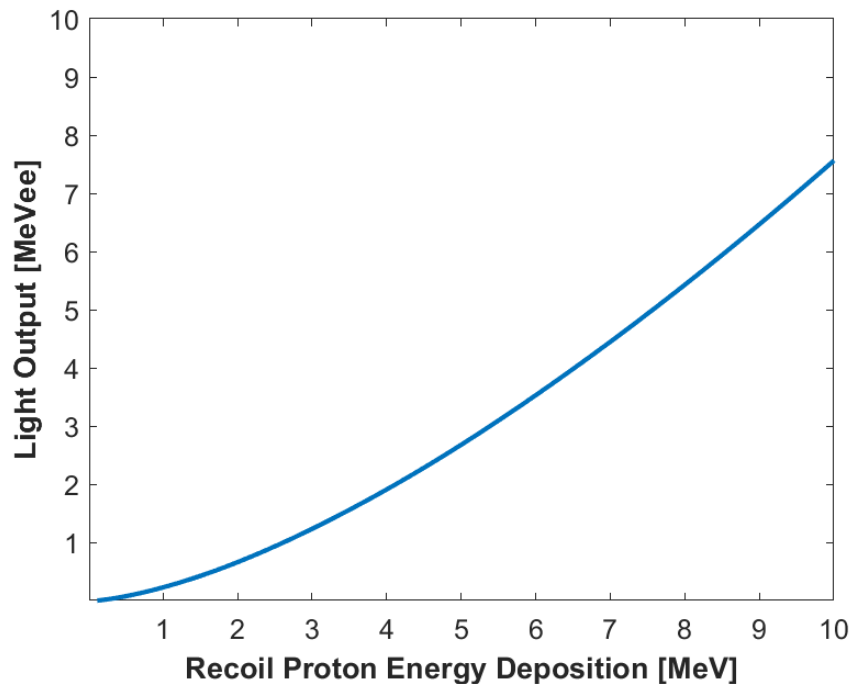


**Figure 35.** The estimated proton light yield for a 1'' EJ-309 liquid scintillator using Birks' formula. The parameters,  $a = 5.22$  and  $b = 44.29$ , of Equation 10 are found by  $\chi^2$  minimization.

tify the level of spectral agreement. Looking at the 4.438 MeV gamma-ray spectra comparison first, covering energies from 258 to 4300 keVee, there is a higher level of disagreement in spectral shape compared to the gamma-ray results from the previous section. Specifically, the MAC value is only 0.739 while the previous three comparisons are greater than 0.99. The reasoning for such dramatic discrepancies in shape remains an open question, but possible causes are poor counting statistics in the measured data, incorrect calibration representation of the non-linear behavior at high energies, the neglecting of the energy-dependent detection efficiency in the simulated spectrum, or the most probable cause, experimental backscattering effects not accounted for in the model. Figure 11 in Section 2.3.1 showed the mean-free path of 4.438 MeV gamma-rays through an EJ-309 scintillator is over 30 cm. Thus, the measured spectrum has a large counting uncertainty since the majority of gamma-rays

are not interacting inside of the active detector volume. In addition, perhaps a large contribution of the detected events at lower energies, where the model and experiment deviate the most, are from Compton scattering events outside of the detector and edge effects.

For the simulated neutron pulse-height energy spectrum, shown in Figure 37, a higher level of agreement is observed over the energy range from 258 to 8500 keVee, where the average relative percent difference is 12.0% with a reduced  $\chi^2$  and MAC value of 2.06 and 0.997, respectively. The reduced  $\chi^2$  shows the statistical level of agreement exceeds that of all gamma-ray spectra comparisons. Further efforts must still be made to correctly model the neutron detector pulse-height response by possibly using alternate physics packages, a different proton light yield conversion method, or through the inclusion of other charged particles such as alpha and carbon nuclei since the contributions are currently assumed to be negligible.

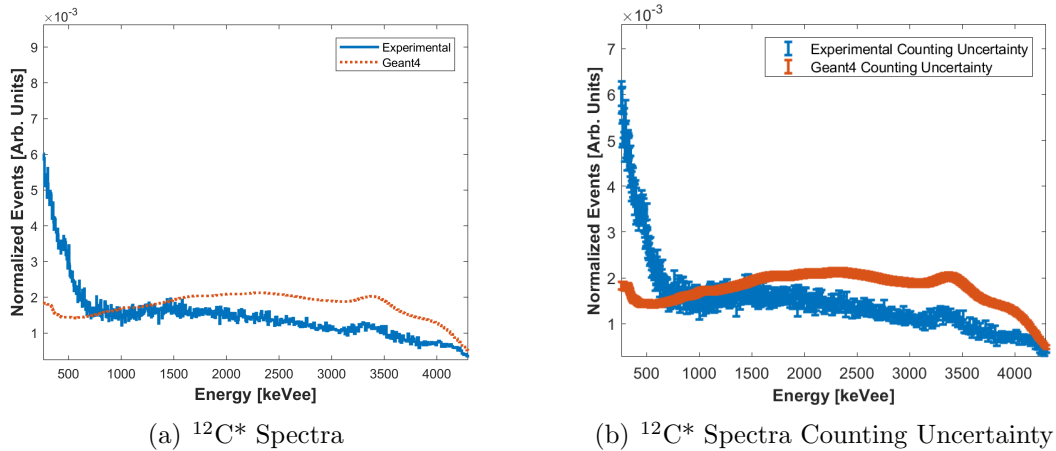


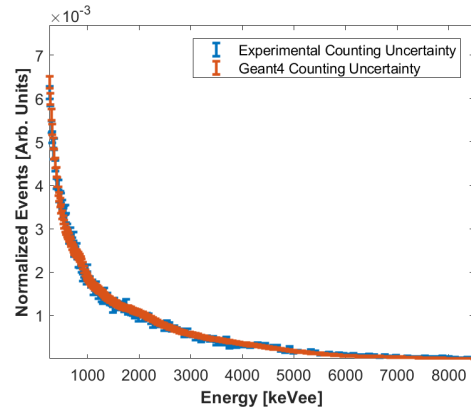
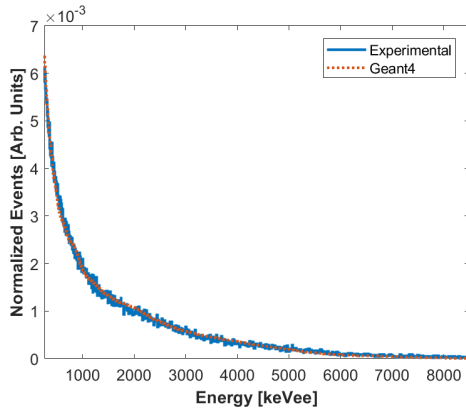
**Figure 36.** Visual comparison of normalized experimentally measured and broadened Geant4 simulated  $^{12}\text{C}^*$  de-excitation energy spectra from an AmBe source for the detector response of a 1" EJ-309 scintillator. The energy spectra are displayed in (a), and the counting uncertainty for each energy bin is provided in (b).

The first half of this chapter demonstrated the ability to experimentally separate neutron and gamma-ray emissions of an AmBe source to generate pulse-height energy

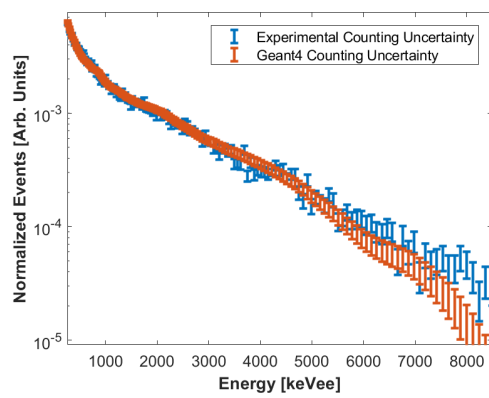
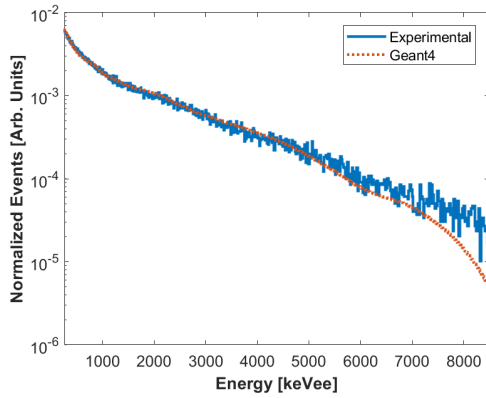
**Table 7. Summary of comparison between background-subtracted measured and Geant4 simulated AmBe pulse-height energy spectra over the energy range of 258 to 4438 keVee for gamma-rays and 258 to 8500 keVee for neutrons with a 1" EJ-309 liquid scintillator.**

<b>Particle</b>	$\chi^2/\nu$	<b>MAC</b>	<b>Average Relative Difference [%]</b>	<b>Maximum Relative Difference [%]</b>
Neutrons	2.06	0.997	12.0	81.9
Gamma Rays	45.0	0.739	40.6	145

spectra, perform an energy calibration, and to quantify how well the Geant4 model can generate a realistic detector response. These capabilities demonstrate the RSM system's credibility to assist in detecting radioactive materials such as SNM being illicitly trafficked. Additionally, by performing a particle dependent spectral analysis the radiation source can further be characterized. For example, if the neutron source was unknown in this experiment, one would still be able to predict the type of neutron producing reaction based on identifying the gamma-ray Compton Edge around 4.1964 MeV. A Compton edge around this energy infers that the source is emitting 4.438 MeV gamma-rays, consistent with the  $^{12}\text{C}^*$  de-excitation emission after  $^{13}\text{C}$  emits a neutron. This means the neutron source must be composed of  $^9\text{Be}$  and an unknown  $\alpha$  particle emitting radioisotope, such as  $^{241}\text{Am}$ ,  $^{238}\text{Pu}$ ,  $^{210}\text{Po}$ , or  $^{226}\text{Ra}$ . Neutron spectroscopy will be investigated in future work to characterize neutron sources even further. Next, the energy calibration and proton light yield expressions are used to synchronize the experimental and Geant4 simulated energy deposition cuts to generate DRCs for source direction identification.



(a) AmBe Neutron Energy Spectra (Linear Scale) (b) AmBe Neutron Energy Spectra Counting Uncertainty (Linear Scale)



(c) AmBe Neutron Energy Spectra (Log Scale) (d) AmBe Neutron Energy Spectra Counting Uncertainty (Log Scale)

**Figure 37.** Visual comparison of normalized experimentally measured and broadened Geant4 simulated AmBe neutron energy spectra for the detector response of a 1" EJ-309 scintillator. The energy spectra in linear and log scale are displayed in (a) and (c), respectively, and the counting uncertainty for each energy bin is provided in both linear and log scale in (b) and (d), respectively.

### 4.3 Directional Measurements

The spectral analysis portion of this study showed mixed results, and enhancements to the model remains ongoing work with the goal of reaching an average relative difference of less than 1%. Fortunately, the modeled and experimental spectra showed consistent similarities in shape still allowing for direction identification of both neutrons and gamma rays. The subsequent sections provide a summary of the RSM system's directional detection performance, both computationally and experimentally.

#### 4.3.1 Direction Identification Performance

Using the final light conversion parameters obtained in the previous section, the energy deposition cut of 258 keVee is converted to a proton energy deposition equivalent value of 1084 keV. Then, a DRM is generated by summing the total number of neutron events per source position, where a neutron event in the model is defined as any secondary recoil proton energy deposition that exceeds 1084 keV.

For simulated gamma-ray DRCs, a 258 keV cut is used on deposition events because a light yield energy conversion is not required. Secondary particles, other than protons, are neglected for computational efficiency and because the equivalent light yield is even less than the light yield of recoil protons when generating the simulated DRCs; however, this could be a minor source of error due to the small size of the detector [54].

The angular distance between a DRC's wall and fin valleys are extracted from the simulated DRM, Figure 38. These values are calculated using the difference between the mean values of the Gaussian fits for each  $\phi$  mode DRC valley. For each Gaussian fit, 14 data points are used, and the propagated one-sigma uncertainty for the true mean of each fit is incorporated when calculating the angular separation between

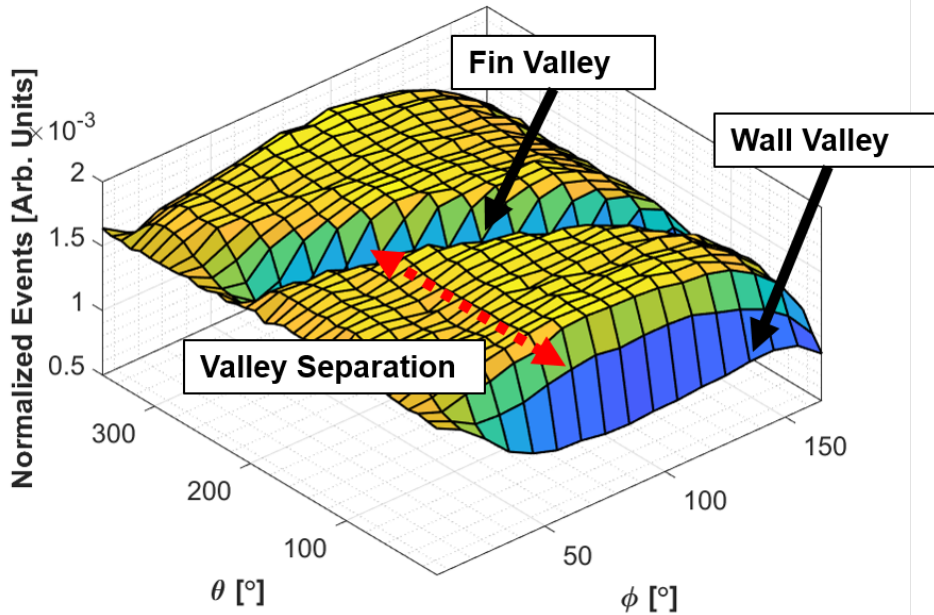


**Figure 38.** Geant4 simulated DRM for an AmBe source place 86.36 cm from the RSM. A proton energy deposition cut of 1084 keV is used, where only protons depositing energy greater than or equal to 1084 keV is considered a detected event.

the valleys. The linear correlation between the valley angular separation and the  $\phi$  direction is shown in Figure 39.

To determine a source's  $\theta$  direction the valley generated by the wall and fin must be distinguishable from each other and from the DRC's baseline. Here, the wall-valley represents the  $\theta$  direction. Through MCNP6.1.4 simulations, Olesen showed the wall valley is deeper than the fin valley between  $\phi$  directions of  $30^\circ$  to  $150^\circ$ , allowing for discrimination to be possible [12]. However, for this study, the wall-width is used instead, where the narrower valley represents the wall of the mask. The next section discusses why the valley widths are better DRC for valley discrimination than the valley depths. Also shown in Figure 39 is the geometrical expression based on the physical mask geometry, Equation 16, from Section 3.1. Comparing the two linear expressions, on average, there is at most a 1.3% difference for each  $\phi$  mode. This result confirms that the physical mask geometry and simulated detector response have

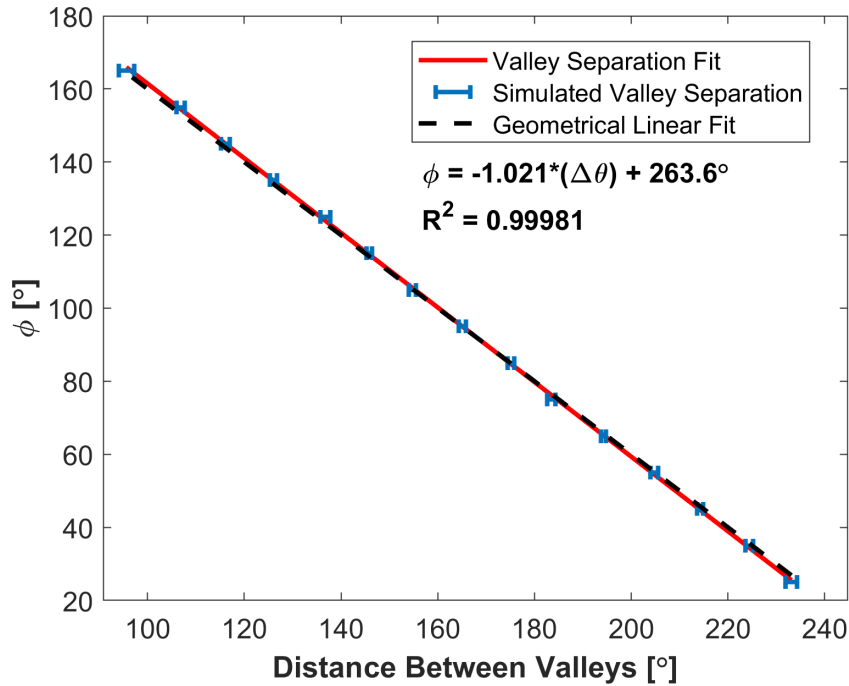


**Figure 39.** DRC angular valley separation curve generated from Figure 38 to determine the  $\phi$  direction of a source. Each valley is fitted with a Gaussian distribution to determine the location of the minima. The linear expression representing the geometry of the Spartan I mask generated from the design matrix is also plotted.

sufficient agreement, and the linear expression obtained using the Geant4 simulated DRM is valid for source direction identification. The direct relationship between the scatter mask's geometry and response curve exemplifies the ability to identify a source's direction using a simple linear expression rather than a complex image reconstruction algorithm.

Two sets of directional measurements at different distances and directions with an AmBe source are performed to validate the RSM system's capabilities. The results are summarized in Tables 8 and 9 for the neutron and gamma-ray emissions, respectively. The uncertainties in the actual direction capture the uncertainty in the precision of the measurement and potential error in the source placement. The experimental DRCs are generated by combining 36 stationary background-subtracted measurements obtained when rotating the mask  $10^\circ$  between each measurement. Overall, the system

correctly predicted the source direction within  $5^\circ$ , in both  $\theta$  and  $\phi$ , for neutron emissions and within  $10^\circ$  for gamma rays with a maximum uncertainty of  $4.63^\circ$ ; thereby meeting the  $10^\circ$  voxel geometrical design resolution of the Spartan I mask. The EJ-309 scintillator has a higher detection efficiency for lower energy gamma rays, such as the emissions from  $^{137}\text{Cs}$ ,  $^{60}\text{Co}$ , or  $^{22}\text{Na}$ , and thus would most likely have a more accurate source direction prediction than obtained using the AmBe source due to improved counting statistics. Uncertainty in the directional predictions is based on a systematic error from the way the mask is rotated and statistical error in determining the valley centroids in a DRC.

**Table 8. Direction identification results for neutrons emitted by an AmBe source with the RSM. The RSM system correctly determined the direction for each measurement within  $5^\circ$  of the actual source direction.**

Source Distance [cm]	Source Direction			
	Actual		Predicted	
	$\theta$ [ $^\circ$ ]	$\phi$ [ $^\circ$ ]	$\theta$ [ $^\circ$ ]	$\phi$ [ $^\circ$ ]
$86.36 \pm 2.20$	$85.0 \pm 1.32$	$45.0 \pm 1.49$	$80.1 \pm 2.11$	$45.5 \pm 3.07$
$106.46 \pm 1.93$	$35.0 \pm 0.960$	$95.0 \pm 1.05$	$37.2 \pm 2.10$	$99.8 \pm 3.10$

**Table 9. Direction identification results for gamma rays emitted by an AmBe source with the RSM. The RSM system correctly determined the direction for each measurement within  $10^\circ$  of the actual source direction.**

Source Distance [cm]	Source Direction			
	Actual		Predicted	
	$\theta$ [ $^\circ$ ]	$\phi$ [ $^\circ$ ]	$\theta$ [ $^\circ$ ]	$\phi$ [ $^\circ$ ]
$86.36 \pm 2.20$	$85.0 \pm 1.32$	$45.0 \pm 1.49$	$85.0 \pm 3.13$	$49.1 \pm 4.36$
$106.46 \pm 1.93$	$35.0 \pm 0.960$	$95.0 \pm 1.05$	$39.3 \pm 2.90$	$105 \pm 4.63$

The neutron and gamma-ray DRCs for the first directional measurement set are displayed in Figures 40 and 41, where the AmBe source is placed 86.36 cm away from the center of the detector at a direction of  $\theta = 85^\circ$  and  $\phi = 45^\circ$ . The comparison metrics for the first measurement are provided in Table 10. Visually, the baseline of response curves match up very well, but the most noticeable discrepancy is an

apparent shift of up to  $5^\circ$  in the valley locations of the experimental DRCs compared to the simulated curves. This shift is evident in both the neutron and gamma-ray DRCs for the first measurement, but not the second, as shown Figures 42 and 43, making the most probable cause of this discrepancy experimental error when rotating the mask. During this experiment, a stepper motor is used to rotate the mask, and a fluctuation of up to  $2^\circ$  for each  $10^\circ$  rotation is observed. This experimental error is incorporated as horizontal error bars for all DRC plots; for future measurements, an encoder ring will be programmed to ensure accuracy in the mask rotational angle to mitigate this systematic error.

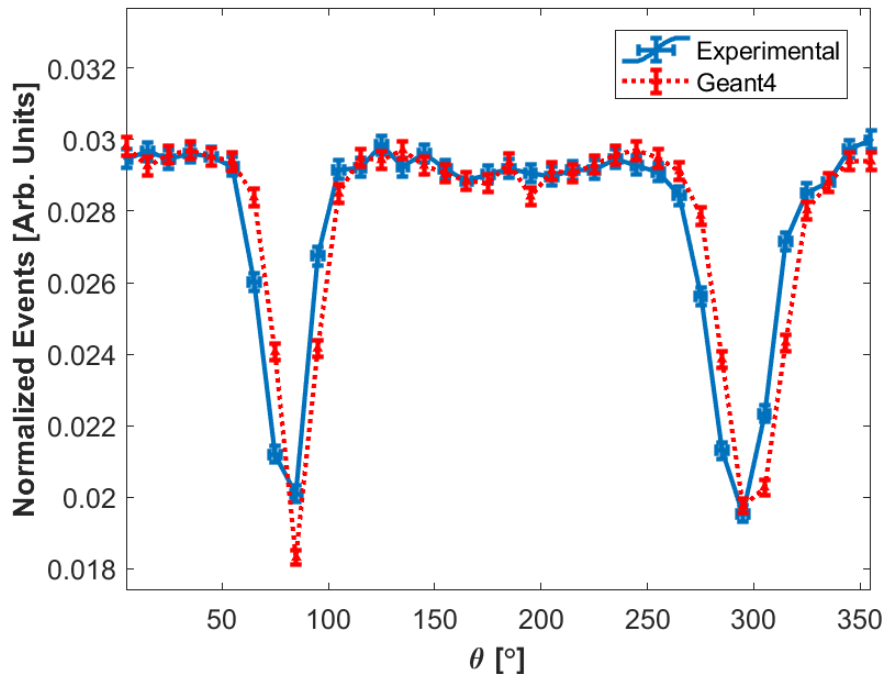


**Figure 40.** Comparison of normalized Geant4 and experimental neutron DRCs for an AmBe source placed 86.36 cm away from the center of the detector at a direction of  $\theta = 85^\circ$  and  $\phi = 45^\circ$ . The Geant4 model ran 40,000,000 source particles, and the experimental measurements are performed for 30 minutes in  $10^\circ$ -increments and are background subtracted.

In addition, the depth of the experimental neutron wall valley is much shallower. This could be a result of the rotational error previously mentioned, error in the

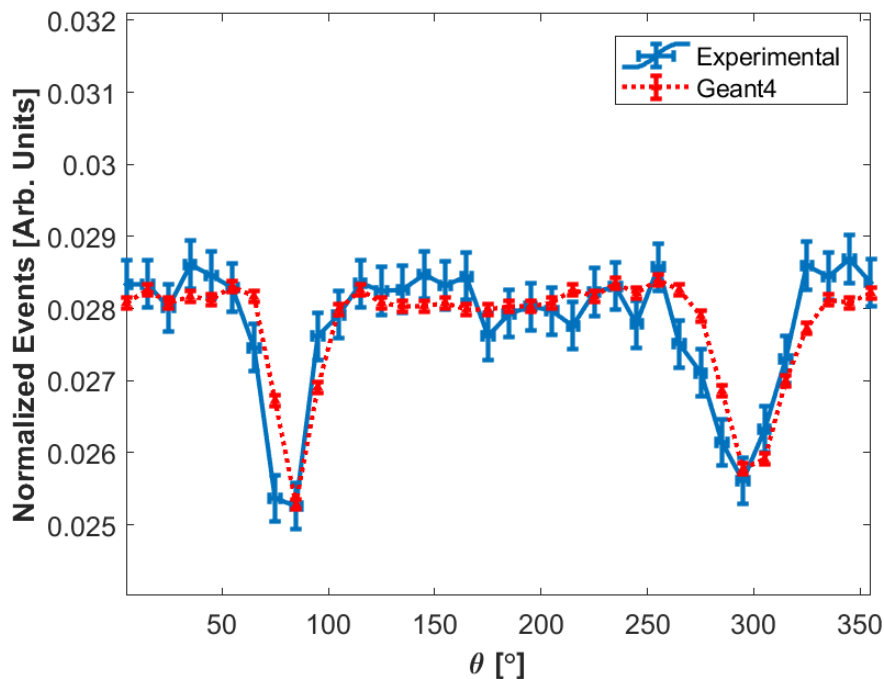


Figure 41. Comparison of normalized Geant4 and experimental gamma-ray DRCs for an AmBe source placed 86.36 cm away from the center of the detector at a direction of  $\theta = 85^\circ$  and  $\phi = 45^\circ$ . The Geant4 model ran 40,000,000 source particles, and the experimental measurements are performed for 30 minutes in  $10^\circ$ -increments and are background subtracted.

calibration and proton light yield conversion which would affect the energy cut used, backscattering effects not accounted for in the model, or could be related to the actual mask material being slightly different than PMMA. Even with the valley depth discrepancies and angular shift, the average relative difference for all rotational angles of the first measurement set is only 2.15%, with a maximum relative difference of 13.4% for both DRC comparisons. Lastly, the large fluctuations and uncertainty in the gamma-ray DRCs are due to the low efficiency of the 1" EJ-309 detector for 4.438 MeV gamma-ray emissions. Nonetheless, the source direction is still determined within  $10^\circ$ , demonstrating directional detection in a mixed-radiation environment with the RSM system.

For the second directional measurement set, the AmBe source is placed 106.46

**Table 10. Summary of comparison metrics for experimental and simulated DRCs for an AmBe source placed 86.36 cm away from the center of the detector at a direction of  $\theta = 85^\circ$  and  $\phi = 45^\circ$ . The Geant4 model ran 40 million source particles, and the experimental measurements are performed for 30 minutes in  $10^\circ$ -increments.**

Particle	$\chi^2/\nu$	MAC	Average Relative Difference [%]	Maximum Relative Difference [%]
Neutrons	25.9	0.845	3.04	13.5
Gamma-rays	2.08	0.745	1.27	5.39

cm away from the center of the detector at a direction of  $\theta = 35^\circ$  and  $\phi = 95^\circ$ . The measured and simulated DRCs for both neutrons and gamma rays are provided in Figures 42 and 43, respectively, where again, a strong agreement is obtained between measured and experimental DRCs. For this measurement, an electronic leveler is used after each rotation to mitigate the potential for mask rotational shifts. Thus, there is an improvement in the MAC values. In all DRCs, there is clear evidence the valleys induced by the wall and fin are sensitive to small rotational shifts in the mask. This sensitivity occurs because the wall and fin of the Spartan I mask are step changes in mask thickness, and so a small angular mask shift can have a drastic effect on the measured DRC; these are the regions where the relative differences are the highest between simulated and measured data.

**Table 11. Summary of comparison metrics for experimental and DRCs for an AmBe source placed 106.46 cm away from the center of the detector at a direction of  $\theta = 35^\circ$  and  $\phi = 95^\circ$ . The Geant4 model ran 40 million source particles, and the experimental measurements are performed for 30 minutes in  $10^\circ$ -increments.**

Particle	$\chi^2/\nu$	MAC	Average Relative Difference [%]	Maximum Relative Difference [%]
Neutrons	6.36	0.944	2.05	10.1
Gamma Rays	1.23	0.788	1.17	5.47

### 4.3.2 Modal Assurance Criterion Direction Identification Method

In previous experimental work with the original gamma-ray RSM system coupled with the FitzGerald mask design, Logan and Condon used a MAC comparison with

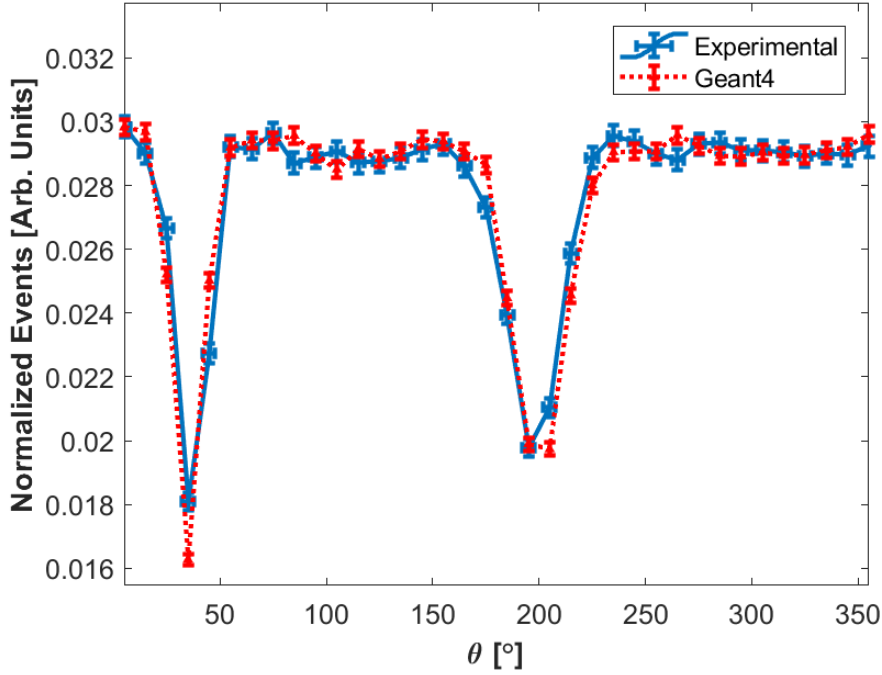


Figure 42. Comparison of normalized Geant4 and experimental neutron DRCs for an AmBe source placed 106.46 cm away from the center of the detector at a direction of  $\theta = 35^\circ$  and  $\phi = 95^\circ$ . The Geant4 model ran 40,000,000 source particles, and the experimental measurements are performed for 30 minutes in  $10^\circ$ -increments and are background subtracted.

measured and simulated DRCs to determine the source direction [11, 14]. The same method is demonstrated with the second neutron directional measurement set using the neutron system coupled with the Spartan I mask, Figure 44(a), showing a matrix with all of the MAC comparison values for each possible source direction. The algorithm correctly predicted the source direction of  $\theta = 35^\circ$  and  $\phi = 95^\circ$ ; however, a degenerate source direction is visible around  $\theta = 55^\circ$  and  $\phi = 195^\circ$ . This is due to a design flaw in the mask, where every wall-to-fin angular separation for one  $\phi$  mode has a complimentary  $\phi$  mode where the fin-to-wall (reversed) angular separation is the same. In other words, the degenerate location is the point where the measured DRC is being compared to a simulated DRC that has the wall and valley flipped, and thus the similar modal shape is causing a higher MAC value. The ability to distinguish

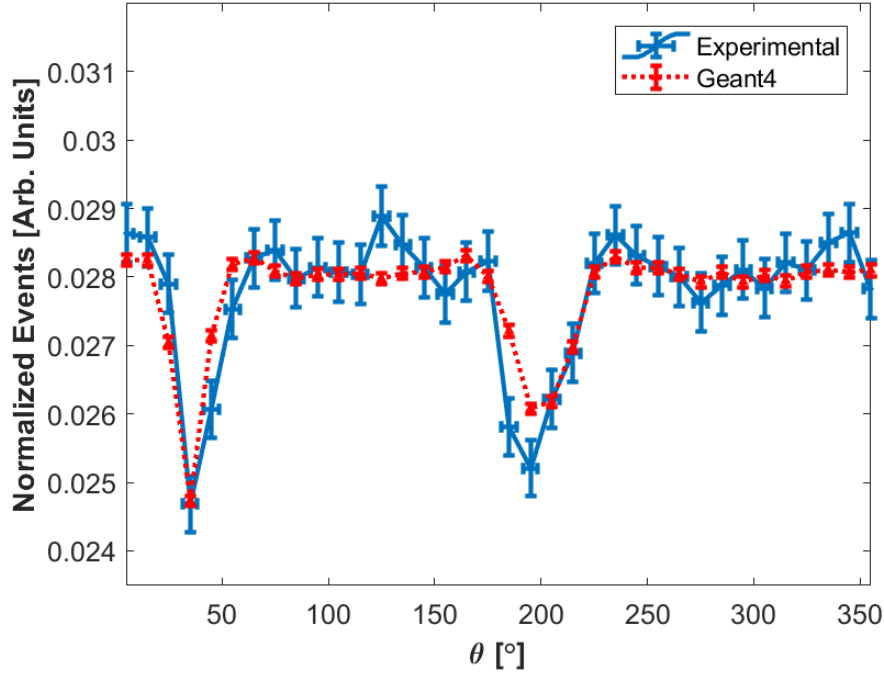
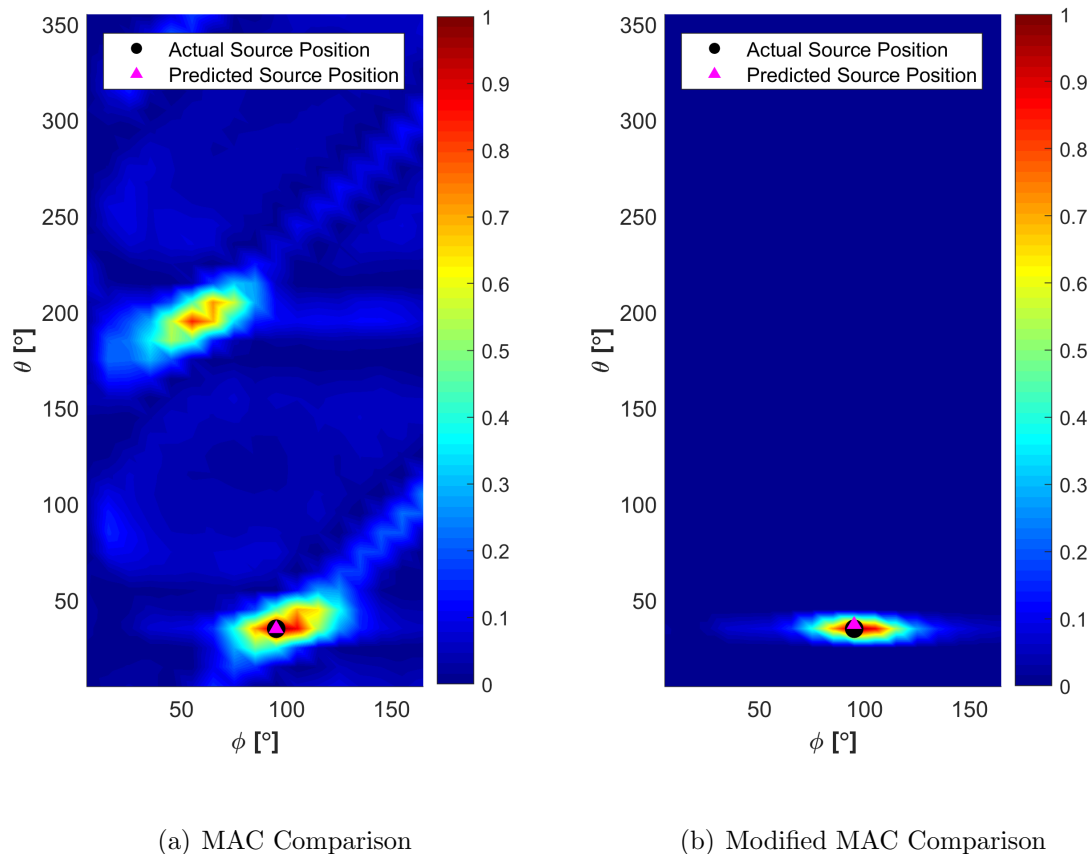


Figure 43. Comparison of normalized Geant4 and experimental gamma-ray DRCs for an AmBe source placed 106.46 cm away from the center of the detector at a direction of  $\theta = 35^\circ$  and  $\phi = 95^\circ$ . The Geant4 model ran 40,000,000 source particles, and the experimental measurements are performed for 30 minutes in  $10^\circ$ -increments and are background subtracted.

the wall from the fin valley based on the widths breaks this degeneracy. Assuming once the wall valley has been determined and the  $\theta$  direction is known, only MAC comparisons for specific  $\theta$  shifts are needed, and all of the other source directions are omitted by setting the MAC values to zero. This leads to a modified MAC comparison, where the comparison matrix results in only one possible source direction with much higher confidence than the original comparison, provided in Figure 44(b). Note that the resolution of the simulated DRM used to perform the MAC comparison with the measured DRC had a resolution of only  $10^\circ$ , and thus it would be misleading to assume the MAC comparison method is a better direction identification method compared to the Spartan method. A higher angular resolution MAC comparison would need to be performed to determine which method is more accurate.

The last two sections provide preliminary insight on the system FOV with the Spartan I mask and also the relative efficiency loss caused by using the scatter mask to transform an ordinary radiation detector into a directionally sensitive detector.



**Figure 44.** MAC matrices generated by a comparison between the measured neutron DRC and all shifted DRCs of the Geant4 simulated DRM for an AmBe source placed at a direction of  $\theta = 35^\circ$  and  $\phi = 95^\circ$ . The full MAC matrix is shown in (a), where the correct source direction is predicted, but a degenerate direction can still be seen. The modified MAC comparison is shown in (b), where the  $\theta$  direction of the source is determined based on the narrower valley of the measured DRC. This reduces the number of MAC comparisons required thus increasing confidence in the predicted source direction.

### 4.3.3 Rotating Scatter Mask Field-of-View

The newly developed RSM system coupled with the Spartan I scatter mask relies on the distinguishable and identifiable wall and fin valleys in the DRC to identify the source direction. This requirement limits the FOV of the Spartan I mask, which is graphically shown in Figure 45. The Geant4 simulated and experimentally measured fin-to-wall width ratios from this study, along with wall-to-fin depth ratio used in previous studies, are plotted as a function of the  $\phi$  angle between  $5^\circ$  and  $165^\circ$ . Ratios less than 1 signify the inability to identify between the wall and fin induced valleys without prior knowledge of the source direction and thus are out of the directional detection FOV, represented by the dashed red line. The error bars shown represent only the error propagated from the one-sigma confidence intervals for the Gaussian fitted parameters obtained from the wall and fin valley fits. Figure 45 indicates that using the valley width ratio rather than the depth ratio improves the overall FOV by over  $30^\circ$ . However, the uncertainty is still very large and needs to be reduced by shortening the mask rotational step size, currently  $10^\circ$ , to obtain more data points for each valley enhancing the Gaussian fit and reducing the overall uncertainty in the fitted parameters. With the current mask, any measurements where the source is outside of this FOV would result in the miss-identification of the source direction; alternative mask designs and classes being explored to solve this limitation [13].

### 4.3.4 Relative Efficiency Characterization

The drawbacks of many commercial directional detection systems is a significant loss in detection efficiency, while the neutron RSM results showed a relative efficiency loss of less than 10.4% between the two sets of directional measurements. Figure 46 shows the simulated normalized event rate for each DRC  $\phi$  mode, which is the average number of neutron events per source particle divided by the sum of the DRC. This

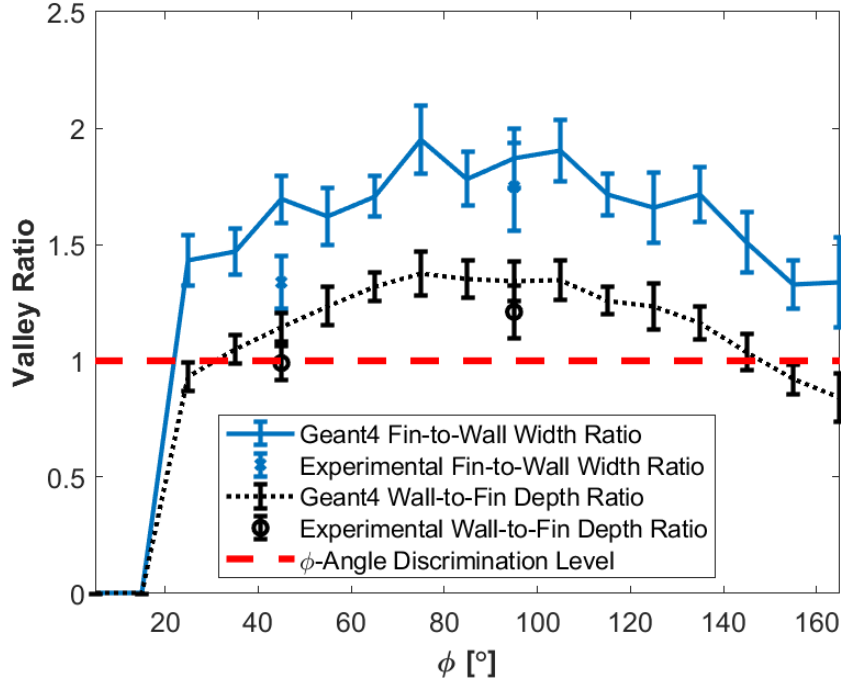


Figure 45. Comparison of the fin-to-wall width and wall-to-fin depth ratios as a function of  $\phi$  direction for both experimental and Geant4 neutron RSM simulations of an AmBe source. The dashed red line represents the discrimination threshold for being able to distinguish the wall from the fin valley of a DRC.

metric is qualitatively representative of the efficiency of the RSM system with respect to different source  $\phi$  directions, where an ideal mask should have a flat curve. For  $\phi$  directions between  $5^\circ$  and  $125^\circ$  the curve is relatively flat but drops off significantly at larger  $\phi$  angles. Although the mask material is equivalent for all polar angles, the detector is cylindrical, not spherical, meaning the active length and detector solid angle the particles traverse through is not constant for different  $\phi$  angles. Also, there are more components surrounding the detector acting as attenuation layers such as the aluminum tubes securing the mask, detector, and PMT at the larger  $\phi$  angles.

Experimentally, the relative percent efficiency loss,  $E_{Loss}$ , defined as the percent change in detected events, with and without the mask, is calculated for each set of directional measurements using Equation 25.  $N_0$  and  $N_1$  are the total number of detected events without the mask and with the mask, respectively.

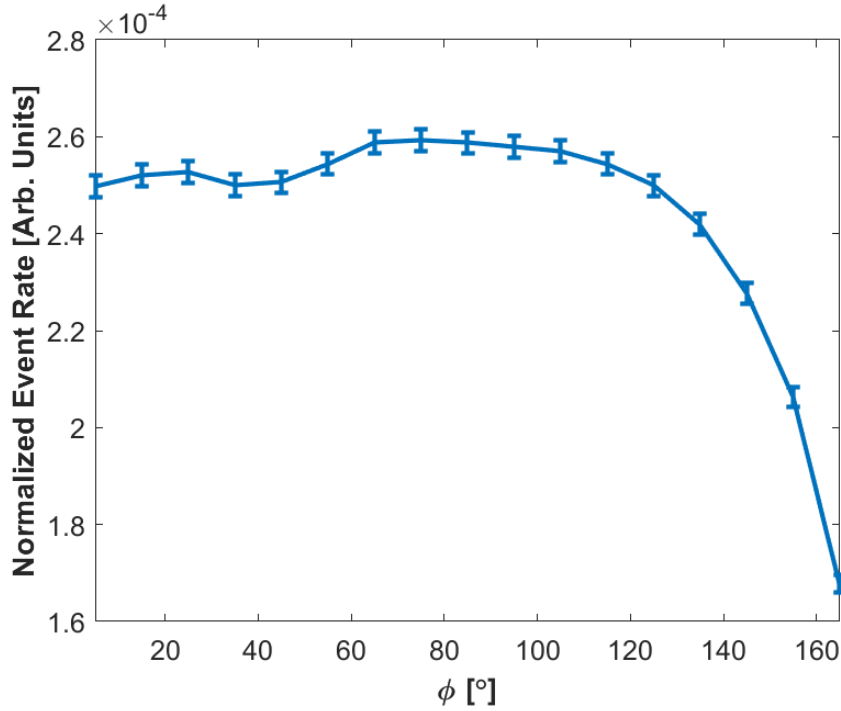


Figure 46. The Geant4 simulated normalized neutron event rate as a function of  $\phi$  direction for an AmBe source placed 86.36 cm away from the center of the detector.

$$E_{Loss} = \frac{|N_0 - N_1|}{N_0} * 100\% \quad (25)$$

The efficiency loss for each measurement separated by neutron and gamma-ray events is shown in Table 12. At most, the scatter mask caused a 10.4% loss in detected events; however the energy cut of 258 keVee excludes a lot of lower energy events in the relative efficiency loss calculation that would increase the loss of detected events.

Table 12. Summary of the relative efficiency loss caused by the scatter mask for each directional measurement performed with an AmBe source.

Source Position ( $r, \theta, \phi$ )	Particle	Relative Efficiency Loss [%]
86.36 cm, 85°, 45°	Neutrons	10.4±1.12
	Gamma Rays	4.02±1.47
106.46 cm, 35°, 95°	Neutrons	5.81±1.44
	Gamma Rays	2.29±1.86

## 5. Conclusion

This proof-of-concept study demonstrated both computationally and experimentally the ability to directionally detect neutrons and gamma rays through the integration of a portable detection system and additively manufactured Spartan I scatter mask. Previous efforts demonstrated this capability only for gamma rays using a NaI scintillator coupled with a PMMA scatter mask designed by FitzGerald and built by Charles [10–14]. The original RSM system lacks portability, is difficult to maintain, has directional degeneracies in the DRM, and suffers from mechanical instability because the mask alone weighs 28 pounds. In this research, the newly assembled RSM system coupled with the Spartan I scatter mask corrected most of the old RSM deficiencies, along with advancing the overall applicability, versatility, and modularity of the system. Additionally, enhancements made to the RSM Geant4 simulation package allow for simulating both neutron and gamma-ray detector responses.

To validate mixed-radiation directional detection, the PSD performance utilizing a 1" EJ-309 scintillator is quantified with FOM values ranging from 1.70 to 1.83, demonstrating the ability to discriminate between neutron and gamma-ray events. Next, comparisons between measured and Geant4 simulated pulse-height energy spectra for  $^{137}\text{Cs}$ ,  $^{60}\text{Co}$ ,  $^{22}\text{Na}$ , and AmBe radiation sources showed a high degree of similarity in the spectral shape based on calculated MAC values; where four out of five comparisons obtained values greater than 0.99. Experimentally, the RSM correctly predicted the AmBe source's direction within  $5^\circ$  in both  $\theta$  and  $\phi$  for neutron-induced events and within  $10^\circ$  for gamma-ray events for two measurement sets with varying distances and directions with a maximum uncertainty of  $4.63^\circ$ . The average percent difference between each rotational  $\theta$ -position for all experimental neutron and gamma-ray DRCs is only 1.88%. Additionally, the RSM system's directional detection FOV is computationally determined to cover  $360^\circ$  in  $\theta$  and  $25^\circ$  to  $165^\circ$  in  $\phi$ . Finally, the relative

efficiency loss caused by the scattering mask is no more than 10.4% for all neutrons and gamma rays depositing at least 258 keVee into the active detector volume. With these performance metrics, the RSM system demonstrates the novel ability to identify the direction of both neutrons and gamma-rays with a reasonable FOV and relatively low efficiency loss. These are appealing features for many nuclear safeguards and counterproliferation missions.

Directional detection systems have a plethora of applications important to nuclear safeguards and counterproliferation efforts including radiological surveying in shipping yards and reactor facilities, border crossing monitoring, public event security, and mobile vehicle or drone surveying. Both neutron and gamma-ray emitting materials pose a nuclear security threat if miss-handled or stolen, and with the developments made in this study, the RSM is able to locate both types of sources at a fraction of the cost compared to commercially available systems. Additionally, mixed-radiation detection allows for fusing the detected neutron and gamma-ray signatures to not only determine the direction of a source, but in future work will be used to characterize information such as the source type, point of origin, activity, isotopic composition, and shielding material.

## **5.1 Future Research**

This work provided an essential component for advancing the RSM directional detection system by validating the ability to identify the direction of both neutrons and gamma rays. However, further work is required to improve all aspects of this on-going project related to modeling, radiation detection, imaging, and engineering design to ultimately be able to assist in the nuclear security mission. Examples of future research tasks include:

- Improve the radiation transport model and reach a higher statistical agreement

between simulated and experimental measurements by obtaining. This involves testing different Geant4 physics packages, enhancing the fidelity in the modeled geometry, using a different recoil proton energy deposition conversion, and spectral convolution methods. This will then improve the ability to perform realistic parameter studies for various detector and mask materials and geometries, and other performance metrics such as the overall efficiency loss and neutron energy spectrum unfolding.

- Computationally and experimentally characterize the performance of various detectors. Then, determine the best detector for the RSM system to detect gamma rays and fast neutrons along with expanding the system capability to thermal neutrons as well. Current suggestions are an EJ-309B liquid scintillator,  $\text{Cs}_2\text{LiYCl}_6\text{:Ce}$  (CLYC) scintillator, or an organic glass scintillator.
- Determine the key performance parameters for a full scatter mask optimization. During the optimization process, explore other additive manufacturing materials such as polylactic acid (PLA), a cheaper alternative to PMMA, and INCONEL-718 printable metal.
- Program the RSM system to operate the DAQ and stepper motor using the RaspberryPi, which can then be controlled through a graphic user interface on a tablet, smartphone, or portable laptop.
- Compare the directional detection performance of the RSM system using a silicon photomultiplier (SiPM) to a regular PMT. Currently, the bulkiest and heaviest component of the system is the CAEN DAQ which is primarily being used because the module not only digitizes the detector output but also supplies the required PMT high voltage. SiPMs do not require as high of a supplied voltage, therefore a much smaller power supply and DAQ could be used to

reduce the overall weight, enhancing portability.

- Develop an imaging program that will be downloaded to the RaspberryPi to allow for real-time directional imaging.
- Manufacture and program an improved, deployable RSM prototype to demonstrate in the field.

## Appendix A. Equipment and Settings

A list of the primary components and the manufacturer of the RSM system are provided in Table 13. Figure 24 from Section 3.2.1 displays a labeled image of the components listed. A full list of radiation detection acquisition settings using the DPP-PSD software and specific for the CAEN DT5790 DAQ coupled with a 1" EJ-309 scintillator mounted to a Hamamatsu 1 1/8" R6094 PMT is also provided in Table 14. This table supplements the primary settings listed in Table 4 of Section 4.1.

**Table 13. A list of the primary components and the manufacturer for the RSM system.**

Component	Manufacturer
1" EJ-309 Liquid Scintillator	Eljen Technology
1 1/8" R6094 PMT	Hamamatsu
DT5790-DAQ	CAEN
VeroClear <sup>TM</sup> Scatter Mask	AFIT 3D Print Shop
HT24-100D-CAA Stepper Motor and Encoder Ring	Applied Motion
ST5-Plus Stepper Driver	Applied Motion
Polycase Box	Polycase
12V and 5V DC Portable DAQ Battery	Talentcell Technology
40V Motor Battery	Black and Decker
Raspberry Pi 3 Model B+	Raspberry Pi Foundation
Aluminum Tubes, Holders, and Detector Support	AFIT Model Shop

**Table 14.** A full list of the radiation detection data acquisition settings, supplementing Table 4, used throughout the experiment. These settings are directly inputted into the DPP-PSD software.

Settings	Input
High Voltage	-800 V
Current	310.15 $\mu$ A
Voltage Ramp Up	100 V/s
Voltage Ramp Down	150 V/s
Maximum Voltage for Safety	1500 V
Record Length	168 Samples or 672 ns
DC Offset	-30 Arb. Units
Threshold	250 LSB
Gate Offset	8 ns
Short Gate	60 ns
Long Gate	500 ns
Self-Trigger	Enabled
Trigger Hold Off	544 ns
Base Line Mean	32 Samples
Charge Sensitivity	40 fc/LSB

## Appendix B. Radiation Source Information

This research utilized the neutron and gamma-ray emissions of an AmBe source, as well as the gamma-rays emitted by  $^{137}\text{Cs}$ ,  $^{60}\text{Co}$ , and  $^{22}\text{Na}$ . Table 15 displays the source information which includes the name, identification (ID) number, half-life, production date, activity, and gamma-ray emission energy.

**Table 15.** A list of all of the sources used for this experiment, where the emission energy column represents the primary gamma-rays lines used in this research.

Nuclide	ID Number	Half Life [Years]	Production Date	Production Activity [ $\mu\text{Ci}$ ]	Emission Energy [keV]
$^{137}\text{Cs}$	644-69	30.17	01 Sep 00	10.00	661.66
$^{60}\text{Co}$	1263-32	5.272	15 Sep 07	10.30	1173.2 1332.5
$^{22}\text{Na}$	1287-63	2.605	15 Aug 09	106.5	511 1274.5
$^{241}\text{AmBe}$	T023	432.17	22 Nov 64	500000	4438

## Appendix C. Rotating Scatter Mask Research Repository

All of the work and analysis for this research is provided in a private online repository at [https://github.com/bve5056/Spartan1\\_Rotating\\_Scatter\\_Mask\\_Repository](https://github.com/bve5056/Spartan1_Rotating_Scatter_Mask_Repository). For access, please contact the author. The repository consists of two directories, **Experiment** and **Modeling**, where each directory contains various files, programs, and sub-directories along with **README** files to assist anyone who desires to reproduce or enhance this work.

The **Experiment** directory contains:

- A sub-directory, **Data**, with all of the raw and processed data obtained throughout the experiment.
- A sub-directory, **Data\_Processing\_Program**, with all of the MATLAB scripts and functions created to process the experimental data.
- A sub-directory, **Photos**, with various photographs of the equipment and experimental setup.
- A sub-directory, **RSM\_Instructions**, with instructions and settings for operating the RSM detection system.
- A sub-directory, **Miscellaneous**, with miscellaneous information and resources related to this research.

The **Modeling** directory contains:

- A sub-directory, **Spartan\_RSM**, with the RSM Geant4 simulation package.
- A sub-directory, **Geant4\_Data\_Processing\_Program**, with various MATLAB scripts and functions created to process the Geant4 simulated results along with comparing them to the processed experimental data.

- A sub-directory, **Geant4\_Results**, with all of the raw and processed Geant4 simulation data.
- A sub-directory, **SolidWorks\_Model**, with all of the SolidWorks files, developed by Martin and the AFIT model shop for designing and assembling the new RSM system [20].
- A sub-directory, **Miscellaneous**, with miscellaneous information and resources related to this research.

## Bibliography

1. Office of the Secretary of Defense, “2018 nuclear posture review,” 2018.
2. United States National Guard, “Civil Support Team,” <https://www.nationalguard.com/guard-experience/civil-support-team>, accessed: 2018-12-09.
3. R. Drumsta, “National guard team searches for radioactive material on lake champlain,” *United States Army Press Release*, accessed: 2018-12-09. [Online]. Available: [https://www.army.mil/article/172300/national\\_guard\\_team\\_searches\\_for\\_radioactive\\_material\\_on\\_lake\\_champlain](https://www.army.mil/article/172300/national_guard_team_searches_for_radioactive_material_on_lake_champlain)
4. United States Department of Energy: Office of Environment, Health, Safety and Security, “Nuclear Material Control and Accountability, DOE O 474.2,” 2016.
5. Nuclear Regulatory Commission, “Orphan Sources,” <https://www.nrc.gov/materials/miau/miau-reg-initiatives/orphan.html>, accessed: 2018-08-13.
6. A. L. Hutcheson, B. F. Philips, E. A. Wulf, L. J. Mitchell, W. N. Johnson, and B. E. Leas, “Maritime detection of radiological/nuclear threats with hybrid imaging system,” in *2013 IEEE International Conference on Technologies for Homeland Security (HST)*, Nov 2013, pp. 360–363.
7. PHDS Co, “GeGI Rad Nuc Standoff Detector White Paper,” <http://www.phdsco.com/products/gegi/gegi-info-sheet>, accessed: 2018-08-13.
8. G. F. Knoll, *Radiation Detection and Measurement, 4th Edition*. Hoboken, NJ: John Wiley & Sons, 2010.
9. H3D Inc., “Polaris-H<sup>TM</sup> Gamma-Ray Imaging Spectrometer,” <https://h3dgamma.com/home.php>, accessed: 2018-12-05.
10. J. G. FitzGerald, “A Rotating Scatter Mask for inexpensive gamma-ray imaging in orphan source search: Simulation results,” *IEEE Transactions on Nuclear Science*, vol. 62, no. 1, pp. 340–348, 2015.
11. J. V. Logan, “Rotating Scatter Mask for Gamma Source Imaging,” Master’s thesis, Air Force Institute of Technology, 2017.
12. R. J. Olesen, “Optimization and Parameter Characterization for Rotating Scatter Mask Designs,” Master’s thesis, Air Force Institute of Technology, 2018.
13. D. E. Holland, J. E. Bevins, L. W. Burggraf, and B. E. O’Day, “Rotating scatter mask optimization for gamma source direction identification,” *Nuclear Instruments and Methods in Physics Research Section A: Accelerators, Spectrometers, Detectors and Associated Equipment*, vol. 901, pp. 104 – 111, 2018. [Online]. Available: <http://www.sciencedirect.com/science/article/pii/S0168900218306429>

14. Z. T. Condon, "Multisource Direction Identification using a Rotating Scatter Mask," Master's thesis, Air Force Institute of Technology, 2018.
15. J. Braverman, J. Brennan, E. Brubaker, B. Cabrera-Palmer, S. Czyz, P. Marleau, J. Mattingly, A. Nowack, J. Steele, M. Sweany, K. Weinfurther, and E. Woods, "Single-Volume Neutron Scatter Camera for High-Efficiency Neutron Imaging and Spectroscopy," 2018.
16. K. Weinfurther, "Model-based Design Evaluation of a Compact , High-E ffi ciency Neutron Scatter Camera Preliminary PhD Report," vol. 2, no. 1, 2017.
17. CERN, "Geant4," [https://geant4.web.cern.ch/support/getting\\_started/about\\_geant4](https://geant4.web.cern.ch/support/getting_started/about_geant4), 1998.
18. J. B. Birks and F. W. K. Firk, "The Theory and Practice of Scintillation Counting," *Physics Today*, vol. 18, p. 60, 1965. [Online]. Available: <http://adsabs.harvard.edu/abs/1965PhT....18Q..60B>
19. J. Arthur, "A Double Time of Flight Method For Measuring Proton Light Yield," Ph.D. dissertation, University of California, Berkeley, 2017.
20. V. A. Martin, "SFFP Report: Optimization of the Rotating Scatter Mask System," 2018.
21. Saint-Gobain, "NaI(Tl) and Polyscin Sodium Iodide," <https://www.crystals.saint-gobain.com/products/nai-sodium-iodide>, accessed: 2018-08-13.
22. B. Kowash, "A Rotating Modulation Imager for the Orphan Source Search Problem," Ph.D. dissertation, The University of Michigan, 2008.
23. B. R. Kowash, D. K. Wehe, and J. A. Fessler, "A rotating modulation imager for locating mid-range point sources," *Nuclear Instruments and Methods in Physics Research, Section A: Accelerators, Spectrometers, Detectors and Associated Equipment*, vol. 602, no. 2, pp. 477–483, 2009.
24. B. R. Kowash and D. K. Wehe, "A unified near- and far-field imaging model for rotating modulation collimators," *Nuclear Instruments and Methods in Physics Research, Section A: Accelerators, Spectrometers, Detectors and Associated Equipment*, 2011.
25. N. O. Boyce, "Thermal Neutron Point Source Imaging Using a Rotating Modulation Collimator (RMC)," Master's thesis, Air Force Institute of Technology, 2010.
26. H. S. Kim, G. Lee, S. J. Ye, and G. Kim, "Design of a Rotational Modulation Collimator Utilizing Asymmetric Masks for the Gamma-Ray/Neutron Dual Imaging Technique," *2016 IEEE Nuclear Science Symposium, Medical Imaging Conference*

*and Room-Temperature Semiconductor Detector Workshop, NSS/MIC/RTSD 2016*, vol. 2017-January, pp. 4–5, 2017.

27. J. R. Lamarsh and A. J. Baratta, *Introduction to Nuclear Engineering*. Upper Saddle River, NJ: Prentice-Hall, Inc, 2001.
28. Los Alamos National Laboratory, “MCNP6.1.4,” <https://mcnp.lanl.gov/>, 2008.
29. K. S. Krane, *Introductory Nuclear Physics*. Hoboken, NJ: John Wiley & Sons, 1988.
30. J. Shipman and C. Barker, *Lab Manual for Shipman/Wilson/Todd’s an Introduction to Physical Science*. Brooks/Cole, 2007. [Online]. Available: <https://books.google.com/books?id=CwFiPwAACAAJ>
31. International Organization for Standardization, “Reference Neutron Radiations Part 1: Calibration fundamentals of radiation protection devices related to the basic quantities characterizing the radiation field, ISO 8529-1,” Tech. Rep.
32. International Atomic Energy Agency: Nuclear Data Services, “Evaluated Nuclear Data File (ENDF) ,” <https://www-nds.iaea.org/exfor/endl.htm>, 2018.
33. F. Pino, L. Stevanato, D. Cester, G. Nebbia, L. Sajo-Bohus, and G. Viesti, “The light output and the detection efficiency of the liquid scintillator EJ-309,” *Applied Radiation and Isotopes*, vol. 89, pp. 79–84, 2014. [Online]. Available: <http://dx.doi.org/10.1016/j.apradiso.2014.02.016>
34. Berger, M. J. and Hubbell, J. H. and Seltzer, S. M. and Chang, J. and Coursey, J. S. and Sukumar, R. and Zucker, D. S. and Olsen, *XCOM: Photon Cross Sections Database*, National Institute of Standards and Technology, Gaithersburg, MD, 2010. [Online]. Available: <http://physics.nist.gov/xcom>
35. Stratasys, “VeroClear™ Rigid Transparent Polyjet Material,” <https://store.stratasys.com/>, accessed: 2018-12-06.
36. M. A. Norsworthy, A. Poitrasson-Riviere, M. L. Ruch, S. D. Clarke, and S. A. Pozzi, “Evaluation of Neutron Light Output Response Functions in EJ-309 Organic Scintillators,” *Nuclear Instruments and Methods in Physics Research, Section A*, vol. 842, no. June 2016, pp. 20–27, 2017.
37. Berger, M. J. and Hubbell, J. H. and Seltzer, S. M. and Chang, J. and Coursey, J. S. and Sukumar, R. and Zucker, D. S. and Olsen, *ESTAR, PSTAR, and ASTAR: Computer Programs for Calculating Stopping-Power and Range Tables for Electrons, Protons, and Helium Ions (version 1.2.3)*, National Institute of Standards and Technology, Gaithersburg, MD, 2005. [Online]. Available: <http://physics.nist.gov/Star>
38. Ziegler, J. F., *SRIM-2013*, 2013. [Online]. Available: [www.srim.org](http://www.srim.org)

39. Ziegler, J. F., Biersack J.P., Zielger M.D., *SRIM: The Stopping and Range of Ions in Matter, 15th ed*, 2015.
40. M. Pastor, M. Binda, and T. Hararik, “Modal assurance criterion,” *Procedia Engineering*, vol. 48, pp. 543 – 548, 2012, modelling of Mechanical and Mechatronics Systems. [Online]. Available: <http://www.sciencedirect.com/science/article/pii/S1877705812046140>
41. P. Bevington and K. Robinson, *Data Reduction and Error Analysis for the Physical Sciences*. New York: McGraw-Hill, 2003.
42. P. Scott, “Chi-Square: Testing for Goodness of Fit,” <http://physics.ucsc.edu/~drip/133/ch4.pdf>, accessed: 2018-12-20.
43. The Raspberry Pi Foundation, “Raspberry Pi,” <https://www.raspberrypi.org/>, accessed: 2018-12-20.
44. CAEN, “User Manual UM2580 DPP-PSD Digital Pulse Processing for Pulse Shape Discrimination,” Tech. Rep., 2016.
45. D. Wright, “A Short Guide to Choosing a Physics List,” <http://geant4.slac.stanford.edu/MSFC2012/ChoosePhys.pdf>, accessed: 2018-12-09.
46. T. Koi, “HadronicPhysics II,” <https://www.nationalguard.com/guard-experience/civil-support-team>, accessed: 2018-12-20.
47. CAEN, “User Manual UM3188 DT5790 Digital Pulse Analyzer,” Tech. Rep., 2014.
48. ———, “User Manual UM5416 DT5790 DPP-PSD Registers Register Description for DT5790 DPP-PSD,” Tech. Rep., 2016.
49. Viareggio, “Application Note AN2506 Digital Gamma Neutron discrimination with Liquid Scintillators,” Tech. Rep., 2012.
50. ———, “Application Note AN3250 Pulse Shape Discrimination with different CAEN digitizers running DPP-PSD firmware,” Tech. Rep., 2014.
51. G. Chikkur and N. Umakantha, “A new method of determining the compton edge in liquid scintillators,” *Nuclear Instruments and Methods*, vol. 107, no. 1, pp. 201 – 202, 1973. [Online]. Available: <http://www.sciencedirect.com/science/article/pii/0029554X73900347>
52. MathWorks, “MATLAB Curve Fitting Toolbox,” <https://www.mathworks.com/products/curvefitting.html>, 2017, natick, MA, USA.
53. D. E. Holland, “SFFP Report: Computational Study of a Rotating Scatter Mask Using MCNP,” 2017.

54. Eljen Technology, "Response of EJ-301 Liquid Scintillator," [https://eljentechnology.com/images/technical\\_library/EJ301\\_Resp.pdf](https://eljentechnology.com/images/technical_library/EJ301_Resp.pdf), accessed: 2018-12-20.

# REPORT DOCUMENTATION PAGE

*Form Approved*  
*OMB No. 0704-0188*

The public reporting burden for this collection of information is estimated to average 1 hour per response, including the time for reviewing instructions, searching existing data sources, gathering and maintaining the data needed, and completing and reviewing the collection of information. Send comments regarding this burden estimate or any other aspect of this collection of information, including suggestions for reducing this burden to Department of Defense, Washington Headquarters Services, Directorate for Information Operations and Reports (0704-0188), 1215 Jefferson Davis Highway, Suite 1204, Arlington, VA 22202-4302. Respondents should be aware that notwithstanding any other provision of law, no person shall be subject to any penalty for failing to comply with a collection of information if it does not display a currently valid OMB control number. **PLEASE DO NOT RETURN YOUR FORM TO THE ABOVE ADDRESS.**

<b>1. REPORT DATE (DD-MM-YYYY)</b> 21-03-2019		<b>2. REPORT TYPE</b> Master's Thesis		<b>3. DATES COVERED (From — To)</b> Sept 2017 — Mar 2019	
<b>4. TITLE AND SUBTITLE</b>  DEVELOPMENT OF A MIXED-RADIATION DIRECTIONAL ROTATING SCATTER MASK DETECTION SYSTEM				<b>5a. CONTRACT NUMBER</b>	
				<b>5b. GRANT NUMBER</b>	
				<b>5c. PROGRAM ELEMENT NUMBER</b>	
<b>6. AUTHOR(S)</b>  Egner, Bryan V, 2d Lt, USAF				<b>5d. PROJECT NUMBER</b>	
				<b>5e. TASK NUMBER</b>	
				<b>5f. WORK UNIT NUMBER</b>	
<b>7. PERFORMING ORGANIZATION NAME(S) AND ADDRESS(ES)</b> Air Force Institute of Technology Graduate School of Engineering and Management (AFIT/EN) 2950 Hobson Way WPAFB OH 45433-7765				<b>8. PERFORMING ORGANIZATION REPORT NUMBER</b>  AFIT-ENP-MS-19-M-075	
<b>9. SPONSORING / MONITORING AGENCY NAME(S) AND ADDRESS(ES)</b> Defense Threat Reduction Agency 8725 John J Kingman Rd #6201, Fort Belvoir, VA 22060				<b>10. SPONSOR/MONITOR'S ACRONYM(S)</b>	
				<b>11. SPONSOR/MONITOR'S REPORT NUMBER(S)</b>	
<b>12. DISTRIBUTION / AVAILABILITY STATEMENT</b>  APPROVED FOR PUBLIC RELEASE; DISTRIBUTION A: UNLIMITED.					
<b>13. SUPPLEMENTARY NOTES</b>					
<b>14. ABSTRACT</b> Previous work demonstrated gamma-ray directional detection through the integration of a radiation detection system and an additively manufactured rotating scatter mask (RSM). This work advances the RSM directional detection system through improvements in the system's design, validation of a new scatter mask, and the novel ability to directionally detect both neutrons and gamma rays. The mixed-radiation RSM system developed for this research utilized the Spartan I mask design coupled with a 1" EJ-309 liquid scintillator. A GEometry ANd Tracking (Geant4) model is developed and quantitatively compared to experimental measurements for both pulse-height energy spectra and detector response curves, validating the system's directional detection capabilities. Two sets of directional measurements are performed with an americium-beryllium source, varying the source's distance and direction for each set. The RSM correctly identified the direction of the source within 5° in both the azimuthal and polar directions for neutron induced events and within 10° for gamma rays. The results demonstrated the RSM is a compact, lightweight, and modular directional detection system useful for safeguard and counterproliferation missions.					
<b>15. SUBJECT TERMS</b>  Rotating Scatter Mask, Directional Detection, Neutron Detection, Gamma-Ray Detection, Monte Carlo Simulation					
<b>16. SECURITY CLASSIFICATION OF:</b>			<b>17. LIMITATION OF ABSTRACT</b>	<b>18. NUMBER OF PAGES</b>	<b>19a. NAME OF RESPONSIBLE PERSON</b>
<b>a. REPORT</b>	<b>b. ABSTRACT</b>	<b>c. THIS PAGE</b>			Dr. Larry W. Burggraf, AFIT/ENP
U	U	U	U	114	<b>19b. TELEPHONE NUMBER (include area code)</b> (937) 255-3636, x4507